Material properties and microwave loss in tantalum superconducting resonators

Zur Erlangung des akademischen Grades eines

Doktors der Naturwissenschaften
(Dr. rer. nat.)

von der KIT-Fakultät für Physik des
Karlsruher Instituts für Technologie (KIT)

angenommene
Dissertation

von

M. Sc. Ritika Dhundhwal

Tag der mündlichen Prüfung: 01 August 2025

Referent: Prof. Dr. Ioan Mihai Pop
Korreferent: TT.-Prof. Dr. Philip Willke

This document is licensed under a Creative Commons Attribution 4.0 International License (CC BY 4.0): https://creativecommons.org/licenses/by/4.0/deed.en

Abstract

For practical superconducting quantum processors, orders of magnitude improvement in coherence is required, motivating efforts to optimize hardware design and explore new materials. Among the latter, tantalum is a promising material, as it has been suggested in recent literature, that using it to fabricate the shunting capacitor of superconducting transmon qubits [1, 2] improves their coherence. In general, the meta-stable β-phase that forms when depositing tantalum on room-temperature substrates was avoided suggesting that it adds loss to superconducting circuits made from them. The aim of this thesis was to investigate the correlations between tantalum thin film properties in general, such as a possible β-phase component, with dissipation in superconducting resonators. The focus was on the single photon regime most relevant in quantum circuits.

We use tantalum films deposited under different growth conditions to achieve varied film properties. To be able to correlate microwave loss to material properties of the films, we characterize them using various material characterization tools such as X-ray diffraction (XRD), DC transport measurements, SQUID magnetometry, scanning tunneling microscopy (STM), scanning transmission electron microscopy (STEM) and scanning precession electron diffraction based automated crystal orientation mapping (ACOM) [3].

In particular, we demonstrate that lumped element microwave resonators fabricated from β-phase-containing tantalum films achieve single photon quality-factors Q_i up to $(5.0 \pm 2.5) \times 10^6$ [4]. XRD measurements suggest that the volume fraction of the β-phase in the film is approximately 8.5%. Surprisingly, we show that the low power internal quality-factor of these resonators is as high as for ones composed of pure α-phase tantalum, fabricated with the same recipe, and comparable to state of the art.

For all the tantalum resonators post-processed with aggressive cleaning in buffered-oxide etchant (BOE), we find that Q_i improved by a factor three to six, irrespective of the film properties [4]. A similar observation was made for example by Crowley *et al.* [5]. Furthermore, we investigated the durability of the reduction in temperature dependent loss under different storage conditions as well as its reproducibility. We found that storing the resonators in vacuum for weeks preserves the coherence, while storage in air for a similar period leads to a degradation comparable to before the cleaning step.

Temperature dependent measurements of the tantalum resonator Q_i and frequency shift reveal minor concentrations of regions with low superconducting transition temperature T_c in the some of the films, which remain undetected in various characterization methods such as XRD, STEM or DC transport. Modeling the temperature sweeps with the Mattis-Bardeen (MB) formalism, allows us to conclude that some of the resonators suffer from excess thermal quasiparticle loss at intermediate temperature, possibly associated with the tantalum β-phase which has a lower T_c than the α-phase [6].

We identified the temperature sweep measurements to be a particularly sensitive method for detecting the presence of minor concentrations of low T_c regions in the films not easily detectable by other means. Finally, we found that the low T_c regions only make up a small volume fraction ($1-10\%$) of the resonator, by comparing the kinetic inductance fraction α_k obtained from two different methods: In the resonators exhibiting excess thermal quasiparticle loss, the MB fit of the temperature dependent frequency shift results in α_k one to two orders of magnitude lower than the value deduced from carefully comparing measured and simulated resonator frequency at base temperature.

Our findings indicate that the relationship between the concentration of the β-phase and Q_i is not trivial. We propose that the presence of a small amount β-phase can be advantageous rather than harmful, potentially enhancing coherence in tantalum-based superconducting circuits. We suggest that regulating the concentration of the β-phase, while not necessarily aiming to eliminate it, offers a promising strategy for further decreasing loss in Ta-based quantum circuits and in addition, also enhancing their critical magnetic fields.

Contents

Acknowledgments

This Ph.D. would not have been possible without the guidance and support of many remarkable individuals. I am deeply grateful to all the kind souls who have contributed to this journey.

First and foremost, I would like to thank my supervisor, Ioan M. Pop, for providing me with the opportunity to work on this fascinating project involving tantalum. This has been a great learning experience.

I owe special thanks to my co-supervisor, Thomas Reisinger, whose day-to-day mentorship has been invaluable. From cleanroom fabrication and film deposition to the intricacies of scientific writing, he has guided me through every aspect of this research. I am particularly grateful for his abundant patience and unwavering support throughout this process.

I acknowledge the European Union's Horizon 2020 research and innovation programme QUSTEC under the Marie Sklodowska-Curie grant agreement No 847471, for providing my PhD grant. I thank whole QUSTEC team and other fellow members for all the nice interactions.

My sincere thanks to Philip Willke for agreeing to be my external reviewer.

I thank Hahn Horst for allowing me to use their impressive film deposition facilities at INT. Thanks to Gleb Iankevich and Robert Kruk at INT for their friendly help with technical support for sputtering chamber whenever Thomas was not around.

I want to thank all my colleagues from the BFQ group for their help and interesting scientific discussions: Dennis Rieger, Nicolas Zapata, Philipp Lenhard, Simon Geisert, Mathieu Féchant, Martin Spiecker, Ameya Nambisan, Nicolas Gosling, Denis Bénâtre, Patrick Paluch, Simon Günzler, Mitchell Field and Sören Ihssen. Thank you Mahya Khorramshahi for all the nice conversations. Thanks to Francesco Valenti for organizing the amazing HIQCuing seminar at Villa Nante in the summer of 2021. I would also like to thank the former group members of BFQ: Daria Gusenkova, Patrick Winkel, Ivan Takmakov and Lukas Grünhaupt.

I am grateful to Haoran Duan, Lukas M. Brauch, Soroush Arabi, at KIT; to Sudip Pal and Florentine Scharwaechter at University of Stuttgart for their expertise and efforts. To

Dirk Fuchs at IQMT, Alexander Welle at IFG. Your work has brought a lot of value to this project. Without your efforts, this thesis would be incomplete.

I want to acknowledge the technical and organizational help of Lukas Radtke and Aina Qunitilla at the CFN cleanroom. The INT people particularly Simone Dehm for her help on the e-beam machine, Martin Limbach for his help with deposition system and the mechanical workshop of Michael Meyer. Also thanks to IQMT administrative staff: Dorothea Trautmann for her friendly support.

I want to thank the collaborators from ENS, Paris: Zaki Leghtas and José Palomo, Marc Scheffler from University of Stuttgart and Gerhard Kirchmair from University of Innsbruck.

Thanks to Alice & Bob for giving me the opportunity to work at their place. Particularly to Jeanne Solard for her friendly guidance through out the collaboration. Thanks to Yuki Nojiri, Jeremy Stevens, and Anil Murani for all the fruitful discussions.

At the end, I would like to thank my friends and family. First, to my parents for their love and support, to my two amazing sisters who bring so much joy to my life and to my little nephew for being the sweetest sunshine. I am grateful to have you all by my side. Thanks to Malati and Rashmi for their beautiful friendship through all these years. My heartfelt gratitude goes to Brigitte and Rudolf Poßlovski for their unconditional support and kindness in all aspects of my journey, and for exemplifying what it means to be a truly good human being. Finally, to Benjamin, for supporting me through everything, especially during writing this thesis. From cooking incredible meals during my busy writing days to carefully proofreading every page, you've been there for me in ways that matter most.

List of Publications

[1] **R. Dhundhwal**, H. Duan, L. Brauch, S. Arabi, D. Fuchs, A. A. Haghighirad, A. Welle, F. Scharwaechter, S. Pal, M. Scheffler, J. Palomo, Z. Leghtas, A. Murani, H. Hahn, J. Aghassi-Hagmann, C. Kübel, W. Wulfhekel, I. M. Pop, and T. Reisinger, *High quality superconducting tantalum resonators with beta phase defects*, arXiv:2502.17247, 2025.

Submitted to APL, 1^{st} revision

[2] S. Arabi, Q. Li, **R. Dhundhwal**, D. Fuchs, T. Reisinger, I. M. Pop, and W. Wulfhekel, *Magnetic bound states embedded in tantalum superconducting thin films*, Applied Physics Letters **126**(11), 2025.

[3] H. Duan, **R. Dhundhwal**, G. C. Marques, D. Fuchs, I. M. Pop, T. Reisinger, and J. Aghassi-Hagmann, *Simulation framework for thermal quasi-particle microwave loss in multi-material superconducting quantum circuit elements*,

IEEE Transactions on Applied Superconductivity, 2025

[4] Y. V. Krasnikova, A. A. Murthy, D. Bafia, F. Crisa, A. Clairmont, Z. Sung, J. Lee, A. Cano, M. Shinde, D. M. T. van Zanten, M. Bal, A. Romanenko, A. Grassellino, **R. Dhundhwal**, D. Fuchs, T. Reisinger, I. M. Pop, A. Suter, T. Prokscha, and Z. Salman, *Experimental Observation of Short-Range Magnetic Correlations in Amorphous Nb_2O_5 and Ta_2O_5 Thin Films*, arXiv:2505.07957, 2025.

Submitted to PRB

List of Figures

List of Tables

1 Introduction

Quantum computing holds potential to solve problems that conventional classical computers cannot handle. In 1982, Richard Feynman popularized the revolutionary idea of constructing a computer that could simulate physical systems that are governed by the laws of quantum mechanics [7]. Such a computer could tackle complex technological challenges in fields like chemistry, biology, materials science, finance, and cryptography, which are deemed nearly unsolvable by standard classical computers.

Developing a practical quantum computer is an immensely intricate challenge. Nonetheless, the quantum computing field has achieved significant strides over the past two to three decades, and efforts are still actively progressing. Today, multiple companies, including IBM, D-Wave, Google, and Microsoft, have developed functional quantum computers. However, these devices are not yet suitable for widespread practical application. A notable milestone in this direction was achieved in 2019 by Google with their first demonstration of quantum advantage [8]. The concept of "quantum advantage" refers to the ability of a quantum processor to successfully solve a problem that is practically insurmountable for a classical computer to simulate. More recently, D-wave has also demonstrated quantum advantage by simulating the continuous-time quantum dynamics of the transverse-field Ising model [9].

Several platforms are available to realize a quantum computer such as superconducting circuits [10], trapped ions [11], photons [12], and semiconductor spin systems [13]. Out of these, superconducting circuits have emerged as a leading platform for quantum information processing [14], and the past two decades have seen remarkable progress in their performance [10, 15]. This platform is also the most relevant for this thesis. Scaled-up circuits, consisting of tens of qubits, have been employed to successfully demonstrate the key milestones such as quantum advantage [8] and error correction [16]. As a further example for the utility of superconducting circuits, quantum-limited Josephson parametric amplifiers form key ingredients for high fidelity qubit read out and state preparation [17].

A qubit is a quantum analogue of a classical bit and serves as the fundamental unit of information in a quantum computer. It operates using two computational states- the ground state and the excited state. What sets it apart from the classical bit are the quantum mechanical phenomenon like superpositions i.e. the ability to be in the ground and the excited states at the same time, coherence, and entanglement [18]. Most

quantum computing platforms mentioned earlier, with the exception of superconducting circuits, use naturally occurring microscopic degrees of freedom to realize a qubit [19]. For example, systems such as the spin of an electron, which can be either spin up or spin down, or the polarization states of a photon, naturally provide the necessary two computational states for a qubit. Similarly, atoms can be used by isolating their two lowest energy levels i.e. the ground and first excited state. While quantum behavior is often associated with particles at atomic or subatomic scales, this assumption does not hold for qubits based on superconducting circuits, which are macroscopic in nature yet exhibit quantum coherence.

1.1 Superconducting quantum circuits

Superconducting circuits, as the name suggests, are quantum integrated circuits constructed from commonly known electrical elements made from superconducting materials [20]. In these circuits, the qubit is made from collective electrodynamic modes of macroscopic electrical elements like capacitors, inductors, and tunnel junctions and exhibits energy spectra similar to that of atoms. This offers certain advantages: it enables strong coupling or interaction with other qubits, their high scalability, and allows for the tuning and control of properties of these engineered atoms by carefully choosing circuit element parameters. Moreover, the fabrication of these circuits benefits greatly from well established lithography technologies prevalent in the semiconductor industry.

Superconducting qubits are constructed from Josephson tunnel junctions, capacitors, inductors, and transmission lines. The Josephson tunnel junction forms the heart of the qubit and it consists of two superconducting electrodes separated by a thin dielectric or insulating barrier [20]. This junction introduces crucial nonlinearity into the circuit, enabling isolation and manipulation of the two lowest energy levels that serve as the qubit basis states. Capacitors and inductors, on the other hand function as linear circuit elements. These components typically employ planar geometries where the only dielectric is the substrate on which they are patterned. Superconducting inductors, in particular, can also be made from either junction arrays or disordered superconducting materials [21]. The dissipation in transmon qubits is predominantly limited by the capacitive component. Since, these losses can be quantified through analysis of a simple linear harmonic oscillator. This thesis concentrates on understanding loss mechanisms in harmonic oscillator as a pathway to improving qubit performance.

As solid-state macroscopic circuits, a major challenge faced by superconducting circuits is decoherence [22] which limits their performance. Decoherence happens when a qubit interacts with the environment's uncontrolled degrees of freedom leading to energy dissipation or dephasing. The performance of qubits is quantified by two figures of merit: lifetime and dephasing time. Lifetime describes how long the qubit can maintain

its quantum state before it interacts with the environment's uncontrolled degrees of freedom leading to energy dissipation. It involves two decay constants, the energy relaxation time T_1 and the transverse relaxation time T_2. T_1 indicates the time required for the excited state population to decay to $1/e$ of its initial value. T_2 describes the time span over which the qubit losses its phase information and is related to the energy relaxation time as well as pure dephasing time T_ϕ. Collectively, they are also referred to as coherence times. These time scales are related in the following way:

$$\frac{1}{T_2} = \frac{1}{2T_1} + \frac{1}{T_\phi} \tag{1.1}$$

The performance of resonator is quantified by the quality-factor Q which is a dimensionless quantity and is a measure of the energy lost in the circuitry. Its value relates inversely with energy lost. The parameter Q will be a primary focus in the later chapters of this thesis to quantify the losses observed in resonator measurements. A detailed presentation of quality factors is given in Chapter 4. The intrinsic quality-factor Q_i and the lifetime are related by [23, 24]

$$Q_\mathrm{i} = T_1(2\pi f) \tag{1.2}$$

where f is the transition frequency between the ground and the excited state. Our primary focus in this thesis will be the examination of the harmonic oscillator.

Unlike other platforms like trapped ions which can achieve qubit lifetimes of several seconds or even minutes [11], the lifetime of superconducting qubits extends at best up to about 1 ms. Among the recognized mechanisms of loss in state-of-the-art hardware, dielectric loss, found in bulk and interfaces of constituent materials, is a notable culprit [23]. Figure 1.1, adapted from [25], shows the evolution of T_1 and T_2 over decades, since the first demonstration of the superconducting qubit in 1999 [26], with a coherence time nearing 1 ns. Almost two decades later, the record lifetime for a transmon qubit reached $(114 \pm 19)\,\mu\mathrm{s}$ [27], which is a five-order-of-magnitude improvement. To mitigate the dielectric losses, so far, efforts have largely centered on understanding the microscopic origins of losses within well-established material platforms such as aluminum and niobium. Additional routes include improvement in fabrication techniques, reducing the various loss channels and the sensitivity to loss channels by improving circuit design.

However, the recent advancements to improve qubit lifetimes have focused on using new constituent materials for making qubits [28–30]. More recently, tantalum (Ta) [1, 2] has joined the select club of materials with low dielectric loss tangent for quantum devices, challenging the performance of established platforms based on aluminum, niobium [30, 31] or titanium nitride [32, 33]. The central material in this thesis is this newly emerging material tantalum.

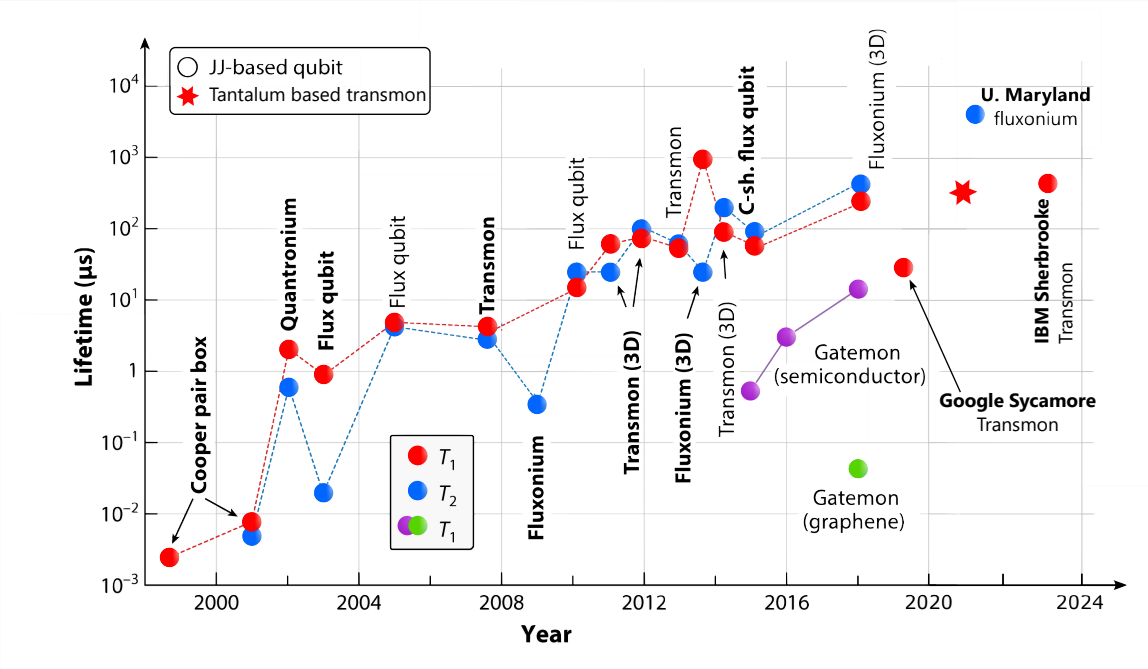

Figure 1.1: Trends in lifetimes and coherence times in superconducting qubits based on Josephson junction (JJ) in the last two decades, highlighting key milestones in bold font. The figure is adapted from [25] with added points from [40].

Record qubit lifetimes on the order of hundreds of microseconds have been demonstrated in transmon qubits composed of Ta capacitors shunting a standard $Al/AlO_x/Al$ junction [1, 2]. However, the coherence in Ta-based circuits is highly dependent on deposition and fabrication process parameters. In particular, a peculiarity of Ta thin films is the possible formation of a tetragonal β-phase [34], competing with the body centered cubic (BCC) bulk α-phase. The latter has a superconducting transition temperature (T_c) of 4.4 K, while the meta-stable β-phase has a significantly lower T_c of 0.5 K [35]. It can form when depositing Ta on near room-temperature substrates [36]. The underlying cause for the coherence improvement in Ta devices remains a matter of intensive research and is most likely multi-faceted [37]. The improvement is often linked to the use of pure α-phase Ta and then accredited to the stable, self-limiting surface oxide [38, 39]. However, there is a large spread in the reported loss for Ta-based devices in the literature, possibly caused by variations in film microstructure.

1.2 Superconductivity

To gain a comprehensive understanding of how superconducting qubits function, one must first grasp the fundamental concepts of superconductivity. This section aims to present the essential concepts of superconductivity relevant for this thesis. Supercon-

ductivity is characterized by two unique electrodynamic properties that emerge when certain materials are cooled to sufficiently low temperatures. The first is the complete vanishing of DC electrical resistance, below a threshold temperature known as the critical temperature, T_c. This remarkable phenomenon was first observed by H. Kamerlingh Onnes in 1911, when he observed that mercury's electrical resistance dropped to zero at temperatures below 4.2 K [41, 42]. The second hallmark of superconductivity is the expulsion of the applied magnetic field, a phenomenon also known as Meissner effect [43]. In this state, the material exhibits perfect diamagnetism, provided the magnetic field strength remains below a material specific value, known as the critical field, H_c.

The phenomenological theory by London offers an explanation for this concept. The density of the super-current, which does not encounter scattering or friction, can be expressed as $\mathbf{J_s} = -en_s\mathbf{v_s}$, where n_s is the density and $\mathbf{v_s}$ is the velocity of the superconducting charge carriers. By applying the equation of motion in the presence of an electric field $\mathbf{E}$, we obtain the *first London equation*

$$\frac{\partial \mathbf{J_s}}{\partial t} = \frac{n_s e^2}{m_e}\mathbf{E} \tag{1.3}$$

where m_e is electron mass. Utilizing the third Maxwell's equation, $\nabla \times \mathbf{E} = -\partial \mathbf{B}/\partial t$, and applying the curl operator to Eq. (1.3), we arrive at the following relationship between $\mathbf{J_s}$ and the magnetic field $\mathbf{B}$

$$\frac{\partial}{\partial t}\left(\frac{m_e}{n_s e^2}\nabla \times \mathbf{J_s} + \mathbf{B}\right) = 0 \tag{1.4}$$

This indicates that the expression inside the brackets of Eq. (1.4) must be constant. London hypothesized that this constant is, in fact, zero, which leads to the formulation of the *second London equation* describing the Meissner effect

$$\nabla \times \mathbf{J_s} = -\frac{n_s e^2}{m_e}\mathbf{B} \tag{1.5}$$

Taking the fourth Maxwells' equation, applying curl to it and using Eq. (1.5), we deduce that the resulting magnetic field has the form $\mathbf{B}(x) = B_0 \mathrm{e}^{-x/\lambda_\mathrm{L}}$ where we introduce a key parameter for the superconductor, London penetration depth λ_L

$$\lambda_\mathrm{L} = \sqrt{\frac{m_e}{\mu_0 n_s e^2}} \tag{1.6}$$

The magnetic field inside a superconductor does not abruptly go to zero but it decays over a length scale of λ_L from the surface. It is a material property and since n_s depends on temperature, λ_L also depends on temperature.

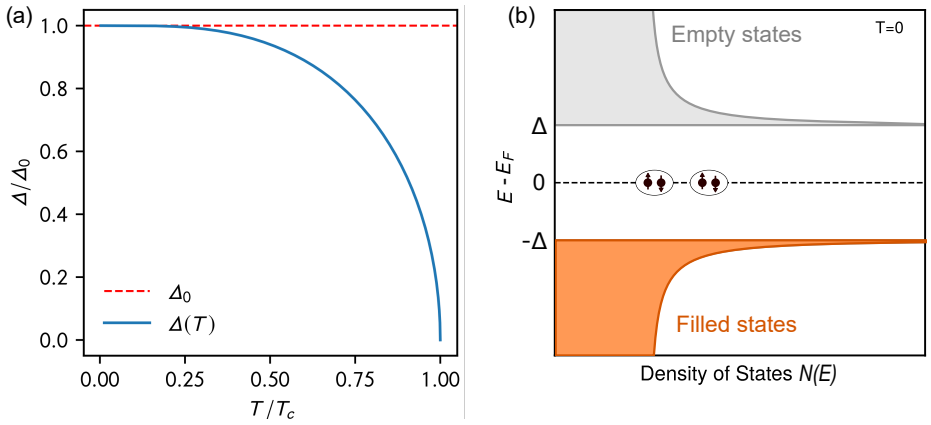

Figure 1.2: (a) The superconducting gap Δ as a function of temperature. Both the gap energy and the temperature are normalized to their values at $T = 0$. (b) Energy vs density of states of quasiparticles at $T = 0$. The ground state of Cooper pairs is shown by dashed line at $E = E_F$.

In 1957, Bardeen, Cooper, and Schrieffer introduced the first microscopic explanation of superconductivity, also known as BCS theory [44]. They proposed that an attractive interaction can arise between two conduction electrons with opposite spin and momentum, and energy near the Fermi energy, which is mediated by the lattice vibrations, called phonons. This leads to the formation of bound electrons, known as Cooper pairs responsible for lossless current. The electrons in the Cooper pair have zero net spin and momentum which makes them bosons and they obey Bose-Einstein statistics. Therefore, Cooper pairs in a condensate occupy the same quantum state, known as BCS ground state and can be described by a macroscopic wave function Ψ with a macroscopic phase ϕ

$$\Psi = \Psi_0 e^{i\phi} \tag{1.7}$$

The wave function is related to the density of cooper pairs $n_s = |\Psi_0|^2$.

The Cooper pairs have lower energy than the single electrons and their formation creates a gap, Δ around the Fermi energy in the density of states as shown in Fig. 1.2(b). The BCS theory predicts the form of Δ as a function of temperature by the following equation [44]

$$\frac{1}{N_0 V} = \int_0^{\hbar\omega} \frac{dE}{\sqrt{E^2 + \Delta^2(T)}} \tanh\left(\frac{\sqrt{E^2 + \Delta^2(T)}}{2k_B T}\right) \tag{1.8}$$

where N_0 is the density of single spin states per unit energy at the Fermi surface, V is the attractive potential between electron and phonon, k_B is the Boltzman constant and E is the energy. Solving Eq. (1.8) for two conditions: $T = 0$ where $\Delta = \Delta_0$ and for $T = T_c$ above which the superconducting gap vanishes $\Delta = 0$, we arrive at the following relation between Δ_0 and T_c

$$2\Delta_0 = 3.5 k_B T_c \tag{1.9}$$

The temperature dependence of Δ is shown in Fig. 1.2(a).

Another characteristic length for superconductors is the coherence length ξ which is a measure of the spatial extent of the Cooper pairs. It can be understood as the length over which the superconducting state decays from the boundary of a material. Its value is maximum at $T_c = 0$ and is given by

$$\xi_0 = \frac{\hbar v_F}{\pi \Delta_0} \tag{1.10}$$

Superconducting materials fall into two categories: type-I and type-II, distinguished by their electrodynamic behavior, which depends on two fundamental length scales: the magnetic penetration depth λ and the coherence length ξ.

Type-I superconductors exhibit a straightforward two-state behavior: they remain in the Meissner state until the applied magnetic field exceeds the critical value H_c, above which they transition directly to the normal conducting state. In contrast, type-II superconductors exhibit three-state behavior governed by two critical magnetic field. Below the lower critical field H_{c1}, these materials operate in the Meissner state, completely expelling magnetic flux. As the field increases beyond H_{c1}, the system enters an intermediate regime called the mixed state. Here, it becomes energetically favorable for magnetic vortices to form within the superconductor, allowing some of the applied field to penetrate the material through vortex nucleation. Finally, when the field reaches the upper critical value H_{c2}, the superconductor loses its superconducting properties entirely and transitions to the normal conducting state.

1.3 Quantum LC resonator

In this section, I present the quantum mechanical description of the LC harmonic oscillator as shown in Fig. 1.3(a), which results in a quantization of its energy levels. The classical dynamics of the harmonic oscillator can be understood by obtaining a Hamiltonian which describes the total energy of the system. The energy in this system oscillates between the capacitor C in form of electrical energy and the inductor L as magnetic energy and they are given by

$$\text{charging energy } E_C = \frac{q^2}{2C}, \quad \text{inductive energy } E_L = \frac{\Phi^2}{2L} \tag{1.11}$$

In analogy with a classical mechanical harmonic oscillator, the electrical and the magnetic energies are equivalent to the kinetic and potential energies, respectively [19]. Following the framework of the Lagrange-Hamilton formulation, one can represent the circuit elements, L and C, in terms of one of its generalized circuit coordinates, charge on the

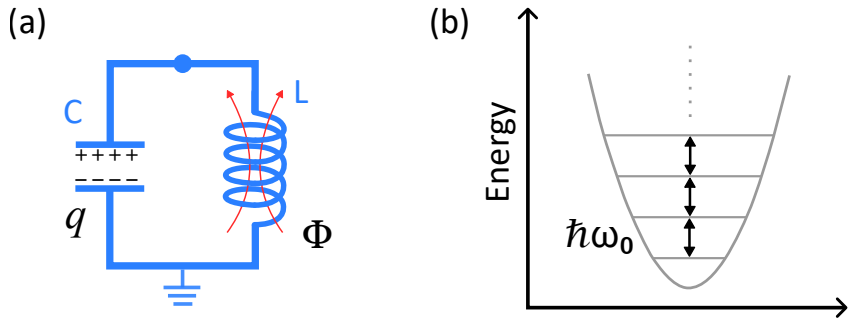

Figure 1.3: (a) Circuit representation of a LC harmonic oscillator in parallel configuration. (b) Energy spectrum of the oscillator showing discrete energy levels.

capacitor $q = CV$ or flux in the inductor $\Phi = Ldq/dt$. We can write the Lagrangian of the circuit in terms of charge

$$\mathscr{L} = E_{\text{kin}} - E_{\text{pot}}, \qquad \mathscr{L}(q, \dot{q}) = \frac{q^2}{2C} - \frac{L\dot{q}^2}{2} \tag{1.12}$$

Charge and flux are conjugate variables. So we can write

$$\frac{\partial \mathscr{L}}{\partial \dot{q}} = L\dot{q} = \Phi \tag{1.13}$$

By definition, the Hamiltonian is related to the Lagrangian by

$$\mathscr{H}(\Phi, q) = \mathscr{L}(\dot{q}, q) + \Phi\dot{q} \tag{1.14}$$

Therefore, we can write the classical Hamiltonian for the harmonic oscillator as

$$\mathscr{H} = \frac{q^2}{2C} + \frac{\Phi^2}{2L} \tag{1.15}$$

The quantum Hamiltonian can be written by converting the flux and charge variables into operators in Eq. (1.15) such that they follow the commutation relation $[\hat{\Phi}, \hat{q}] = i\hbar$

$$\hat{\mathscr{H}} = \frac{\hat{q}^2}{2C} + \frac{\hat{\Phi}^2}{2L} \tag{1.16}$$

Following the mechanical oscillator analogy, where momentum and position are canonical conjugate variables, the Hamiltonian is given by

$$\mathscr{H} = \frac{\hat{p}^2}{2m} + \frac{1}{2}m\omega^2\hat{x}^2 \tag{1.17}$$

where the mass m is equivalent to C, the momentum $\hat{p}$ is equivalent to the charge, the position $\hat{x}$ to flux and frequency ω to $1/\sqrt{LC}$. Another way to express the above

Hamiltonian is [45]

$$\hat{\mathscr{H}} = \hbar\omega_0\left(\hat{a}^\dagger\hat{a} + \frac{1}{2}\right) \qquad \text{where} \quad \omega_0 = \frac{1}{\sqrt{LC}} \tag{1.18}$$

where, $\hat{a}$ and $\hat{a}^\dagger$ are the creation and annihilation operators and ω_0 is the resonant frequency of the LC oscillator. Using the definition of characteristic impedance $Z_0 = \sqrt{L/C}$, the creation and annihilation operators can be written as:

$$\hat{a} = \sqrt{\frac{C\omega}{2\hbar}}\left(\hat{\Phi} + i\frac{\hat{q}}{C\omega}\right) \qquad \text{and} \qquad \hat{a}^\dagger = \sqrt{\frac{C\omega}{2\hbar}}\left(\hat{\Phi} - i\frac{\hat{q}}{C\omega}\right) \tag{1.19a}$$

$$\hat{a} = \frac{1}{\sqrt{2\hbar Z_0}}\left(\hat{\Phi} + iZ_0\hat{q}\right) \qquad \text{and} \qquad \hat{a}^\dagger = \frac{1}{\sqrt{2\hbar Z_0}}\left(\hat{\Phi} - iZ_0\hat{q}\right) \tag{1.19b}$$

The energy spectra of a quantum LC oscillator is shown in Fig. 1.3(b) with discrete, equally spaced energy levels separated by $\hbar\omega_0$. Describing a typical LC oscillator with quantum operators does not inherently make it quantum in nature. This is due to the fact that when the oscillator is strongly coupled to a lossy environment, energy dissipation occurs, which suppresses quantum effects. Consequently, the quantum states of the oscillator transition into coherent states, which are combinations of Fock (energy eigen) states. To observe quantum behavior such as quantum tunneling or superpositions of states, the oscillator must operate at very low energy; specifically, close to a single quantum of energy $\hbar\omega_0$. This requires cooling the system to temperatures where the thermal energy $k_B T \ll \hbar\omega_0$. Therefore, to properly understand dissipation mechanisms relevant to quantum devices, it is important to study microwave resonators in this single-photon regime, as we will explore in Chapter 4. As an example, for a resonator at 5 GHz, this implies a temperature below approximately 240 mK. However, even at such low temperatures, normal electronic components can still cause energy loss, making the oscillator unsuitable as a qubit. To truly reach the quantum regime with minimal energy loss, the oscillator must be made from superconducting materials and operated at frequencies below $2\Delta/\hbar$. This would correspond to 87 GHz for aluminum with a Δ_0 of 0.18 meV.

1.4 Overview of loss mechanisms

In this section, we present an overview of the main loss mechanisms limiting the performance of superconducting quantum circuits. These are dielectric losses, quasiparticle (QP) losses due to: thermal radiation, stray infrared light, and microwave-induced pair-breaking, vortex loss, radiative loss, and parasitic modes [46]. All the different circuit components of the superconducting qubit, such as Josephson junctions, capacitors or inductors can host these loss mechanisms to varying degree.

1.4.1 Dielectric loss

Dielectric loss represents one of the most significant challenges in state-of-the-art superconducting circuits, often serving as the primary source of decoherence and energy dissipation [47]. This loss mechanism originates from the fundamental interaction between electric fields and structural defects that naturally occur within dielectric materials.

The root cause lies in the atomic structure of these materials and not in the chemical composition [48]. Unlike crystalline solids, which exhibit long-range atomic order, amorphous dielectrics lack this long-range order, as shown in Fig. 2.2. This structural disorder creates numerous defect sites that can interact with electromagnetic fields. However, even crystalline materials are not immune to such loss: they contain their own imperfections such as dislocations, impurities, and grain boundaries that contribute to dielectric loss. Also, piezoelectric materials will be very lossy because they couple electric fields to phonons.

The response of materials to alternating electromagnetic fields can be given using the complex permittivity ϵ, which is defined as the ratio of the the dielectric displacement $\mathbf{D}$ to the applied electric field $\mathbf{E}$:

$$\epsilon = \epsilon' + i\epsilon'' \tag{1.20}$$

where the real part ϵ' represents the material's capacity to store electrical energy: this is the familiar dielectric constant encountered in basic electromagnetism. The imaginary part ϵ'' quantifies energy dissipation within the material. A particularly useful metric for characterizing material losses is the loss tangent $\tan\delta$, which provides a measure of how much energy is lost in the material. Geometrically, this quantity corresponds to the phase angle between the dielectric displacement and electric field vectors. The loss tangent is defined as:

$$\tan\delta_{\text{dielectric}} = \frac{\epsilon''}{\epsilon'} \tag{1.21}$$

Loss tangent allows for comparison between different materials and values for materials commonly found in superconducting circuits are presented in Table 1.1. Higher value of loss tangent indicates higher losses.

1.4.1.1 Concept of participation ratios

The participation ratio model provides a quantitative framework for analyzing dielectric loss in complex device geometries. This approach treats the total dielectric loss as a weighted sum of contributions from each material region, where each region has its

Material	$\tan\delta$	Reference
Vacuum	0	
Sapphire	1×10^{-6}	[49, 50]
Silicon oxide	1.7×10^{-3}	[51]
Niobium oxide	$(9.9 \pm 0.6) \times 10^{-3}$	[52]
Tantalum oxide	$(15.9 \pm 0.7) \times 10^{-4}$	[5]

Table 1.1: Loss tangent values for commonly used materials in superconducting circuits. Note that $\tan\delta$ is a materials property. However, in order to connect to a device loss tangent, for example from dielectric loss, we need to include the participation ratio, cf. Eq. (1.24).

own loss tangent. The model begins by calculating the electric field energy stored in each region of interest. For a n^{th} dielectric volume V_n, the stored energy is:

$$U_n = \frac{1}{2}\int_{V_n} \mathbf{E}.\mathbf{D}dV \tag{1.22}$$

The participation ratio p_n quantifies what fraction of the total electromagnetic energy resides in region n. Using the relation $\mathbf{D} = \epsilon_n \mathbf{E}$ and substituting into Eq. (1.22), the participation ratio becomes:

$$p_n = \frac{\int_{V_n} \epsilon_n |\mathbf{E}(\mathbf{r})|^2 d\mathbf{r}}{\int_V \epsilon |\mathbf{E}(\mathbf{r})|^2 d\mathbf{r}} \tag{1.23}$$

Once the participation ratios are known, the total dielectric loss tangent can be expressed as:

$$\tan\delta_{\text{dielectric}} = \sum_n p_n \tan\delta_n \tag{1.24}$$

This linear superposition allows engineers to identify which material regions contribute most significantly to the overall loss and guides material selection and circuit design optimization strategies.

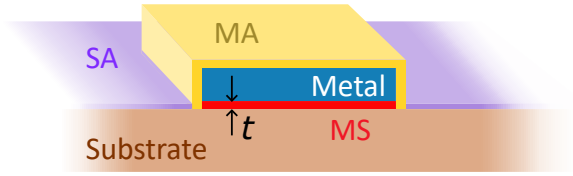

Figure 1.4: Cross section schematic of metal on substrate. The metal-air (MA), metal-substrate (MS) and substrate-air (SA) interfaces with thickness t are highlighted in different colors.

1.4.1.2 Bulk vs. surface dielectric losses

The practical implementation of superconducting microwave resonators introduces additional complexity to the dielectric loss picture. These devices typically consist of metallic films deposited onto dielectric substrates, most commonly single-crystal sapphire due to its exceptional purity and low defect density. The metal surfaces are inevitably covered with native oxide layers - thin amorphous films that form naturally upon exposure to air. In some designs, resonators may incorporate multiple metallic layers, creating a complex multilayer structure. For better understanding of dielectric loss in a device, it can be categorized into two distinct contributions: bulk and surface losses.

Bulk dielectric loss originates within the substrate material itself. For high-quality sapphire substrates, this loss mechanism is typically well-controlled due to the crystalline perfection and ultra-low impurity levels. The single-crystal structure minimizes structural defects, while careful purification processes reduce impurity concentrations to parts-per-million levels. This makes substrate selection a powerful tool for minimizing bulk contributions to the overall loss budget.

Surface dielectric loss, in contrast, arises from the numerous interfaces present in the device. These interfaces are metal-substrate (MS), metal-air (MA), substrate-air (SA) and metal-metal interfaces in multilayer structures. These interfaces contain surface oxides and metal-substrate boundaries that are inherently difficult to control during material deposition and circuit fabrication processes and make surface losses particularly challenging to control. The structural disorder and chemical complexity at these interfaces make them the primary sources of dielectric loss, driving significant research in understanding and mitigating these mechanisms.

A cross section schematic of typical metal electrode on a substrate is illustrated in Fig. 1.4 where both bulk regions (metal and substrate) and interface regions (MS, MA and SA) are highlighted in different colors. While the substrate dominates the total dielectric volume due to its large size, its exceptionally low loss tangent means it contributes minimally to the overall loss budget [50]. Note that value of $\tan\delta$ for sapphire is approximately 10^{-6} whereas it is 10^{-3} for interfaces like surface oxides.

These dielectric losses exhibit distinctive behavior that provides important clues about their physical origin. At mK temperatures, the operating regime for most quantum devices, interface losses become the dominant decoherence mechanism. Interestingly, these losses tend to saturate at elevated temperatures, suggesting a quantum mechanical origin rather than classical thermal activation. The losses also show dependence on frequency, temperature and microwave power.

1.4.1.3 Two-Level Systems: The microscopic origin of dielectric loss

The microscopic mechanism behind dielectric losses is commonly modeled using two-level systems (TLS), originally described by Anderson's phenomenological tunneling model [53]. These TLS can be visualized as atoms or as groups of atoms that can tunnel quantum mechanically between two nearly degenerate energy states. Crucially, these systems can be located at metal-substrate interfaces, within bulk materials, or on surfaces, making them ubiquitous throughout the device structure.

The loss mechanism operates through the following process: TLS can absorb microwave photons from the resonator, causing them to tunnel to their excited state. When this excited state subsequently relaxes, it may release energy in a form that does not contribute constructively to the resonator mode, thereby representing a loss channel. A comprehensive review by Müller *et al.* [54] provides a detailed overview of TLS.

Understanding the TLS loss mechanism opens several avenues for loss reduction. Since TLS interact with the local electric field through their electric dipole moments, reducing the participation of fields in suspected loss regions can significantly decrease energy available for TLS excitation. Among circuit elements, only capacitors contribute significantly to TLS [55]. Therefore, one approach involves increasing the footprint of capacitive elements, which naturally reduces the electric field participation in high-loss interface regions. An extreme example of this principle is the use of three-dimensional waveguides [56, 57], where the electromagnetic field propagates primarily through vacuum rather than through lossy materials. This approach isolates material-related losses and allows for their systematic study while achieving ultra-low loss operation.

The motivation for exploring new materials stems directly from this understanding—the goal is to identify dielectrics with inherently fewer TLS or TLS with reduced coupling to electromagnetic fields. This explains why ultra-pure sapphire substrates are preferred: their crystalline perfection and low impurity content minimize bulk TLS density.

The dominance of TLS-related losses in superconducting circuits is supported by a key experimental signature: the internal quality factor Q_i typically increases with photon number, consistent with the saturation behavior expected from TLS at higher drive powers. This power dependence has become a standard diagnostic tool for identifying TLS-limited devices in the quantum circuits community. However, this remains a matter of debate: other loss mechanisms that saturate with power exist, such as excess quasiparticles [58], which are discussed in the next section.

1.4.2 Quasiparticle loss

1.4.2.1 Thermal quasiparticles

At temperatures above absolute zero, some Cooper pairs in a superconductor can break apart, forming quasiparticles. As a result, the superconductor contains both bound Cooper pairs and a population of unpaired conduction electrons. Unlike Cooper pairs, QPs are not bound and can scatter, contributing to energy dissipation.

When high-frequency electromagnetic fields are applied, QPs get accelerated by the field, but suffer energy loss due to scattering. This behavior is described by the two-fluid model, which treats the superconductor as a mixture of a lossless superfluid (Cooper pairs) and a dissipative normal fluid (QPs). The electrodynamic response of superconducting films under such conditions is characterized by a complex conductivity: the real part accounts for energy dissipation due to QPs, while the imaginary part corresponds to a purely inductive response, characterizing the kinetic inductance of the superconductor.

At any temperature T, the density of thermal quasiparticles, $n_{qp}(T)$ is described using the Fermi-Dirac distribution function $f(E)$. In the low-temperature limit, $T \ll T_c$, this density is well approximated by:

$$n_{qp}(T) = 2N_0\sqrt{2\pi k_B T \Delta_0}e^{-\Delta_0/k_B T} \tag{1.25}$$

where, N_0 is the single spin electron density of states at the Fermi level, and Δ_0 is the superconducting energy gap at $T = 0$. According to Eq. (1.25), at mK temperatures, thermal energy is much lower than the superconducting gap, leading to an exponentially small QP density. Unfortunately, in practice a non-equilibrium population persists even at the base temperature of dilution cryostats, which is discussed in the next section.

1.4.2.2 Non-thermal quasiparticles

Also known as non-equilibrium quasiparticles, these can arise through several mechanisms other than thermal excitations, including pair-breaking from cosmic and environmental radiation with energy $> 2\Delta$. Another relevant mechanism, especially for our devices, involves pair-breaking due to the microwave signal used to measure resonators. This happens when a microwave signal with a frequency $\hbar\omega < 2\Delta$ interacts with the resonator, leading to absorption by QPs in the metallization. This results in redistribution of the QP distribution function $f(E)$, causing the emission of phonons that possess energy greater than 2Δ, thereby breaking Cooper pairs [23, 59, 60]. Recently, Anthony-Petersen *et al.* [61] demonstrated that thermal contraction-induced stress and vibrations in the cryostat [62] has the potential to generate non-equilibrium QPs.

1.5 Materials for superconducting quantum circuits

So far, we've understood that constructing reliable qubits requires materials with minimal or zero energy dissipation. The basic requirement is to use a superconducting material with a reasonably high critical temperature. This raises an obvious question: Can any superconductor be used to build qubits? In practice, not all superconductors are suitable. Also, we shall see that while superconductivity is a necessary condition for qubit materials, it's far from sufficient. To achieve long qubit coherence times, the material must meet additional criteria which are as follows:

- **Chemical stability**: The material should not corrode easily under ambient conditions. Chemically stable materials also allow for harsh cleaning procedures (Section 3.5).
- **Stable surface oxide**: Many of the dominant energy loss mechanisms in qubits come from interfaces: such as between the metal and substrate or within the Josephson junction. To minimize these losses, the superconductor should form a thin and self-passivating low-loss surface oxide, which helps reduce dielectric loss and improve device performance. In addition, absence of magnetism in the surface oxide is also important [63]. This requirement already eliminates many superconducting materials from consideration.
- **Low microwave loss**: In the operating frequencies in the range 4 GHz to 20 GHz.
- **Material purity**: The purity of the superconductor can influence its properties, including its critical temperature and surface loss. In particular, magnetic impurities such as Fe and Ni, can locally suppress the superconductivity. However, high purity isn't always necessary; materials like granular aluminum, which contains a large oxygen fraction, have still been successfully used in quantum circuits.
- **Well behaved thin-film properties**: Since superconducting qubits are fabricated using standard lithography techniques, the material should form high-quality thin films when deposited on a substrate. The films should be uniform, adherent, and structurally stable.
- **Compatibility with nano-fabrication**: The material must be compatible with micron- and nanometer-scale fabrication with reproducible outcomes, as qubit components like Josephson junctions and capacitors are defined with sub-micron resolution.
- **Magnetic field resilience**: High critical field is a useful property, as magnetic fields can be used to change Hamiltonian in-situ, particularly for hybrid applications.

Material	T_c (K)	H_c(mT)	ξ_0(nm)	λ_0(nm)	Δ_0(meV)
Al [65]	1.18	10.5	1600	50	0.18
Nb [65, 66]	9.25	198	40	85	1.5
NbN [65, 66]	16	15	5	200	2.4
NbTiN [67]	upto 17				
TiN [68]	4.86		289		0.73†
grAl [69]	2.3⋆				0.34†
Ta [66, 70, 71]	4.4	830	90	54	0.67†

Table 1.2: Superconducting parameters for commonly used materials.
† calculated using $\Delta_0 = 1.76 k_B T_c$
⋆ T_c values depend on the film resistivity

- **Absence of low-temperature phase transformations**: This refers to allotropic transformations that occur at low temperature, impacting the structural, electrical, and mechanical properties of the material. A well-known instance is tin-pest, where the stable β-tin (with BCC crystal structure) converts into a brittle crumbly α-tin (FCC crystal structure) at temperatures below 13.5 °C, leading to volume increase and disintegration of samples [64].

Therefore, only a small subset of superconductors meet all the above mentioned requirements, which is why materials like aluminum, niobium, and tantalum are predominantly used in current state-of-the-art devices. Aluminum and niobium have been well-established for many years, while tantalum has become more popular in recent years. While there are also several material platforms based on superconducting alloys, like niobium nitride (NbN), titanium nitride (TiN) [32, 33], NbTiN, in the following section, we will limit the discussion to three main elemental materials Al, Nb and Ta as well as the sapphire substrate, with a focus on material related loss contribution to the qubit performance. Since Ta is the central focus of this thesis, it will be discussed in greater detail compared to Al and Nb.

1.5.1 Sapphire substrate

Before we move on to the other two materials, at this point, it is relevant to introduce the crystal structure of sapphire, which is particularly important in the context of tantalum-based devices. Sapphire has a rhombohedral crystal structure but in the literature, it is often described using a larger hexagonal close-packed (HCP) crystal structure as shown in Fig. 1.5, as it is more convenient to visualize leading to an easier understanding of the crystal structure. Even this larger HCP unit cell is formed by arrangement of three primitive hexagonal unit cells. The HCP lattice constants of the primitive unit cell are

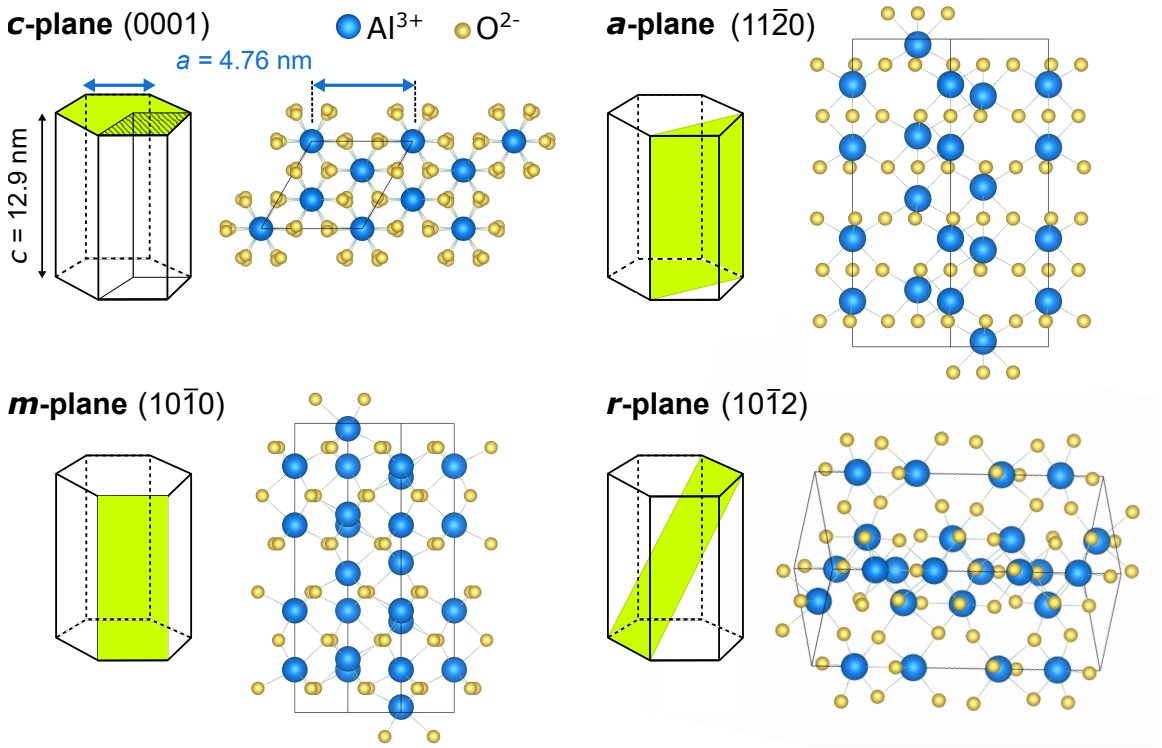

Figure 1.5: Lattice planes of sapphire crystal: *c*-, *a*-, *m*- and *r*-planes are highlighted in green within the hexagonal unit cell. Adjacent to each hexagonal unit cell, the layout of oxygen and aluminum atoms on these planes is illustrated from a top-down perspective. The black lines in the atomic layouts represent the actual primitive hexagonal unit cell marked as a shaded rhombus, for 2D-representation, in the *c*-plane.

$a = 4.76\,\text{Å}$ and $c = 1.299\,\text{nm}$ [72]. Sapphire single crystals are widely used as substrates in thin-film deposition, and the four most common crystallographic orientations are : $c-(0001)$, $r-(10\bar{1}2)$, $a-(11\bar{2}0)$ and $m-(10\bar{1}0)$, and are shown in Fig. 1.5.

1.5.2 Aluminum

Aluminum is the most extensively utilized material for superconducting quantum devices. It is also the most abundant material available as compared to Nb and Ta. Its critical temperature and superconducting length scales are given in Table 1.2. Al can be formed into thin-films using several physical vapor deposition techniques such as thermal evaporation [73], sputtering [74] and electron beam evaporation [75, 76].

One key reason for the widespread use of Al in superconducting circuits is its oxide. When exposed to air, Al forms a self-limiting, stable and robust surface oxide Al_2O_3 that is only few nanometer thick, making it ideal for use as a tunneling barrier in Josephson junctions. From one of the first qubits demonstrated by Nakamura *et al.* [77] in 1999 to

the latest advancements by Place *et al.* [1] and Wang *et al.* [2], aluminum oxide has been consistently used to form tunnel junctions. Moreover, Josephson tunnel junctions based on aluminum oxide have been under study for a much longer time prior to the advent of the superconducting qubits since the 1960's [78].

Al crystallizes in a face centered cubic (FCC) structure with a lattice constant of 4.05 Å [66]. A key advantage of Al in superconducting qubit fabrication is that the qubit performance is largely independent of Al microstructure. Unlike Ta and Nb, high-quality crystallinity and microstructure are not essential for achieving long coherence times in Al-based qubits. In fact, Al films are generally straightforward to deposit through thermal evaporation, due to its relatively high vapor pressure, in high vacuum conditions without the need for elevated substrate temperatures. The structural properties of Al film depend on the growth conditions and the resulting films can be polycrystalline or even epitaxial [76].

Comparing to materials like Nb and Ta, Al has the lowest T_c at 1.18 K and lower superconducting gap, yet it performs well in qubit applications. This indicates that a high T_c is not strictly necessary, as long as Δ remains sufficiently above the operating photon energy scale in GHz regime, $\hbar\omega \ll \Delta$. Additionally, the T_c of Al can be enhanced by introducing disorder, particularly oxygen impurities, forming granular aluminum (grAl) which is a matrix of ≈ 3 nm grains of pure Al partially separated by AlO_X [79]. T_c of such a material varies with the film resistivity and forms a dome shaped behavior with a maximum of ≈ 2.3 K [69]. Additionally, Al films exhibit the uncommon behavior of enhanced T_c with decreasing film thickness [80].

Internal quality factor values of the order of several 10^5 are routinely observed for Al devices. The commonly used substrates for Al devices are c-plane sapphire and silicon. Some of the best performing planar resonators have shown Q_i exceeding 10^6 in the single photon regime, which has been achieved in planar Al resonators on sapphire [74] as well as on silicon substrates with an additional substrate etching step [81].

1.5.3 Niobium

Niobium is a refractory metal and it becomes superconducting at approximately 9.2 K, the highest T_c among elemental superconductors. Nb crystallizes in body-centered cubic (BCC) structure with a lattice constant of 3.3 Å [66].

A key distinction between Al and Nb lies in the importance of Nb's film microstructure, which must be carefully controlled to achieve high-quality films. Nb is typically deposited as an epitaxial film to optimize its superconducting properties [82]. High structural quality films can be grown using magnetron sputtering or MBE. The resulting film properties, such as grain size, crystallinity, and defect density, are highly sensitive to growth parameters [83]. For instance, a temperature range of approximately 750 °C to 900 °C

is required to obtain films with high crystallinity [84]. Though this does not always correspond to reduced microwave loss, indicating a complex interplay between structural and microwave performance[85]. Additionally, the orientation of substrate plays a role in determining the preferred epitaxial orientation of the Nb films.[86]. For example, c-plane sapphire typically promotes the growth of (110)-oriented Nb at moderate temperatures, while further increases in temperature can lead to a transition toward (111)-oriented growth.

Nb offers advantages over Al for superconducting qubit applications due to its high superconducting gap and T_c, which make it less susceptible to quasiparticle induced losses. While Nb is a superior superconducting material in many respects, its native oxide is problematic. Unlike the well-behaved and stable aluminum oxide (Al_2O_3), Nb can form several oxides such as NbO (a superconductor with $T_c = 1.38\,\mathrm{K}$, NbO_2 and Nb_2O_3 [87]. As a result, Nb is commonly used for the non-junction elements of a qubit, while aluminum oxide is used for tunnel barrier in Josephson junctions to avoid lossy Nb oxides [31]. Further improvements in coherence have been achieved by encapsulating the Nb surface with Ta, which has led to lifetimes of 300 µs [39] and more recently, over 500 µs without any surface encapsulation [30].

Nb is compatible with acid surface treatments like buffered oxide etch (BOE) to etch away or reduce the amorphous surface oxide after device fabrication. For more details on BOE, see Section 3.5. Planar resonators fabricated from Nb that went through BOE treatment have shown Q_i as high as 6×10^6 [52, 88].

1.5.4 Tantalum

Ta is also a refractory metal with atomic number 73. It lies below well known metal niobium in the periodic table; all nearest neighbors are shown in Fig. 1.6. Tantalum is known for its chemical inertness to acids, a property useful for this work.

Figure 1.6: Ta and its neighboring elements in the periodic table (left). Image of Ta (right).

In contrast to Al and Nb, a peculiarity of Ta is the existence of two different crystallographic phases, when in thin films. The two well known phases are called alpha and

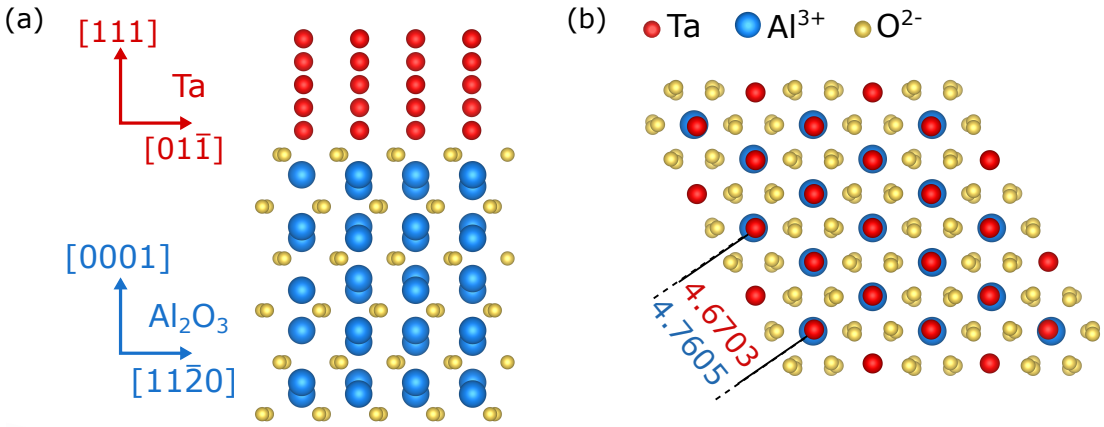

Figure 1.7: Lattice matched crystallographic planes of Ta and sapphire: layout of α-Ta atoms on c-plane sapphire where the α-Ta[111] || Al_2O_3[0001] when viewed from (a) side and (b) top. The units of distance between Ta-Ta and Al-Al atoms in (b) is in Å.

beta [34]. The α-phase, which is thermodynamically stable, has BCC structure similar to that of Nb, with a lattice constant of 3.3 Å [89]. In contrast, the β-phase is metastable and is often found in thin films. It has tetragonal structure with lattice constants $a = b$ =10.2 Å and c = 5.3075 Å [34, 90]. It is noteworthy to highlight that the β-phase possesses a complex, non-primitive tetragonal unit cell comprising a total of 30 Ta atoms as shown in Fig. 2.9. Identifying the phases present in tantalum thin films is crucial, as the two phases exhibit distinct physical and electronic characteristics [91]. The room temperature resistivity of α-phase is typically in the range 10 − 30 µΩ cm whereas, the β-phase shows an order of magnitude higher resistivity, in the range 180 − 200 µΩ cm [34, 91]. Both phases become superconducting, the α-phase has a bulk T_c of 4.4 K, while the β-phase has a significantly lower T_c of 0.5 K [35].

When depositing Ta films using the commonly employed sputtering technique, the β-phase forms readily under typical conditions, as it can form on substrates held near room-temperature[36]. In contrast, high substrate temperatures typically above 300 °C are required to stabilize the α-phase and achieve high quality films. Due to this need for high-temperature processing, sapphire is a widely used substrate, as it allows for heating to high temperatures without decomposition and inter-diffusion with the film material to be deposited. Alternatively, introducing a seed layer of structurally compatible materials such as Nb, Ti, TaN, TiN, or Cr can promote desired growth [92–94]. There is also growing interest in using silicon substrates as a potential replacement for sapphire. However, Ta forms silicide with silicon at elevated temperature.

Epitaxial films of Ta can be grown on sapphire similar to Nb. Depending on the plane of sapphire, as shown in Fig. 1.5, in combination with heated substrates, the α-phase can grow with specific preferred orientations. The c-plane sapphire is expected to promote α-phase growth along (111) direction with low lattice mismatch. Fig. 2.9 illustrates the (111) plane among other planes within the α-phase lattice. Figure 1.7 show the

arrangement of Ta atoms stacked on *c*-plane sapphire with $\alpha(111) \parallel Al_2O_3(0001)$. The top view of same arrangement reveals a precise alignment of Ta atoms with Al atoms in the sapphire. It has been observed that $\alpha(110)$ and a mix of $\alpha(110)$ and $\alpha(111)$, is also supported by *c*-plane sapphire [95]. In the intermediate temperatures around 500 °C, the $\alpha(110)$ orientation forms and further heating leads to nucleation in $\alpha(111)$ orientation.

Given its comparatively higher T_c compared to β-phase, the α-phase Ta has emerged as a favorable material for superconducting circuit applications. This interest has been fueled by the demonstration incorporating tantalum in the shunting capacitor pads of 2D transmon qubits which have achieved lifetimes upto 500 µs [1, 2]. A lot of research has gone into optimizing the growth of high-quality tantalum films and understanding the underlying mechanisms driving this performance improvement. Much of the recent work has concentrated on stabilizing α-phase films grown on *c*-sapphire [5, 96–98], *a*-sapphire [99, 100] or silicon [30, 92, 93, 97, 98]. It has become evident that the superconducting and structural quality of the films—reflected in properties like T_c, residual resistance ratio (RRR) and surface morphology can vary significantly even within the same phase and orientation. Factors such as substrate choice, surface preparation, deposition conditions, and subsequent fabrication or post-processing steps all play critical roles in determining film quality.

The observed improvements in qubit lifetimes are attributed to the formation of a stable, self-limiting surface oxide [38, 39]. Tantalum readily forms an amorphous Ta_2O_5 of 3 nm to 5 nm thickness when exposed to air, though there are many other oxidation states possible like Ta_2O_3, TaO, Ta_2O etc [101]. Several studies suggest that Ta-oxide is superior to Nb-oxide for such applications [39, 102]. Notably, Ta tends to form fewer suboxides than Nb [38] or no suboxides [103]. Ta_2O_5 also exhibits a simpler structure and a near-crystalline character, which contributes to a reduction in TLS defects. Furthermore, it displays a more abrupt transition between oxidation states and a bonding nature that closely resembles its crystalline phase. These properties inhibit hydrogen diffusion and help minimize loss-inducing defects [103].

In a study conducted by Frost *et al.* [104] to examine the oxide characterization shortly after film deposition, they found that the growth rate of oxide on Ta is initially slower in the first $\approx$ 1 h and it then shifts to a faster rate. However, such a change in oxidation rate does not occur with Nb. To prevent the surface oxide formation, Ta surfaces can be covered with materials like Mg [105], Au, or AuPd [106]. Nevertheless, there have been no reports so far indicating a reduction in losses due to oxide removal. Ta/Ta-oxide/Ta tunnel junctions have been demonstrated by Lam *et al.* [107], who also reported the formation of epitaxial Ta_2O_5 [101]. Despite these advances, the fabrication of high-quality tunnel junctions based on Ta or Nb remains an area requiring further investigation.

To date, the β-phase has not been thoroughly studied, often due to its low T_c. Nonetheless, it would be interesting to explore it as the T_c is larger than the operating temperatures of few mK. Urade *et al.* [92] reported quality factor of $\approx 10^5$ for β-phase Ta deposited on unheated Si substrates. Consequently, exploring β-phase Ta presents a novel opportunity to assess its suitability in superconducting circuits and to determine whether it truly presents challenges or if it can be effectively integrated into high-quality circuits. Not only that, its high resistivity and low superconducting gap makes β-Ta an interesting candidate for kinetic inductance detectors [108]. In this thesis, we explore Ta grown on *c*-plane sapphire. We include films with pure α-phase growing with both (110) and (111) orientation as well as films containing a mixture of α- and β-phase.

1.6 Thesis outline

In this thesis, I characterize microwave losses in Ta resonators and identify the material properties that make Ta suitable for low-loss quantum circuit applications. The focus is on measuring resonators to gain insights into material-related loss aspects. To thoroughly study the impact of various material properties on resonator performance, we utilize Ta films with structural and electronic attributes that were deposited at KIT, as well as those obtained from collaborators from ENS Paris and University of Innsbruck. The subsequent sections of this thesis are organized as follows:

Figure 1.8: Process flow followed in this thesis showing how film growth parameters influence material properties, which in turn determine microwave resonator performance.

Chapter 2 elaborates on the different Ta films used in this study and their synthesis methods. It begins with an overview of magnetron-sputtering technique for thin film deposition, followed by a comprehensive description of the deposition setup used at KIT. This is followed by a detailed characterization of the various films using a range of standard and special techniques.

Chapter 3 outlines the lithography fabrication process for patterning lumped element resonators. It includes the design of resonators and the 3D-waveguide sample holders, with simulations using finite elements simulation software to predict the frequency and coupling to the waveguide electric fields beforehand. This chapter also discusses the post-fabrication processing of resonators via buffered oxide etching, along with a brief structural characterization to assess the impact of post-processing on film properties.

Chapter 4 covers the microwave characterization of resonators, aiming to explore the dominant loss mechanisms and link them to the material properties of Ta. It starts with essential concepts for evaluating microwave resonators' quality, followed by an introduction to microwave resonators. Subsequent microwave measurements with a vector network analyzer and circle fitting of data are provided to determine the internal quality factor. The dependence of the quality factor and frequency shift on photon number and temperature is presented, while superconducting parameters like T_c and kinetic inductance fraction are discussed and compared to those obtained from DC measurements in Chapter 2.

2 Synthesis and characterization of high quality tantalum films

This chapter provides a detailed discussion of tantalum (Ta) film deposition and a comprehensive characterization of different Ta films which were deposited under different conditions and at different locations. This leads to films with varied crystalline, surface and superconducting properties. A well understood optimization of sputtering parameters is essential for obtaining good Ta films with low microwave losses. With the aim to correlate film microstructure with the microwave losses, we use multiple techniques to characterize various films. These films were deposited at three different locations summarized in Table 2.1. Films at KIT were deposited by myself, and at ENS, Paris by José Palomo.

Initial characterization of the films was carried out using readily available techniques like x-ray diffraction (XRD) to check the films' crystallographic phase and orientation, four-probe DC transport measurements to determine the superconducting transition temperature T_c and atomic force microscopy (AFM) to examine the film's surface morphology. After developing a deposition recipe that yields films with a desired T_c close to that of bulk Ta, we proceed to fabricate resonators from those films and subsequently measure them, which forms the subject of Chapters 3 and 4. Only after high-quality factors in these resonators were achieved, more advanced characterization techniques were employed for these films. We used scanning transmission electron microscopy (STEM) and automated crystal orientation mapping (ACOM), which is a technique based on STEM, for detailed microstructure at film surface and various interfaces. To study superconducting properties, superconducting quantum interference device (SQUID)

Deposited at	Ta phases in the films
KIT	$\alpha(110)$, $\alpha(111)$, $\alpha(110)+\alpha(111)$, $\alpha(110)+\beta(002)$
ENS, Paris	$\alpha(110)+\beta(002)$, $\beta(002)$
Star Cryoelectronics	$\alpha(110)$

Table 2.1: List of labs where Ta films were deposited along with the growth phase and orientation in the films deposited in each lab. The '+' denotes the presence of multiple phases and orientations within a single film.

magnetometry and scanning tunneling microscopy (STM) were employed, while time-of-flight secondary ion mass spectrometry (ToF-SIMS) was used to identify material impurities, such as magnetic materials.

2.1 Tantalum film deposition

Tantalum deposition has a long history, starting with electro-deposition in the 1920s [109], and later by thermal evaporation techniques [110, 111]. From the 1960s onward, extensive studies have been going on sputter-deposited Ta films [34, 112, 113], with a particular interest in exploring its two different crystallographic phases. Over the years, Ta films have found use in various applications such as photon detectors for astronomy [114, 115], electronic components like capacitors [116] and resistors [117], as implant material [118], and as coatings [119, 120]. Most relevant to us, they have been also used in circuit quantum electrodynamics [121]. More recently, tantalum has gained significant interest from the community by demonstrating improvement in superconducting quantum circuits [1, 2]. Achieving high-quality Ta films involves careful consideration and optimization of various factors, including the choice of substrate, its quality and cleanliness, and several deposition parameters. Therefore, optimizing the deposition process of tantalum films remains an important step towards achieving high-coherence quantum devices.

First, the concept of magnetron sputtering is briefly introduced, discussing the different deposition parameters. Then, we describe the sputtering setup used at KIT and compare it to the one used at ENS. This is followed by discussion of the actual range of parameters used for the films at KIT and ENS. Owing to the commercial nature of Star Cryoelectronics films, the details of deposition parameters are not readily available, and hence are excluded from the discussion.

2.1.1 DC magnetron sputtering

The physical-vapor deposition (PVD) techniques of sputtering developed in 1850s to late 1800s as vacuum and electrical power technologies improved [122]. W.R. Grove's work in 1852 is credited to demonstrate the phenomenon of sputtering and its ability to form thin films in a vacuum [123].

Sputtering is a process where energetic ions or neutral particles bombard the target material. This results in momentum transfer between the bombarding ions and the target material, causing atoms to be ejected from the target surface [124]. The ejected atoms travel towards the substrate and condense on it to form a film. The energetic ions are created from sputter gas by applying voltage between two electrodes inside

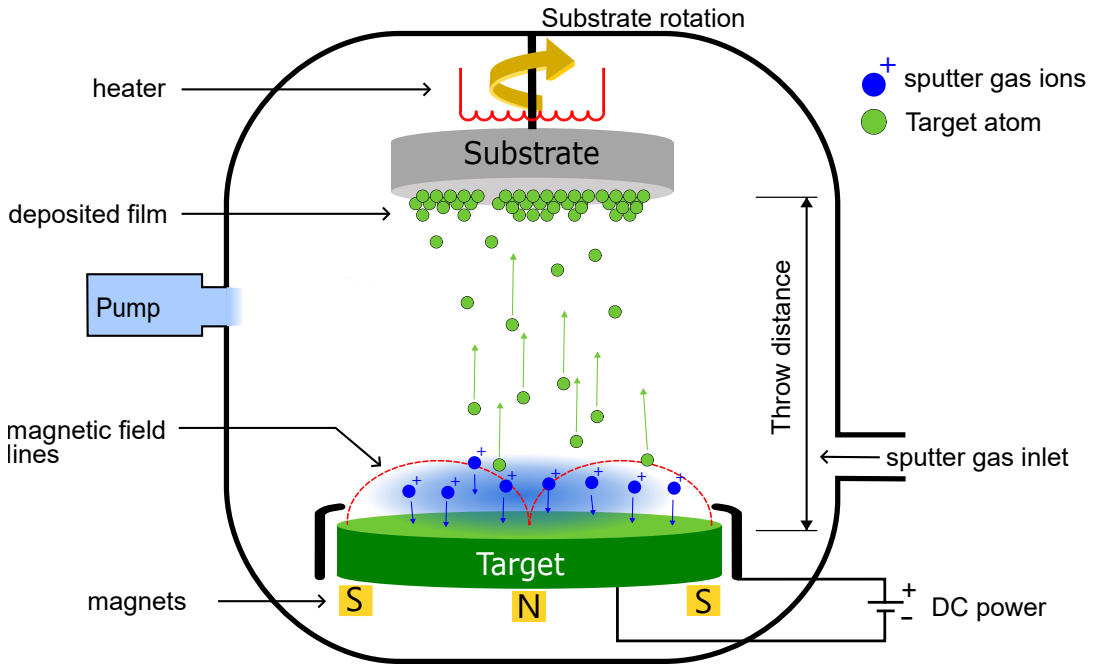

Figure 2.1: Schematics of a sputtering deposition chamber equipped with a target; a substrate; a heater to control the temperature of the substrate; vacuum pump to create vacuum conditions; gas inlet to introduce sputter gas atoms into the chamber; electrodes to ionize sputter gas; magnets behind the target to confine the plasma. The target is bombarded with sputter gas ions (blue), and the ejected/vaporized target atoms (green) travel towards the substrate and condense on it to form a film.

a high vacuum chamber. In magnetron sputtering, magnets are placed behind the target, creating a magnetic field in the vicinity of target surface and confining the plasma near the target. This allows for higher sputter rates at lower gas pressure and voltage as compared to sputtering without magnets. Various deposition parameters that are relevant in film growth are background vacuum, discharge voltage, substrate temperature, dc power, working gas pressure etc. A schematic of the sputtering process is shown in Fig. 2.1.

2.1.2 Sputtering parameters affecting film properties

To understand how deposition parameters influence film properties, examining the growth process and structural evolution during initial film formation is essential. Thin film development proceeds through four distinct stages: nucleation, nucleus growth, coalescence, and film thickening [125].

During nucleation, the incoming vaporized target atoms condense onto the substrate surface as adatoms. These adatoms transfer energy through interactions with the

substrate lattice, allowing them to diffuse across the surface. As more atoms arrive at substrate, they interact with existing adatoms to form small islands of atoms that either diffuse or gradually expand depending on their stability. This stage is known as nucleation growth. The coalescence stage involves the merging of these islands, continuing until complete substrate coverage eliminates all voids. The diffusion process of adatoms on substrate surface fundamentally determines the structure of resulting film. Several deposition parameters influence adatom diffusion. The well known structure zone diagram by Thornton [126] effectively illustrates how expected microstructure vary with substrate temperature and argon gas pressure.

Of the various deposition parameters, substrate temperature is among the most important in the growth dynamics of the films [127]. Higher temperatures provide adatoms with sufficient kinetic energy to diffuse across the surface, allowing adatoms to reach thermodynamically stable equilibrium sites. In contrast, lower temperatures restrict adatom mobility, causing them to become trapped before reaching equilibrium sites. Elevated temperatures also enable impurity desorption from the substrate surface, reducing film contamination and also promoting island coalescence. The kinetic energy of adatoms is also affected by the energy of sputter gas ions and sputtered atoms. Additionally, the deposition rate impacts adatom diffusion; higher rates result in a greater density of islands during nucleation growth. Lastly, the substrate's quality also play a role [84]. Crystal structure of underlying substrate influences the thin film's structure. If the film material's lattice parameters closely match those of the substrate, epitaxial growth may occur, as discussed in the subsequent section.

2.1.3 Epitaxial vs polycrystalline films

During crystalline film growth, the films can exist with different crystal structures while having the same chemical composition, depending on a variety of parameters such as choice of substrate and its orientation, surface conditions, growth temperature, etc. The resulting films can be *epitaxial* or *polycrystalline*, each with different properties. The word epitaxy is derived from *epi-*, meaning "upon" and *taxis*, meaning "ordered". Epitaxial films have higher degree of order within the bulk and at the interface with the underlying substrate crystal. They are further classified into homoepitaxy which refers to growth of a crystalline film of same material as the substrate and heteroepitaxy where the materials of the crystalline film is different than the substrate material. Ta film on Al_2O_3 substrate used in this thesis falls under the category of heteroepitaxy. High substrate temperature favors the epitaxial growth. The crystal order in epitaxial and polycrystalline films is depicted in Figure 2.2. For completeness, an amorphous films is also shown whose structure is defined by complete lack of order.

On the other hand, polycrystalline films are made up of multiple small crystals or grains. Within each grain, the atoms have a specific arrangement. Hence, polycrystalline films

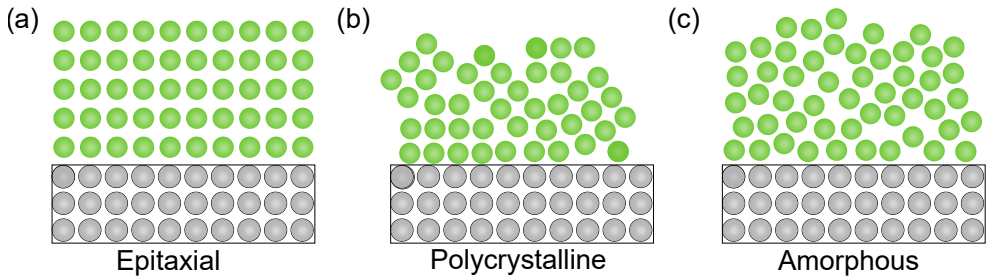

Figure 2.2: Schematic of a film (green) crystal structure on a substrate (gray). (a) Epitaxial film with lattice matching between film and the substrate lattice and long range order in atomic arrangement of the film. (b) Polycrystalline film without lattice matching and several grains orientated in different directions but the individual grains have order. (c) Amorphous film with no order.

only have short-range order. The grains are aligned in different orientations which gives rise to grain boundaries defined as the interface between two adjacent grains. The size of the grains and their orientation can significantly impact film properties. Typically, low to intermediate temperatures are needed to promote polycrystalline growth [125].

2.1.4 Createc sputtering system at KIT

Sputtering is an attractive choice for making Ta thin films. Figure 2.1 a simplified schematic of a sputtering chamber. The important parameters during film depositions that affect the composition, structure and electrical properties of the films are the chamber base vacuum at room temperature (RT), throw distance, pressure and flow of working gas- argon, substrate temperature, sputtering power, DC bias voltage and deposition time.

We use a custom made sputtering deposition system from Createc Fischer GmbH. The deposition chamber and some of the components are shown in Fig. 2.3. It is connected to an ultra high vacuum transfer-line which is further connected to a high vacuum load-lock via a gate valve. The load-lock is designed to be brought at atmospheric pressure. To mount samples inside the chamber, they are first installed to the load-lock while it is isolated from the transfer line. After pumping and bringing the load-lock to $\approx 1 \times 10^{-8}$ mbar, samples can be transferred to the transfer-line and further to the deposition chamber using magnetically coupled, manual transfer arms. This prevents exposing both the chamber and the transfer line to the ambient conditions and hence ultra-high vacuum of less than 1×10^{-9} mbar can be reached inside the chamber and be sustained even when frequently changing samples.

The deposition system is designed specifically for high-quality thin film deposition owing to its large throw distance between the target and the substrate of ≈ 285 mm [129],

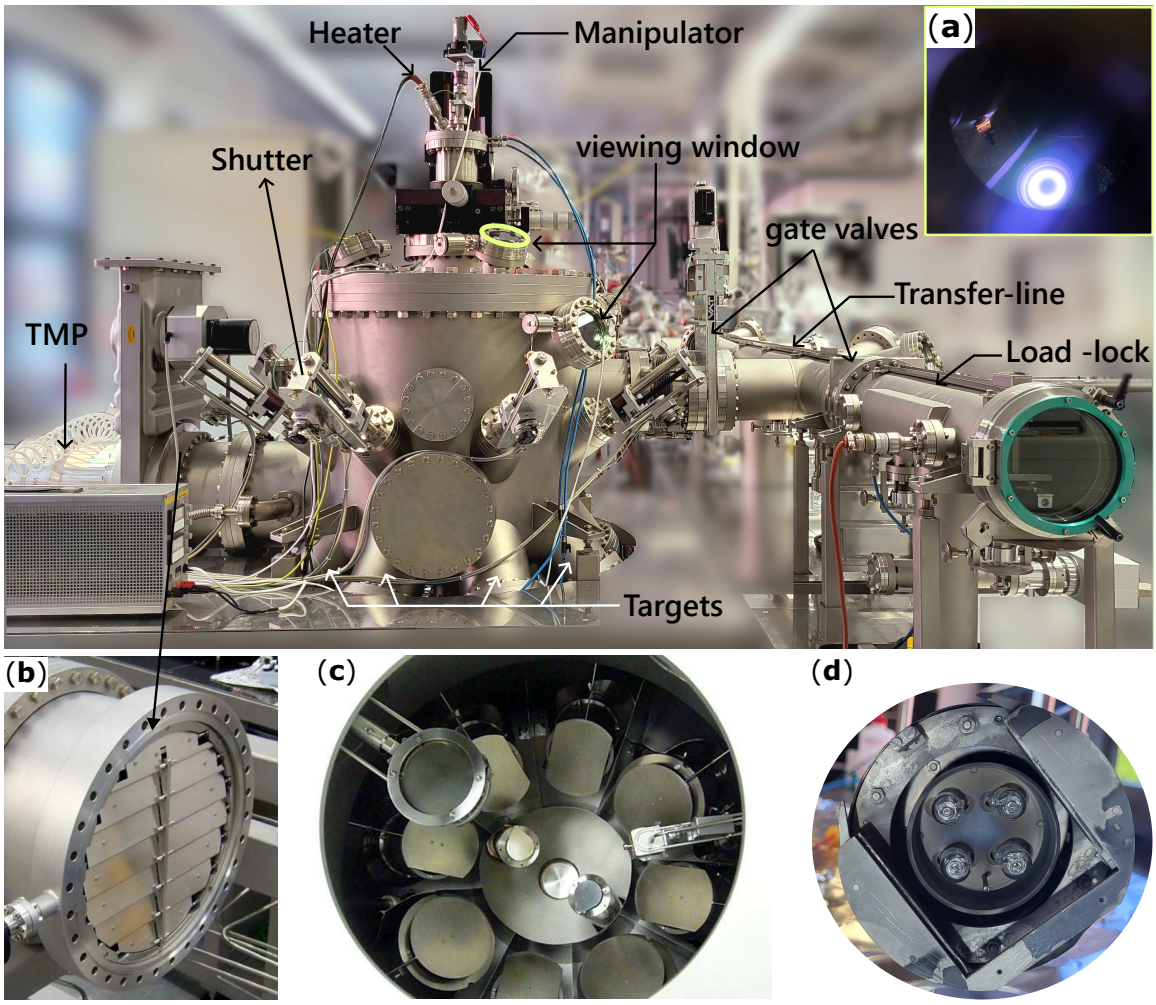

Figure 2.3: Photograph of sputtering deposition chamber used at KIT to deposit Ta films. The chamber is directly connected to the transfer-line via a gate valve on the right and to the pumping on the left. The transfer-line is then connected to the load-lock. Four shutter-controls, four targets and two viewing windows are visible in the front. Manipulator with heater and attached housing for substrate-holder extends from top to center (inside) of the chamber. (a) View of Ta target and plasma around the target during deposition from the glass window highlighted in yellow circle. (b) Throttle valve to regulate working pressure. (c) Top view of the targets through the manipulator port. (d) Bottom of manipulator with heater consisting of a set of 4 halogen lamps. The attached U-shaped housing contains grooves to mount substrate holder shown in Fig. 2.4. (b) and (c) are adapted from [128].

which is notably larger than the mean free path (MFP) of Ar ions, ≈ 50 mm at working pressure of 0.3 Pa. This substantial distance results in lower deposition rates. As sputtered atoms or molecules travel to the substrate through the plasma, they undergo collisions. For large throw distance, sputtered atoms lose energy due to collisions on their way and move diffusively. The energy loss of sputtered atoms can considerably influence the film's microstructure, density, and other characteristics [129–131]. Additionally, the amount of Ar ions reaching the substrate, thereby causing implantation

or damage to the film, is also minimal. The substrate holder is located in the center of the chamber in an on-axis orientation. The angle of incidence on substrate holder is 37.5° with respect to its surface normal. The chamber is equipped with a manipulator that can be heated using a heater consisting of a set of four Halogen lamps as shown in Fig. 2.3(b). The substrate holder can be mounted in the U-shaped grooves at the end of the manipulator. Temperature setting up-to 1000 °C can be set without damaging the lamps. The substrate is heated mostly by radiation and as a result, some heat is lost to the nearby environment. The radiative heating leads to a lower actual substrate temperature than the set temperature of the heater. One disadvantage associated with it is the difficulty to stabilize low temperatures. On the other hand, the quality of the contact between heater and substrate holder is not important, i.e. heating is similar in each deposition.

The set temperature is measured by a thermocouple, not in direct contact with the sample holder, and is also heated radiatively which leads to the inaccurate reading of the substrate temperature. The actual temperature on substrate was measured by attaching an additional thermocouple to the top surface of a loaded sapphire wafer in a separate calibration experiment and the results are shown in Fig. 2.5. To attain higher actual temperature on the substrate, we modify the substrate holder by adding grooves [see Fig. 2.4] which reduce the heat loss of the substrate to the water cooled seat of the sample holder.

Care has to be taken if the deposition chamber has been opened to ambient pressure. Air brings in moisture and hydrocarbons, that can be adsorbed onto the chamber walls and other surfaces. Therefore baking the chamber afterwards is crucial for achieving a high vacuum and minimizing contamination. By heating the chamber, residual gases, moisture, and adsorbed contaminants are released and pumped away, improving the vacuum conditions and the quality of the resulting thin film. Additionally, sputtering of getter materials such as Ti with a high affinity for specific gases can be used to absorb the unwanted gases. The choice of getter material depends on the target materials already available in the chamber. We sputter coat the chamber with Ta using a dummy substrate to protect the heating lamps.

We deposited approximately 200 nm thick Ta films on 2" double-side-polished *c*-plane sapphire using DC magnetron sputtering to have the bulk Ta properties in the films. For KIT films, we used sapphire substrates from Crystal GmbH grown with the Kyropoulos method [132, 133]. The procedure for film deposition at KIT is given below and the deposition parameters of films S1-S5 are summarized in Table 2.2.

1. Substrate preparation: At the beginning, four sapphire pieces measuring 7×7 mm^2 each, were used in combination with a stainless steel substrate holder as shown in Fig. 2.4(b). For this, a 2" sapphire wafer was spin coated with a resist layer for surface protection and was diced into smaller pieces. These pieces were cleaned in acetone bath followed by isopropanol (IPA) to remove the protective resist layer.

Afterwards they were immersed in a Piranha solution for 30 min followed by a 2 min to 3 min of water risning to clean any organic residues. In the next step, the wafers were cleaned in an oxygen plasma using a reactive ion etching (RIE) tool with parameters: O_2 flow- 15 sccm, 30 W, etching time- 2 min, O_2 pressure- 100 m Torr. The substrate cleaning recipe was later changed to a sequential dip in NEP (N-Ethylpyrrolidone), acetone and ethanol for 4 min each. However, Ta deposited on smaller sapphire wafers always resulted in films with α-phase in two orientations (110) and (111) while the aim was to stabilize only (111) orientation of α-phase. As a result, the use of small sapphire wafers was terminated and whole 2" sapphire substrates were used in combination with a different substrate holder as shown in Fig. 2.4. They were cleaned in IPA for 10 min in an ultrasonic bath and dried using a N_2 gun before loading them into the deposition chamber.

2. After the substrate was loaded into the chamber, it was baked overnight using the heating lamps at 300 °C. This heats the substrate above boiling point of water i.e. 100 °C to evaporate moisture and other contamination present on the surface. The base pressure inside the chamber was maintained at 1×10^{-9} mbar at room temperature.

3. The next day, the heater temperature setting was changed to the temperature required for the actual deposition, which in most cases involved heating further to higher temperatures. To obtain α-phase with (111) film orientation, we heat the substrate holder from the backside to 800 °C, which corresponds to substrate temperature of around 530 °C. The manipulator is rotated during deposition at constant speed of ≈ 7 rpm to get homogeneous film thickness.

4. The target was sputter cleaned using Ar plasma for approximately 10 min before the actual deposition while keeping the target shutter closed.

5. The target shutter is opened to start the film deposition.

6. After deposition, the substrate rotation is stopped and the film is cooled down overnight at 2 °C/min inside the chamber. In later depositions, the cooling rate was increased to 20 °C/min.

The film grown at ENS Paris was deposited using the same DC magnetron sputtering technique but in a Plassys deposition setup and with different deposition parameters. The substrate was baked overnight inside the high vacuum chamber at 360 °C and at 5×10^{-8} mbar chamber base pressure followed by a 2 hour baking at 550 °C and 4×10^{-7} mbar. It was then cleaned with Ar plasma for 150 s inside the deposition chamber prior to deposition with following parameters: 20 sccm Ar, 200 V, 34 W and 0.018 mbar. In this setup, the substrate temperature was determined by the temperature calibration curve provided by the sputter deposition system manufacturer. Temperature setting of (400)650 °C at the thermocouple correspond to $\approx$ (360)550 °C. These resulted in a completely different film from structural point of view. This is due to the differences

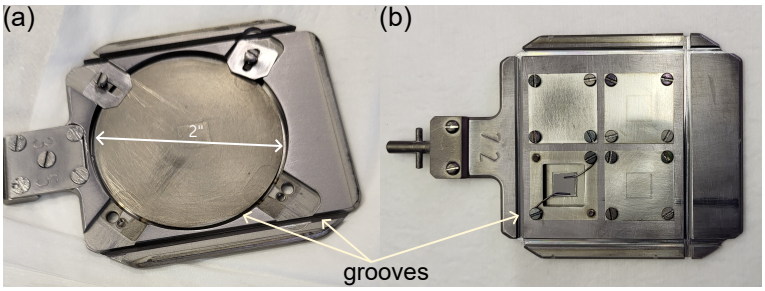

Figure 2.4: Substrate holders designed to accommodate (a) 2" substrate and (b) four substrates measuring 7×7 mm^2 each. There are additional grooves shown by arrows to improve substrate heating.

Parameter \ Films	S1	S2, S3, S4	S5	Fig. 2.6
Temperature (°C)	650†	800*	500*	800*
Ar flow (sccm)	13	44	44	17
Working pressure (mbar)	0.009	0.003	0.003	0.0092
Power (W)	500	200	200	500
Voltage (V)	391	254	254	273
Deposition time	3 min 30 s	62 min	61 min	26 min6 s
Rate (nm/s)	1	0.06	0.06	
Cool-down time (hour)	3	7,1,1	7	
Deposition site	ENS Paris	KIT	KIT	KIT
Resulting Ta phase	α and β	α(111)	α(110)	α(111)+α(110)

Table 2.2: Magnetron sputtering parameters for Ta film deposition. The three cool-down time entries correspond to each one for S2, S4 and S5.
$\star$ Thermocouple temperature † Substrate temperature

in the deposition system such as the dimension of the chamber (also associated with the throw distance) as well as different deposition parameters.

2.1.5 Film comparison across different apparatus

This section compares films deposited in the KIT and ENS deposition chambers. In addition to film S1, three additional films are discussed. First, the films deposited at high temperatures are discussed, followed by those deposited at room temperature.

The attempt to make a similar film with both α- and β-phases using the ENS film recipe yields a completely different film structure. The deposition parameters of this film are

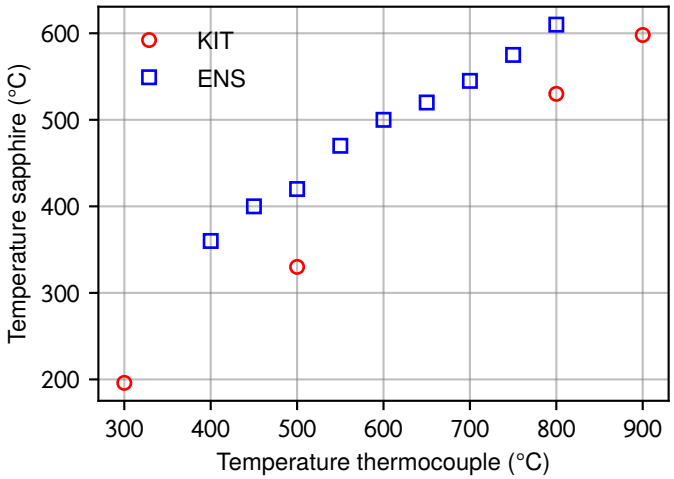

Figure 2.5: Temperature calibration curve for deposition system at KIT and ENS.

shown in the last column of Table 2.2. Figure 2.6 shows comparison of XRD of two Ta films: first deposited at KIT and second at ENS, Paris. The KIT deposited film shows two peaks corresponding to $\alpha(110)$ and a $\alpha(111)$ peak. It does not show any presence of β-phase unlike the ENS deposited film. Both films also have different surface topography as shown This implies that given the same parameters as ENS apparatus, we were not able to achieve the same growth condition in the KIT apparatus.

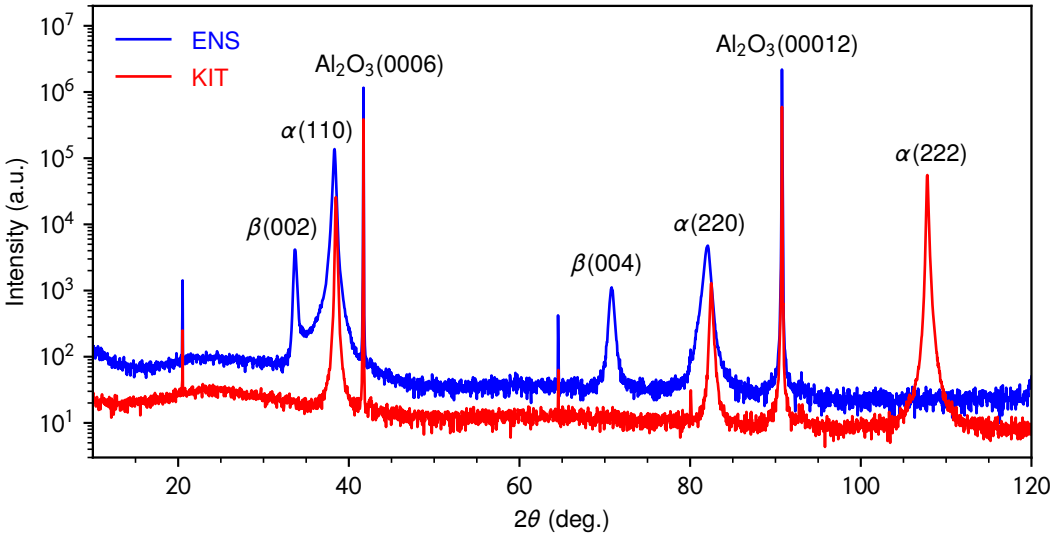

Figure 2.6: Comparison of high temperature deposited films: XRD[1] of two films grown at KIT and ENS. The film deposited at KIT using the ENS film deposition parameters with aim to achieve the same film as ENS.

Room temperature deposition of tantalum films is expected to stabilize β-phase. The two films shown in Fig. 2.7 were specifically grown to achieve the β-phase. The deposition chamber at ENS yields a film with only β-phase with (002) orientation. The deposition

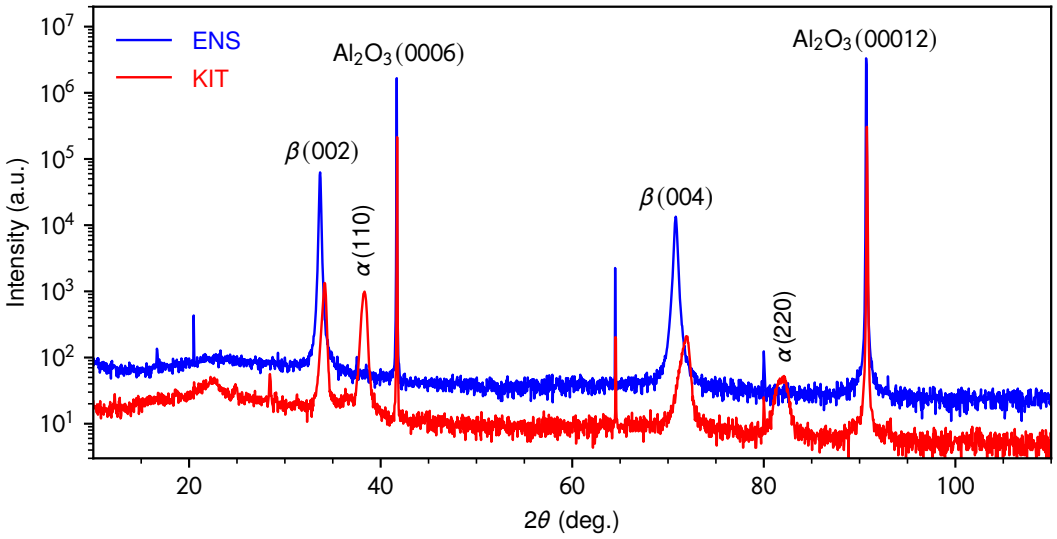

Figure 2.7: Comparison of room temperature deposited Ta films: XRD of two films grown at KIT and ENS at room temperature substrates. ENS film shows only β-phase peaks whereas, KIT film shows two peaks, each for α and β-phase.

parameters for this film are the same as S1, except for the deposition temperature. The films grown using the KIT deposition apparatus also show the β-phase with the same orientation as the ENS film. However, the film additionally has α-phase growing in (110) orientation. The deposition parameters for this film are the same as S2, except for the substrate temperature. This indicates that films deposited at room temperature indeed stabilize the β-phase, though the slow deposition rate might possibly also facilitate the nucleation of the α-phase.

2.2 Crystallographic analysis using XRD

X-ray diffraction is a non-destructive technique for structural analysis of materials. It uses x-ray beams, which are incident onto the atomic planes of the crystal. Since, x-rays have similar wavelength as the inter-atomic spacing in the crystals, they undergo elastic scattering from the atomic planes. The scattered x-rays interfere either constructively or destructively, depending on the distance between atomic planes d and the angle of incidence θ of x-rays with respect to the crystalline plane. The condition for constructive interference is given by Bragg's law [134]:

$$n\lambda = 2d_{hkl}\sin\theta \tag{2.1}$$

[1] All XRD measurement data shown in this thesis were recorded by Dr. Dirk Fuchs at KIT.

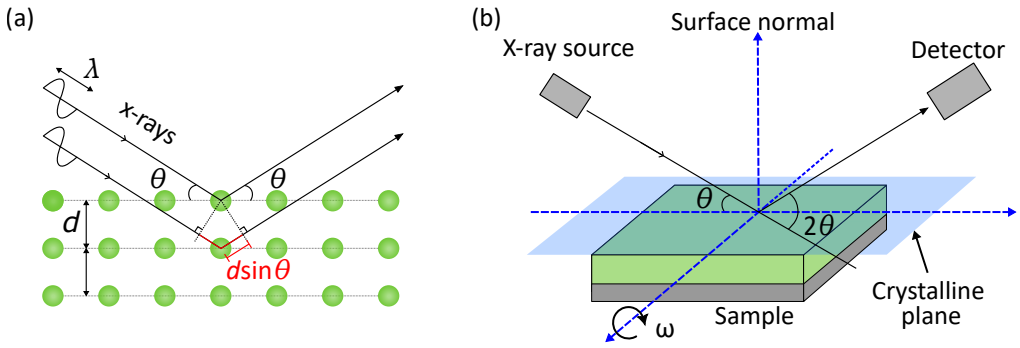

Figure 2.8: Schematics showing working principle of XRD. The relative phase difference between the scattered x-rays is highlighted in red. (a) shows reflection of x-rays of wavelength λ from the atomic planes. The incoming x-rays have angle θ from crystalline planes which are separated by a distance d. (b) shows the axis along which sample is rocked during ω-scan.

where n is the diffraction order and can take integer values, λ is the wavelength of the x-rays, and hkl are the Miller indices of the crystallographic plane. Schematic in Fig. 2.8(a) illustrates the diffraction of incoming x-rays incoming from the atomic planes of the crystal.

The initial approach in XRD is to obtain a $\theta - 2\theta$ scan, where the intensity of diffracted x-rays is plotted against 2θ, angle between the incident x-rays and the detector. Sharp peaks in the intensity indicate constructive interference of scattered x-rays from specific lattice planes. These scans reveal information about phases and their orientations, which are given by the Miller indices. Figure 2.9 shows the powder XRD 2θ scan for α- and β-phase Ta. The data is taken from the Inorganic Crystal Structure Database (ICSD) code 652902 [89] for α-Ta and ICSD code 54208 [90] for β-Ta. In an ideal powder sample, the crystallites are oriented in random directions, resulting in a range of delta function like diffraction peaks. In contrast, for epitaxial films where the crystallites have a preferred orientation, we would expect only single set of peaks.

The next approach is to obtain a ω scan, where the incident angle of x-ray is fixed at the angle corresponding to a particular reflection peak from 2θ scan and the sample is rocked along ω axis as shown in Fig. 2.8(b). The resulting pattern consists of intensity plotted as a function of angle ω and is known as the rocking curve. It shows the broadening of the diffraction peaks and the full-width at half-maximum (FWHM) of the rocking curve is known as mosaicity. It is an important parameter to assess the structural quality and crystalline order in the film. The peak broadening can be caused by various factors such as the misorientation or defects in the lattice planes/crystallites and strain in the film [134, 135]. Higher mosaicity indicate larger spread in deviations from the ideal orientation.

After film deposition, we start the film characterization with XRD to examine the crystallographic phases and orientations using x-ray diffraction [84]. We use a Bruker high-

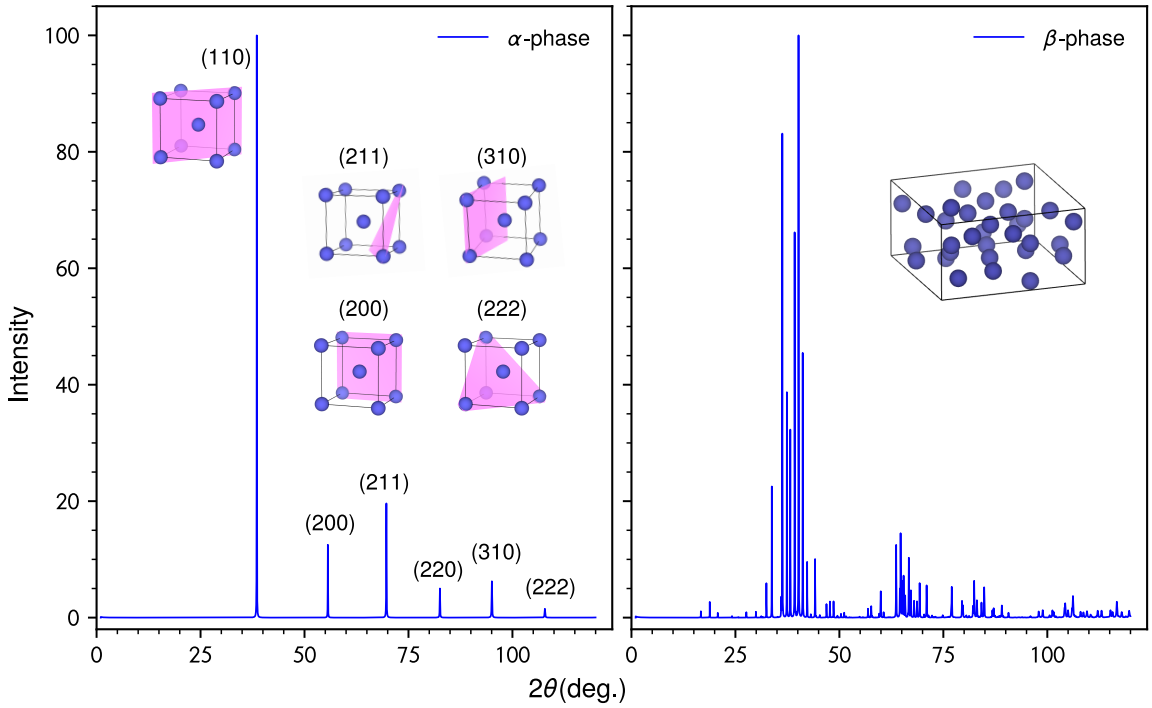

Figure 2.9: Powder x-ray diffraction (XRD) pattern of α (left) and β (right) phase Ta taken from ICSD code 652902 [89] for α-Ta and ICSD code 54208 [90] for β-Ta. Additionally, lattice planes inside a unit cell are shown for α-phase corresponding to the five different XRD peaks. Lattice planes are shown only for α-phase due to the simplicity of its unit cell.

resolution X-ray diffraction system in reflection, equipped with a (022) Ge monochromator for the characteristic K_α line of a Cu X-ray source.

The crystallographic analysis of the four different Ta films, namely S1, S2, S5 and S6, prior to lithography is presented in Fig. 2.10. It reveals the presence of both α- and β-phase in the film deposited at ENS, S1. Two peaks are present corresponding to α-phase at 38.3° and 82° with [110] film orientation as well as corresponding to β-phase at 33.7° and 70.8° with [002] film orientation. We attribute the growth of the β-phase to an initially low substrate temperature and high deposition rate during film growth.

In contrast, film S2 deposited at KIT, shows a single Ta peak at 107.8° corresponding to α-phase growing with [111] film orientation. XRD of films S3 and S4 is not shown here as it is similar to that of S2. Another film from KIT, S5 as well as the commercial film, S6 show two Ta peaks corresponding to α-phase growing with [110] film orientation. For S5, the peaks are positioned at 38.48° and 82.4° whereas for S6 at 38.44° and 82.36°. The peak positions are related to the out-of-plane spacing between crystalline planes. Shift in peak positions indicates change in the lattice parameters, which can arise from various sources including epitaxial strain from substrate mismatch, thermal expansion or contraction, or some residual stress introduced during film growth [136].

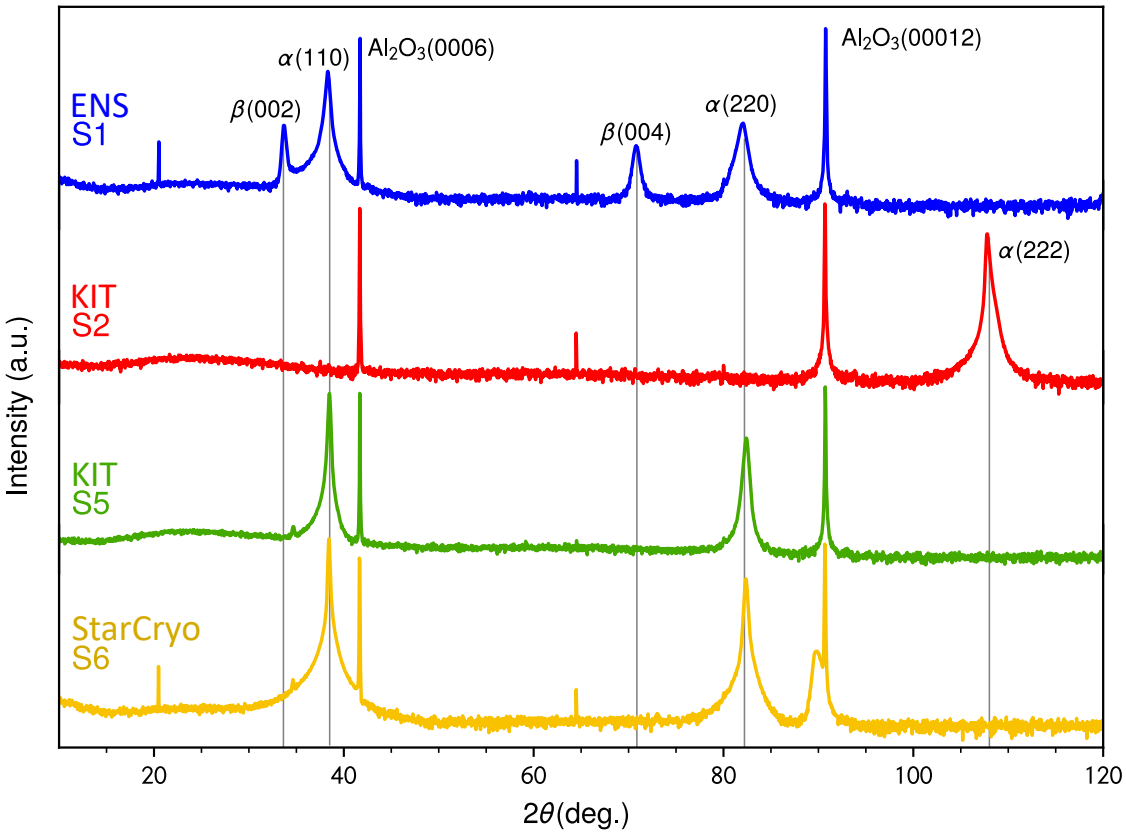

Figure 2.10: Crystallographic analysis of Ta films: X-ray diffractograms of four Ta films grown on c-plane Al_2O_3. Film deposited at ENS, S1, shows multiple Ta peaks corresponding to both α- and β-phase growing with (110) $\parallel z$ and (002) $\parallel z$ orientation, respectively. Film S2 shows a single Ta peak, denoted α(222), corresponding to the α-phase growing with (111) orientation $\parallel z$ direction; the α(111) peak is suppressed due to the symmetry of the BCC crystal structure (Systematic absence). Both S5 and S6 show two Ta peaks, denoted α(110) and α(220), corresponding to the α-phase growing with (110) orientation $\parallel z$ direction. The narrow peaks visible at 20° (S1 and S6) and 65° (S1, S2 and S6) correspond to the diffraction from residual K_β x-rays originating from the sapphire substrate. The broad sapphire peak at higher angles in S6 could be related to a worse quality of the sapphire used or from heating the substrate to very high temperatures before or during the film growth.

We also observe an additional peak at 34.64° in both S5 and S6 which might indicate the presence of a small fraction of β-phase or the diffraction from K_β x-rays originating from the sapphire substrate. All these films present a good example of the variation of deposition parameters leading to structurally completely different films. The mosaicity of diffraction peaks in these films was determined by recording the rocking curves for each Ta orientation and fitting them using a pseudo-Voigt function, which is a linear combination of Gaussian and Lorentzian functions. The rocking curved with the fit are shown in Fig. 2.11. We obtained highest film mosaicity of $\approx 2.4°$ for α as well as for β-phase in film S1, making it the film with lowest structural quality. S5 has intermediate mosaicity of 1°. At last, we obtained sub-degree mosaicity of 0.3° and 0.4°for films,

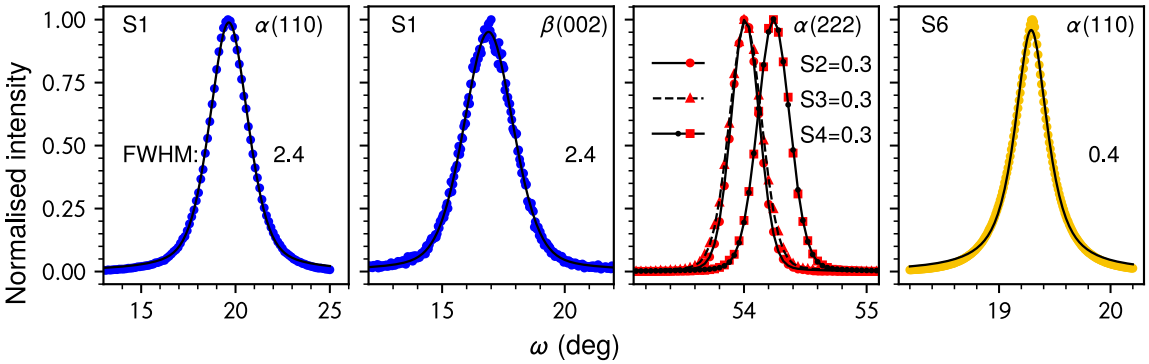

Figure 2.11: Rocking curves of various diffraction Ta peaks in different films and the corresponding FWHM. First two panels show $\alpha(110)$ and $\beta(002)$ peaks in S1. The third panel shows $\alpha(111)$ peaks for three films S2-S4 and the last panel shows $\alpha(110)$ in S6. The measured data is fitted using a pseudo-Voigt function (black line) to obtain the FWHM of the peaks.

S2-S4 and S6, respectively, making them the best films from crystal structure point of view.

XRD can be also used to estimate the volume fraction of β-phase in the film, S1 by comparing the fit to the experimental data with the theoretical data from the ICSD. More accurate results can be obtained by using ω scans instead of 2θ scans for this calculation because, as seen earlier, the thin film exhibits a fair amount of mosaicity of $\approx 2.4°$ leading to shifts in the peaks of 2θ scans. The measured data is fitted using the pseudo-Voigt function and the FWHM and area under the fitted peak is given in Table 2.3. The volume fraction is calculated using the ratio of the integrated intensities of α- and β-phase peaks of the XRD ω scans, I_α and I_β, respectively, according to Eq. (2.2). We look up the corresponding expected intensities, I_α^d and I_β^d, for powder diffraction in the ICSD selecting the following entries from it: ICSD code 652902 [89] for α-Ta and ICSD code 54208 [90] for β-Ta. Given the intensities listed in Table 2.3 and assuming the film is only composed of these two phases, the volume fraction is given by:

$$\frac{V_\beta}{V_\alpha + V_\beta} = \frac{I_\beta / I_\beta^d}{I_\alpha / I_\alpha^d + I_\beta / I_\beta^d} \tag{2.2}$$

The volume fraction for film S1 determined using Eq. (2.2) is 8.5%. Though it is in good agreement with the amount of β-phase visible in the ACOM data in Fig. 2.16(a), it is important to note that this estimation relies on the assumption of complete epitaxial growth of the phases and that all $\alpha(110)$ and $\beta(001)$ grains are oriented along surface normal ($Al_2O_3(0001)$). Given the relatively large mosaic spread in S1, this is not immediately evident. Nevertheless, confirming this assumption using XRD could be challenging because small quantities of differently oriented grains might not appear in the XRD.

Peak	$\alpha(110)$	$\beta(002)$
2θ	38.32°	33.68°
FWHM	2.4°	2.4°
Intensity (I)	44066.88	1067.14
Intensity (I^d)	100	26

Table 2.3: ICSD database intensities for the tantalum phases and the intensities measured for S1 tantalum film. 2θ is the angle corresponding to $\alpha(110)$ and $\beta(002)$ peaks. I is the peak height from the ω-scan. (I^d) is obtained from powder diffraction in the Inorganic Crystal Structure Database (ICSD) selecting the following entries from it: ICSD code 652902 [89] for α-phase and 54208 [90] for β-phase.

2.3 DC transport measurements

To investigate the electrical transport properties of Ta films, we conducted measurements of electrical resistance as a function of temperature. These measurements allowed us to determine the superconducting transition temperature (T_c) and residual resistance ratio (RRR). The later is defined as the ratio of resistance at room temperature to that just above T_c and it serves as an indicator of material defects and impurities and thus assesses film quality. A higher value is associated with low defects and higher film quality. As an example, RRR values of the order 10^3 have been reported in highly purified Ta specimens [137–139].

These measurements were performed using the standard four-probe technique in a Physical Property Measurement System (PPMS) by Quantum Design. We compared the sheet resistances $R_\square$ for six different films, S1-S6. Specifically, unpatterned films were used in S1, S2, S5, and S6 before undergoing lithography, whereas for S3 and S4, we employed patterned Hall bar structures as depicted in Fig. 2.12. To determine the resistivity ρ of these unpatterned films, we followed the approach outlined by [140]:

$$\rho = \frac{\pi t}{\ln 2} \times R, \quad R_\square = \frac{\rho}{t} \tag{2.3}$$

where t is the film thickness, R is the measured resistance. The film thickness was determined by techniques such as AFM and TEM. Figure 2.13 shows the sheet resistance plotted against temperature and the results are summarized in Table 2.4.

All films have T_c close to the bulk value of 4.4 K. Moreover, the $\alpha(111)$ films S2-S4, which were deposited at a higher substrate temperature, exhibit a slightly improved T_c of 4.3 K compared to the other films. Film S1 has the highest room temperature $R_\square$, which is attributed to the presence of lower T_c β-phase. In contrast, there is a significant variation in the RRR values. Film S1 shows a minimum RRR of 4, associated with the β-phase, followed by films S5 and S6. This indicates that presence of β-phase is not

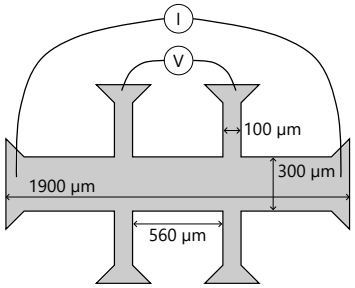

Figure 2.12: Hall-bar used for 4-probe transport measurements. Design adapted from [141].

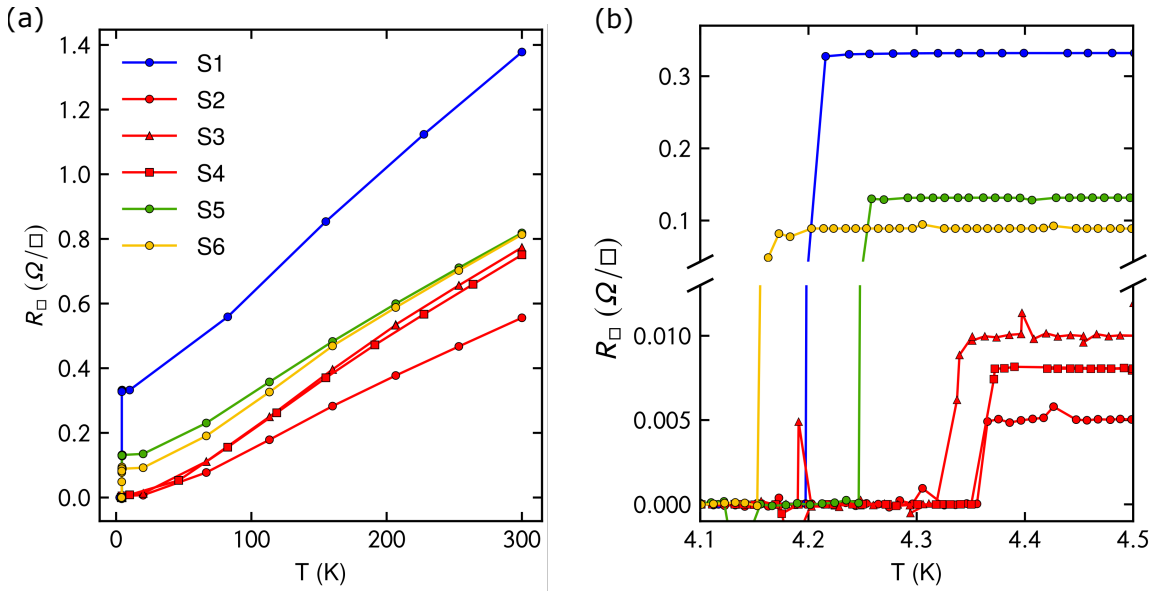

Figure 2.13: Sheet resistance $R_\square$ as a function of temperature T for six different Ta films S1-S6. (a) shows the full temperature range and (b) shows the zoom-in near T_c. The measurements were performed with 10 µA excitation current.

the contributor to the low RRR. In contrast, film S2 has the highest RRR of 95, which can be attributed to its higher deposition temperature. Same goes for the other α(111) films S3 and S4, which have similarly high RRR as S1. Moreover, a direct correlation is observed between RRR and film mosaicity (Fig. 2.11). The films with high RRR have the lowest mosaicity.

2.4 Surface topography

We utilize Atomic force microscopy (AFM) to study the surface morphology of Ta films. AFM is a mechanical surface imaging technique based on monitoring interactive forces between a probe and sample surface [142, 143]. Unlike scanning tunneling microscopy, which relies on tunneling current flow, AFM detects the bending of a flexible cantilever

Sample	T_c (K)	RRR	Sample state
S1	4.2	4	Diced chip, before patterning
S2	4.3	95	Diced chip, before patterning
S3	4.3	77	Patterned, Hall bar
S4	4.3	93	Patterned, Hall bar
S5	4.2	6.2	Diced chip, before patterning
S6	4.1	9.2	Diced chip, before patterning

Table 2.4: DC transport measurements using four probe method: Superconducting transition temperature (T_c), residual resistance ratio (RRR) of Ta films and description of the samples used.

caused by tip-surface interactions. The technique generates three-dimensional surface maps by scanning a sharp tip across the sample surface. AFM can operate in various modes depending on the force regime and tip-surface distance employed. We use a Bruker Dimension Ikon instrument and operate in *tapping* mode at ambient conditions.

The surface morphology of Ta films is influenced by their phase composition [144]. AFM scans of $1 \times 1\mu m^2$ area for films S1-S6 are shown in Fig. 2.14. The surface morphology α-Ta with (110) orientation distinctly differs from those with (111) orientation. Surface of film S1 shows a fiber-like structure throughout the scanned area, a pattern also typical for other BCC refractory metals such as molybdenum or tungsten [145]. Similar features are also observed in films S5 and S6. The feature size in S1 and S5 is comparable; however, in the commercially deposited film S6, the features are considerably larger and aligned uniformly. Further examination of a larger $5 \times 5\mu m^2$ area of the same film shows larger domains spanning several micrometers, with a defined orientation within each domain. The surface of $\alpha(111)$ Ta films is smoother than that of $\alpha(110)$ films and no preferred texture in surface morphology is seen.

2.5 STEM and ACOM

The scanning transmission electron microscope is one of the most powerful material characterization tools providing spatial resolution of sub-angstrom [146]. The basic working principle of STEM is as follows: an electron source generates a highly coherent electron beam which is then accelerated to high voltages of upto 300 kV [147]. Electromagnetic lenses are used to focus the high energy electron beam to the desired diameter before it passes through a thin specimen. The interaction between the focused electron beam and the specimen results in various types of electron emissions such as transmitted electrons, back-scattered electrons, secondary electrons, characteristic, and continuum

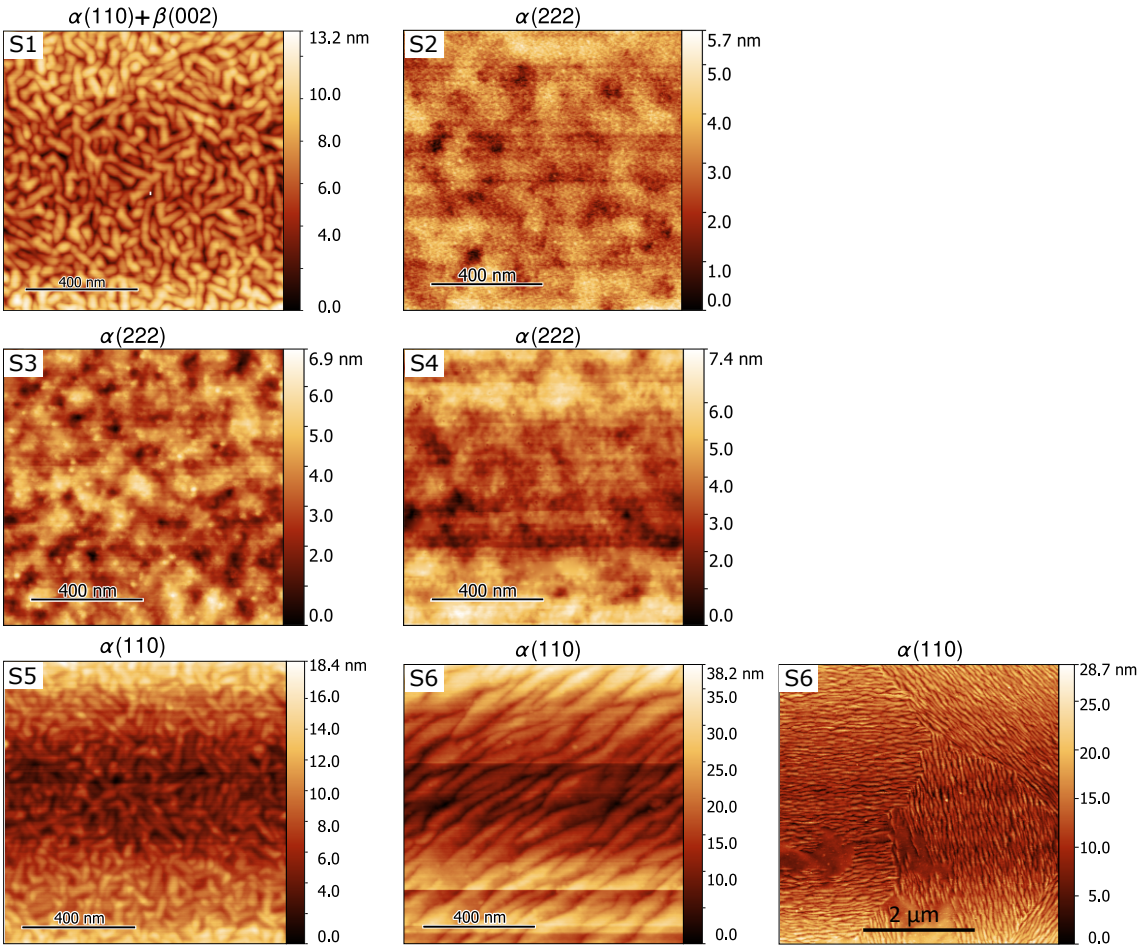

Figure 2.14: AFM surface topography of $1 \times 1\mu m^2$ area. Additionally, a larger scan area of $5 \times 5\mu m^2$ is shown for film S6.

x-rays, Auger electrons, etc. Among these, STEM utilizes transmitted electrons through the specimen which are detected to form an image. STEM can be used to obtain atomic resolution images of films to reveal their crystalline structure, presence and location of defects, quality of grain boundaries and to determine thickness of various interfaces.

Automated crystal orientation mapping (ACOM) is a STEM based technique developed to automatically determine the orientation of individual crystallites with high spatial and angular precision [3, 148]. The orientation map is obtained by scanning an electron beam across a sample, where interactions between the beam and the crystal lattice produce diffraction patterns. These patterns encode crucial information about the crystal structure, including orientation, symmetry, and lattice parameters. A high-resolution detector is used to capture these diffraction patterns, which are then matched against a library of calculated diffraction patterns. The result is an orientation map in which a color is assigned to different regions of the scanned area based on their measured crystallographic orientations, with the color scheme interpreted through accompanying

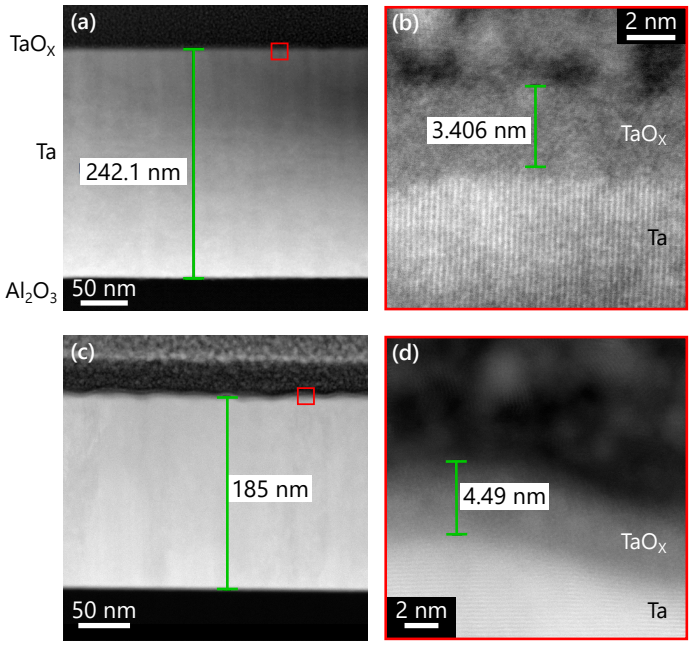

Figure 2.15: Cross section TEM[2] image of (a) film S2 and (c) film S1. (b) and (d) show the enlarged view of the tantalum surface showing the oxide thickness.

pole figures [149], similar to one shown in Fig. 2.16(c). This technique enables the generation of both phase and orientation mapping across micrometer-scale areas with nanometer-level spatial resolution.

The STEM characterization was carried out on a Thermo Fischer Scientific Titan Themis 300 (S)TEM equipped with a Nanomegas ASTAR system and a Dectris Quadro camera. All experiments were performed at 300 kV acceleration voltage in nanoprobe mode with 30 mrad convergence for high angle annular dark field (HAADF) imaging and in microprobe precession mode at 1 mrad convergence and 0.6° precession angle for ACOM. Electron transparent cross sections of the thin films were prepared on a FEI Strata 400 S dual beam SEM/FIB. Protective layers of electron and ion beam deposited platinum were applied successively before trench cutting to preserve the original oxide layer structure. The initial XRD analysis presented in Section 2.2 revealed the presence of both α- and β-phases in the examined films. Notably, film S1 stands out due to the inclusion of the β-phase in it, which makes it particularly interesting for studying phase distribution. It is crucial to further investigate S1 to understand the thickness of the surface oxide layer, surface roughness, any defects close to the sapphire interface or with the film bulk, and various film interfaces. The coexistence of phases with distinct crystalline properties can lead to multiple grain boundaries and strained interfaces due to lattice mismatches. These sites can negatively impact the performance of microwave resonators by contributing to losses. Therefore, STEM and ACOM are ideal techniques

[2] All measurement data shown in Section 2.5 was recorded by Lucas M. Brauch at KIT.

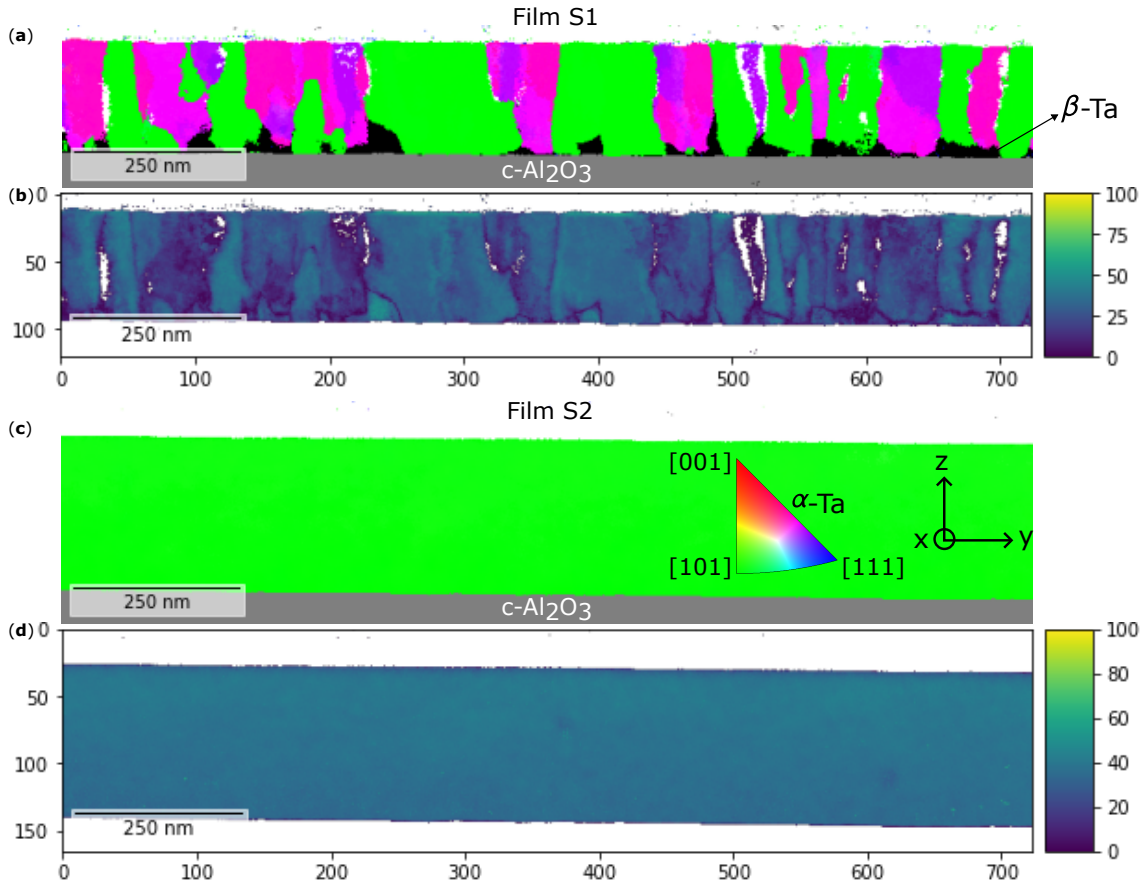

Figure 2.16: Automated Crystal Orientation Mapping (ACOM) of lamella extracted from films S1 ((a) and (b)) and S2 ((c) and (d)) performed using a transmission electron microscope. (a) The black areas correspond to the β-phase, while the other colors (except white) indicate the crystal orientation of the α-phase in the x-direction. The color key for the α-phase orientation is shown in panel (c) and is applicable to both (a) and (c). The gray regions beneath the films indicate the sapphire substrate. White color areas in film S1 indicate regions where the crystal orientation is not well defined. (b) and (d) are orientation reliability map of (a) and (c), respectively.

for this investigation. For comparison, we also examine film S2, which consists entirely of α-phase and exhibits the highest residual resistance ratio, indicating high film quality. and overall the best film so far from material properties point of view. Also, film S2 has exhibited overall superior material characteristics so far compared to other films.

Figure 2.15 shows the cross section view of film S1 and S2. The two films have different thickness: S2 has higher thickness of approximately 242 nm than S1 which has 185 nm. An enlarged view of the surface oxide is shown in Fig. 2.15(b),(d) and an overall thicker surface oxide of approximately 4.5 nm is present in film S1 as compared to 3.4 nm in S2. In addition, the film surface is smoother in S2 as compared to S1.

The orientation map of cross-section of film S1 is shown in Fig. 2.16(a). It shows ACOM of a film lamella, where both α- and β-phase are present. The α-phase is shown as

colored areas except black and gray. In addition, there are two main orientations of α-phase visible as green and pink areas leading to several grain boundaries. β-phase is shown as black areas without an indication for its orientation and is only present near the sapphire-Ta interface and not at the film surface. The β-phase may preferentially localize at the sapphire-Ta interface because of its reduced interfacial energy with the substrate. Figure 2.16(b) shows the confidence map of the orientation map shown in Fig. 2.16(a). As can be seen, the grain boundaries have higher uncertainty than within a grain or a crystallite.

Figure 2.16(c) shows an ACOM of a S2 film lamella composed of a single crystal grain. Keeping in mind that ACOM is a highly localized probe, it still suggests that the grain size in the film is at least on the order of a micrometer. It is important to note that phase determination for films S1 and S2 from ACOM is in good agreement with XRD, which examines a much larger area of the order of several 1000 µm.

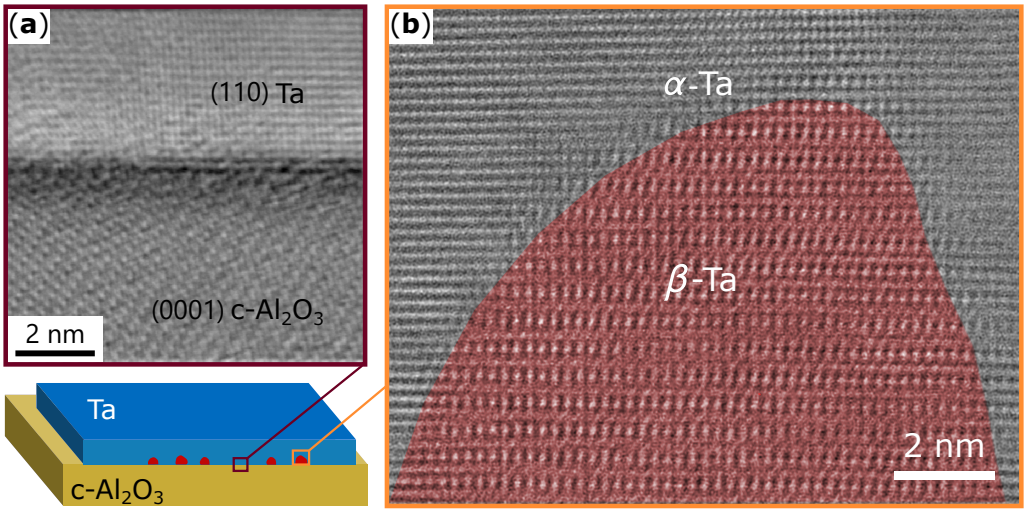

Figure 2.17: Scanning transmission electron microscopy (STEM) images of α-β interface in the film S1. The schematic of the film cross-section evokes the film structure from the Automated Crystal Orientation Mapping data in Fig. 2.16(a) with scattered islands of β-phase close to Ta-sapphire interface. (a) interface between Ta and sapphire (b) High angle annular dark field (HAADF) STEM image of a β-phase grain highlighted in red for better visibility. Its interface with the α-phase (gray) is epitaxial.

Fig. 2.17 gives a deeper insight into the atomic-scale microstructure of the β-phase containing film S1. The interface between Ta and sapphire substrate is shown in Fig. 2.17(a). The β-phase forms a coherent interface with the α-phase and furthermore confirms that the observed crystal structure of β-phase corresponds to literature. As shown earlier, the crystal unit cell of β-phase Ta is more complex than a primitive tetragonal unit cell [112]. From this, an overall more complex microstructure with increased amounts of high-angle grain boundaries potentially associated with a local suppression of superconductivity,

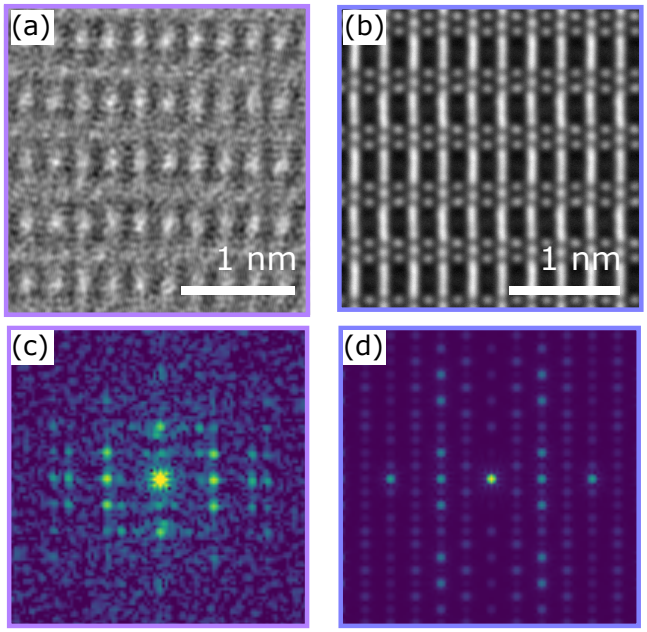

Figure 2.18: Scanning transmission electron microscopy (STEM) image of β-phase in film S1. (a) and (b) compare the β-phase HAADF STEM image with a simulated image at the same scale. (c) and (d) show fast Fourier transform (FFT) of the images shown in (a) and (b), respectively and the width of both FFT images is 20.1 nm^{-1}.

could be expected. However, the β-phase forms a highly coherent interface with the α-phase [Fig. 2.17(b)].

It is important to remember that the large tetragonal unit cell of β-phase, shown in Fig. 2.9, makes it difficult for the ACOM matching algorithm to recognize the β-phase. That's why, to confirm its presence, we simulate the high angle annular dark field (HAADF) STEM image in Fig. 2.18(a). The crystallography data for the image is retrieved from the Materials Project for Ta (mp-42) from database version v2023.11.1. [90, 150]. We then compare it with the measured HAADF image in Fig. 2.17(b). We observe a fair agreement between the experimental and the simulated structure in terms of observed lattice spacings. However, their fast Fourier transforms [Fig. 2.18(c,d)] indicate differences in symmetry, which suggests small deviations from the theoretical crystal structure of the β-phase. Nevertheless, the images substantiate the claim that the dark areas in the ACOM data of film S1 in Fig. 2.16(a) are closely related to the β-phase.

2.6 Superconducting properties of Ta

The superconducting properties of thin films deposited on substrates differ markedly from the behavior exhibited by the same materials in bulk form [151, 152]. Pure bulk Ta in known to be a type-I superconductor with a critical-magnetic field H_c of 83 m T[153].

However, in thin film form, Ta films are type-II superconductor [154]. In this section, investigation of superconducting parameters such as superconducting gap Δ, T_c and H_c using superconducting quantum interference devices (SQUIDs) and STM techniques is presented.

2.6.1 SQUID magnetometry

SQUID magnetometers are the most sensitive available technology for measuring magnetization, and are therefore well suited for characterizing the diamagnetic response of superconducting thin films as a function of temperature and external field. Their operation is based on two fundamental quantum phenomena: magnetic flux quantization i.e. if a loop of superconducting material is cooled below T_c in presence of a magnetic field, the magnetic flux in the loop is trapped and can only take values equal to the multiples of flux quantum ($\phi_0 = h/2e$) and Josephson tunneling effect [155].

SQUIDs consist of a superconducting loop containing two Josephson tunnel junctions. For practical measurements, the magnetic signal to be measured is coupled to the SQUID loop through two coils: a detection coil and an input coil. The sample is placed inside the detection coil and is moved as shown in Fig. 2.19. The sample motion generates changing magnetic flux that is inductively transferred to the input coil. This flux change is then detected by the SQUID loop, causing periodic voltage changes across the SQUID. The measurements were performed using a MPMS XL SQUID magnetometer from Quantum Design and were conducted by Dr. Sudip Pal at university of Stuttgart.

The magnetization of the sample is measured as a function of temperature in the presence of a magnetic field. The results in Fig. 2.20(a) show the parallel orientation measurements of H_c as a function of temperature for films S1, S2, S5, and S6. To obtain the H_c, we use the relation between the critical magnetic field and temperature is given by [44]:

$$H_c(T) = H_c(0)\left[1 - \left(\frac{T}{T_c}\right)^2\right] \tag{2.4}$$

where $H_c(0)$ is the critical field at zero temperature.

The small grain size of the S1 film leads to shorter superconducting coherence length and in turn a higher H_c [71]. This constitutes an additional benefit, when considering applications in magnetic fields such as hybrid spin quantum systems. The data in Fig. 2.20(a) is fitted to Eq. (2.4) to determine the zero-temperature critical fields $H_c(0)$. As expected, $H_c(0)$ for S1 is highest at (388 ± 17) mT and it is smallest for S2 at (107 ± 4) mT. Films S5 and S6 have similar $H_c(0)$ of 292 mT and 215 mT, respectively. The S2 $H_c(0)$ is close to the value for bulk Ta [71]. These measurement also provide independent confirmation of the critical temperature values previously determined through DC electrical transport in Section 2.3.

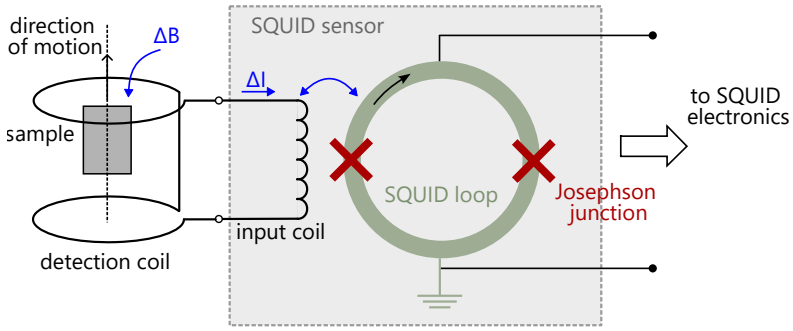

Figure 2.19: Schematic diagram of a typical SQUID device.

2.6.2 Scanning tunneling microscopy

STM is a surface characterization technique that generates topographic images with sub-nanometer resolution [156]. The underlying principle of STM is quantum tunneling: an atomically sharp conducting probe tip is positioned above a conductive sample surface with a gap of approximately 10 Å, creating a metal-vacuum-metal tunnel junction. When a bias voltage is applied between the tip and sample, electrons tunnel across the gap, generating a measurable current. As the tip scans across the surface, the tunneling current is continuously recorded to create an image. This image captures both surface topography and electronic structure, including work function variations and local density of states.

STM measurements were performed using a home-built dilution refrigerator setup at a base temperature of 45 mK [157]. The superconducting gap and critical magnetic field of the films were characterized by dI/dV measurements conducted in out-of-plane magnetic fields. Prior to measurements, removal of the surface oxide with argon milling [158]. These measurements were carried out with a bias voltage of $V_b = 1.5\,\mathrm{mV}$ and a current setpoint of $I_p = 100\,\mathrm{pA}$, utilizing a standard lock-in technique with an AC modulation voltage of $V_{\mathrm{mod}} = 20\,\mu\mathrm{V}$. STM was conducted by Dr. Soroush Arabi at KIT.

Based on the results from SQUID measurements, films with highest and lowest critical fields, i.e. S1 and S2, were selected for additional characterization using STM. Local measurements of the superconducting gap Δ as a function of perpendicular magnetic field H were performed at 45 mK after removal of the surface oxide with argon milling [158]. The two quantities are related by

$$\frac{\Delta}{\Delta_0} = 1 - \left(\frac{H}{H_c}\right)^2 \tag{2.5}$$

The results are shown in Fig. 2.20(b). These measurements yield Δ_0 of $(585 \pm 16)\,\mu\mathrm{eV}$ and $(600 \pm 28)\,\mu\mathrm{eV}$ for films S1 and S2, respectively, which are only slightly smaller than the value for bulk Ta of 686 µeV [159]. Critical magnetic fields of $(103 \pm 5)\,\mathrm{mT}$

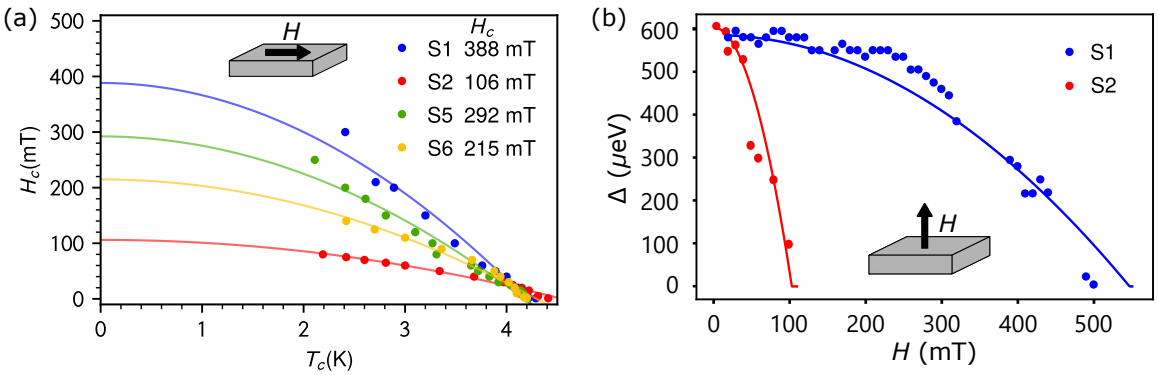

Figure 2.20: (a) Critical magnetic field in parallel orientation (H_c) as a function of temperature (T) for Ta films. The H_c's were measured using a SQUID magnetometer. The solid lines correspond to a fit of the data to Eq. (2.4). (b) Superconducting gap (Δ) as a function of magnetic field for S1 and S2 Ta films. The solid lines correspond to a fit of the data to Eq. (2.5).

and (540 ± 34) mT were required to suppress superconductivity, which is in good correspondence with the magnetometry data.

2.7 Time-of-Flight Secondary Ion Mass Spectrometry

ToF-SIMS is a high-resolution mass spectrometer technique aimed for surface analysis providing elemental and molecular information [160]. It is a semi-quantitative and highly sensitive technique used to perform surface spectrometry, chemical mapping by surface imaging, depth profiling and volume analysis [161]. A focused primary ion beam is used to bombard the surface of the material under investigation resulting in emission of neutral atoms or molecules, ions or radical ions from the surface [136]. Moreover, the emitted ions, known as secondary ions can have positive or negative polarity depending on the chemical environment of the surface [162]. The secondary ions are detected and separated by an ion detector based on their mass to charge ratio. The intensity of these secondary ions can be described by the basic SIMS equation:

$$I_S^x = I_p C_x S \gamma F \tag{2.6}$$

where I_S^x is the secondary ion current of species x (i.e. the measured secondary ion counts of x), I_p is the primary ion beam current, C_x is the concentration of species x, S is the sputter ion yield of x and γ is the ionization efficiency, i.e. the probability of the detected species forming positive or negative ions. Finally, F is the transmission of the analysis system. For typical depth profile measurements, the intensity of specific ions is measured as a function of the depth of the sample being analyzed.

We employ ToF-SIMS to analyze impurity levels in various Ta films, with aim to establish a relationship between detected impurities and the performance of resonators [103, 163]. Typically, the impurities in Ta films are influenced by the purity of the sputtering target and gas, as well as a range of physical and chemical treatments, including procedures during fabrication and wafer dicing. Depth profiling was performed for samples S1, S2, S5, and S6. Ta-coated sapphire wafers, originating from the same wafers as used for fabricating the resonators, were eroded by sputtering with cesium or oxygen ion sources under high vacuum. The spectroscopy was performed by Alexander Welle on a ToF.SIMS5-100 instrument (ION-TOF GmbH) at KMNFi, KIT.

The analysis is discussed in two parts: firstly, SIMS depth profiling with O^+ bombardment and secondly, with Cs^+ bombardment. Left column of Fig. 2.21 shows the depth profile obtained with O^+ bombardment of the four films where various positive secondary ion intensities are plotted against the sputter ion fluence [ions/cm^2] as an arbitrary measure of depth. In addition to elemental composition, the spectra also contain information about the relative thickness of the films. The film thickness decreases in the order: S2 $\approx$ S5 (deposited at KIT) $>$ S1 (ENS, Paris) $>$ S6 (Star Cryoelectronics). Contaminants such as TaN, Nb^+, Na^+, K^+ and Ca^+ are present in all films. TaN is a common byproduct of magnetron sputtering and is present in all films. However, the total TaN content is similar in all samples when normalized with respect to the Ta signal. Most importantly, magnetic materials such as iron and nickel are not found in any of the films. There is an increase in the Nb^+ signal at the bottom of the Ta film in S5, while the commercial sample S6 exhibits a nearly negligible amount of Nb. Alkaline metal ions Na^+, K^+ and Ca^+ are found both at the film surface and the bottom of the films and are a common result of water used in wafer polishing and dicing. Comparing this to the resonator quality factors shown in Chapter 4, we note that the commercially deposited Ta film S6 has the least amount of impurities overall but it does not perform best in microwave measurements.

To analyze films for non-metallic contaminations and the amount of oxides, we performed SIMS depth profiling with Cs^+ bombardment analyzing negative polarity secondary ions. The results are shown in right panel of Fig. 2.21. Three sample depth regimes will be regarded separately to understand how the concentration of contaminants and oxides changes with film depth.

(a) **Outermost surface as received**
Depth profiles show several layers on the surface of S2, a very thin layer of airborne carbon containing contamination, followed by a tantalum oxide layer showing various $Ta_xO_y^-$ species together with the ^{16}O signal (partly saturated) and the ^{18}O signal. No Ta dimers indicating that no metallic Ta is present. Underneath the oxide layer, a thin TaH layer is detected followed by the metallic tantalum bulk showing Ta_2^- signals and weaker signals of Ta^- and larger Ta_x cluster ions (not

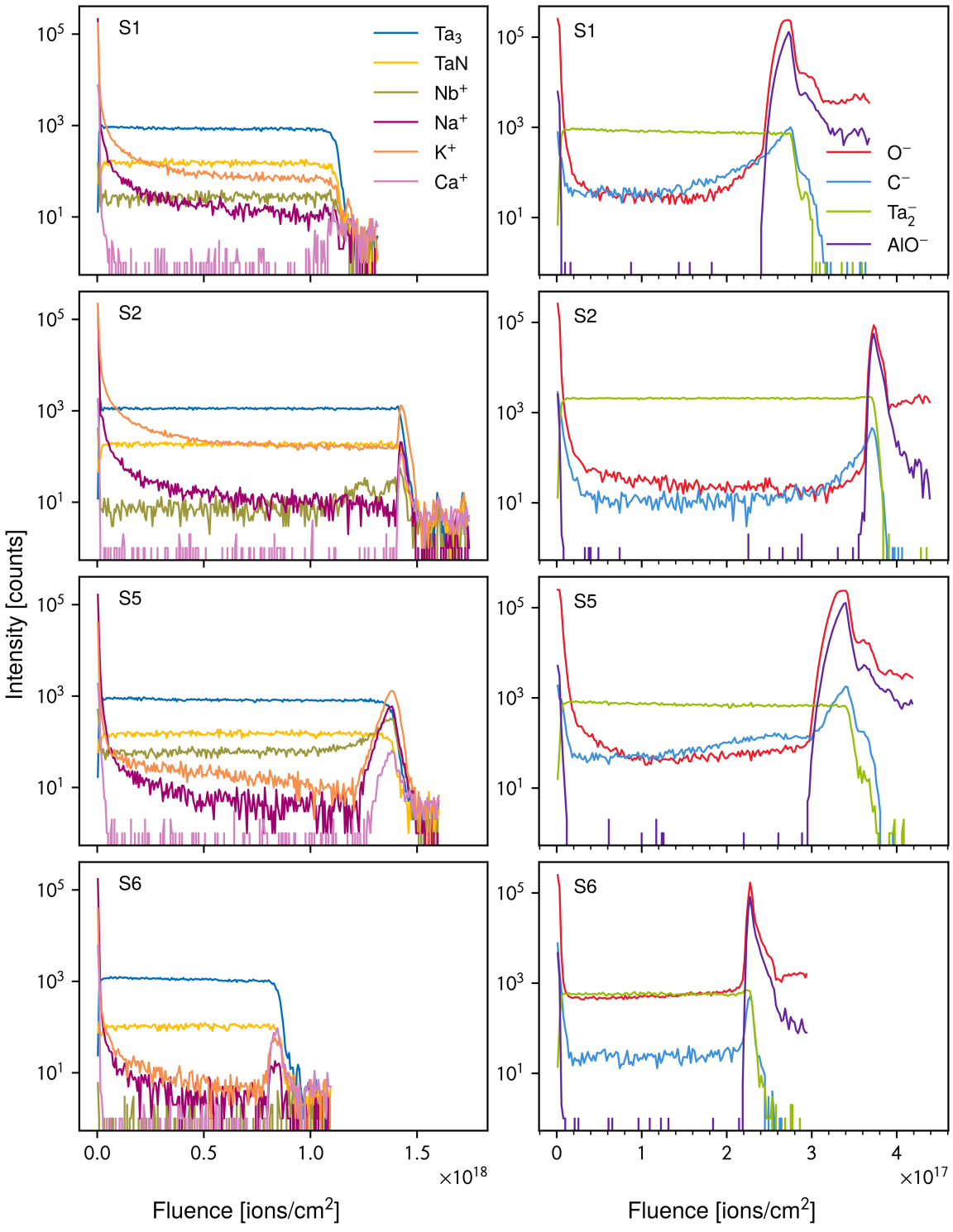

Figure 2.21: Time-of-Flight Secondary Ion Mass Spectrometry depth profile of S1, S2, S5 and S6 Ta wafers (only diced, no lithography steps performed). Intensity of sputtered secondary ions is plotted against the fluence which is defined as number of impinged sputter ions per cm^2 area. Zero fluence is associated with the film's surface and at the high-fluence end of the spectra is the metal-substrate interface. Left(right) column shows depth profiling using Cs^+(O^-).

shown). This behavior is also found on S1 with a slightly more pronounced oxide layer.

(b) **Tantalum bulk**
Here S2 has a lower oxygen contribution the O^- signal normalized on the dominating Ta_2^- signal ranges at 1.3×10^{-2} relative intensity, whereas in case of S1 this signal ratio is higher, 4.6×10^{-2}.

(c) **Tantalum / sapphire interface**
Due to the roughness of the tantalum layer this interface is less defined; note the apparent overlap of Ta_2^- signals indicating bulk tantalum and AlO^- from the underlying sapphire. Despite the lower overall tantalum thickness, this effect is more pronounced on S1. Also, the carbon and chlorine contamination at this interface is more pronounced at S1 as compared to S2. Whether this is due to different cleaning procedures of the substrates or an effect of the tantalum deposition is not clear. The elevated contamination levels are laterally uniform reaching far into the tantalum layer. TaH is less prominent at this depth. Entering the insulating sapphire substrate, the total secondary ion count rate is dropping due to charging effects.

3 Experimental methods and Ta post-processing

After examining the material properties such as film structure, transport, etc. of Ta films in Chapter 2, the next step involves utilizing lithography techniques to fabricate microwave resonators. This chapter gives a description of resonator fabrication procedure. Section 3.1.1 discusses the standard procedures for sample preparation and lithographic steps involved in fabricating the resonators as they can be just as crucial as the material's composition itself. At the start of this PhD, the initial fabrication methodologies for Ta were based on the work of Place *et al.* [1] and customized to meet our specific requirements. The exact fabrication procedure is described in Section 3.1.2. Following this, in Section 3.2, various resonator designs and their design parameters are presented. Next, the setup used for the measurements of the resonators at low temperatures is explained (Sections 3.3 and 3.4). Additionally, Section 3.5 covers the details of the essential post-processing step of buffered oxide etch (BOE).

3.1 Resonator fabrication

3.1.1 General fabrication steps

After sputtering Ta on sapphire substrates, which was discussed in detail in the previous chapter, the films are brought to a clean room facility of Class 6 and 7 to start the resonator fabrication process. A schematic for the lithography recipe used is shown in Fig. 3.1 showing the difference between positive and negative resist process, here used with UV and electron-beam exposure, respectively. The following sections provide a description of the fabrication steps mentioned in there.

Solvent Cleaning

The first step in fabrication is the cleaning of Ta films. This is to remove any contaminants such as dust particles that may deposit on the film during its transfer from the deposition chamber to the cleanroom. It ensures similar starting condition for all films. A common

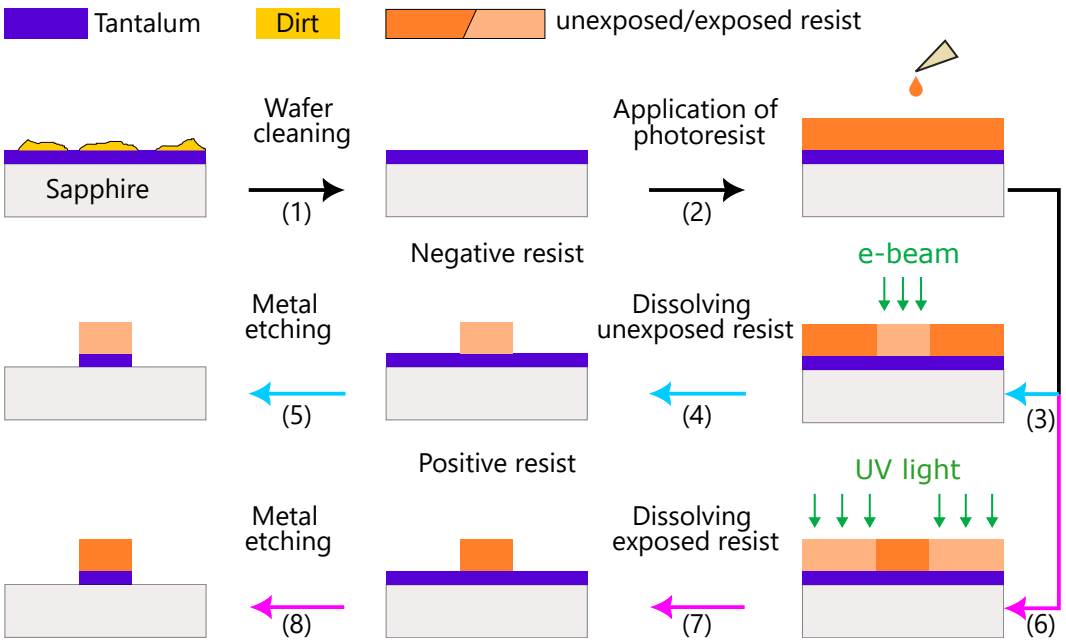

Figure 3.1: Schematic diagram showing step by step lithography process for resonator fabrication. The steps for negative and positive photo-resist are shown separately. They are as follows: (1) wafer cleaning (2) resist coating (3,6) resist exposure (4,7) developing and (5,8) Ta etching. These steps are described in detail in Section 3.1.1

practice to clean the film surface with Piranha solution before spinning resist to remove carbon contamination [1, 164] Initially, films were prepared for spinning resist by dipping them in Piranha solution followed by rinse in deionized (DI) water. A mixture of sulfuric acid (H_2SO_4) and hydrogen peroxide (H_2O_2) in ratio 3:1 was used. However, this did not show any positive affect on the final resonator outcomes and it is also shown to increase the Ta surface oxide [2]. Finally, films were cleaned using only combination of commonly used solvents such as acetone, ethanol and isopropanol (IPA). First, the wafer is immersed in acetone at room temperature. It is optional to heat the acetone to 50 °C on a hotplate to improve the effectiveness of cleaning. This is followed by immersion in Ethanol at room temperature and rinsed in IPA in an ultrasonic bath at room temperature. As there are no delicate structures on the wafer at this point, highest power of sonication can be used. Afterwards, the films are blown dry using a nitrogen gun to get rid of the solvent liquid and were baked at 120 °C to get rid of any trapped moisture on the film surface followed by a 2-3 min of cooling down immediately before resist coating. This is to ensure good adhesion of the resist which is the next step. This step was the same for all the chips fabricated.

Resist coating

In the second step, a uniform layer of resist is coated on Ta. The films are mounted on a spincoater to coat the cleaned wafers with resist. It should be ensured that no dirt particles are present on the wafer which may result in an uneven thickness of the resist layer in the region of interest. The resist coated film is baked on a hotplate to evaporate the excess solvents in the resist and to harden the resist. This step is known as prebake. Initially, we used a negative e-beam resist from the maN 2400 series, specifically the thinner version maN 2403 was used. However, in the later step of metal removal by wet etching, to ensure that the resist layer can withstand the etching which is described in further sections, the thickest version maN 2410 was used.

Resist Exposure

The resist coated wafer is exposed using the electron beam or UV light to chemically alter the resist to form a circuit pattern. For e-beam resist, the wafers were exposed in a Leo 1530, Raith ElphyPlus system at 30 keV. The system was situated outside the cleanroom. One consequence of the e-beam exposure on insulating substrates is charge accumulation. To overcome this, the common practice is to sputter deposit a conducting layer of gold before exposure which is later easily removed by dipping in Lugol solution. However, it was not possible to develop the maN resist after dissolving the gold layer in Lugol solution. Therefore, the gold anti-charging layer was not an option and instead the already present Ta film was employed for this purpose. This was achieved by a scratch that was made on the top right corner of the wafer with the help of tweezers to get rid of the resist layer. This exposes the conducting Ta film beneath. The wafer is then mounted inside the chamber such that the holding clip is touching the exposed Ta to make a channel for discharging.

Another concern in the e-beam process was the use of negative resist. By definition, the irradiated region stays after developing. This also means, that some of the e-beam can penetrate into the metal and interact with it in the regions that are going to be part of the actual circuit, which may result in higher defect densities in the Ta film and sapphire substrate. To overcome this, an obvious solution is to use a positive resist instead. However, the combination of positive resist with e-beam lithography is not very efficient as it would mean exposing large areas. This was deemed to be too time and resource consuming. For reference, exposure of one resonator in Fig. 3.4 with takes approximately 1 h whereas, the exposure time for the whole wafer in optical lithography is of the order of few seconds. Therefore, e-beam lithography was completely eliminated and optical lithography was opted for instead. For optical lithography, wafers were exposed with a Süss 365 nm ultra-violet mask aligner. The photomask was fabricated in house using a Heidelberg direct writer tool by Lucas Radke.

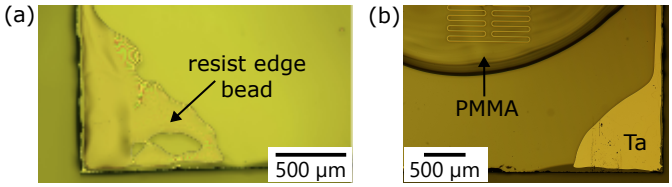

Figure 3.2: (a) optical image of an edge of a chip with the resist edge bead. (b) A resonator covered with PMMA resist that serves as a protective layer during the etching of edge bead.

Resist developing

For negative (positive) resist, the unexposed (exposed) resist is dissolved in a developer. A mixture consisting of a TMAH based AZ developer, metal ion containing, and DI water in 1:1 ratio was used for maN 2403 e-beam resist. The developing time varied by few seconds in order to dissolve the resist edge bead which is a common issue when resist is spun on non-circular wafers. The edge bead is a buildup of resist at the edges of the wafer during spin coating. Figure 3.2(a) shows an edge bead visible after developing on one of the wafers. For maN 2410 e-beam resist, the new metal ion free developer was used. After developing, the resist mask was baked in an oven to strengthen the resist, this step is known as postbake.

Metal etching and resist cleaning

In the final step, the parts of the metal film not protected by resist are removed leaving behind the patterned resonator under the resist mask using a wet etching technique with maN 2403 resist. Initially, following the recipe from [1], where wet etching resulted in better outcomes than dry etching, we also opted for wet etching with a solution of hydrofluoric acid, nitric acid, and water in equal parts ($HF:HNO_3:H_2$=1:1:1). However, in our case, this method had several drawbacks: it etched Ta quickly, making it difficult to control the etching time. Sometimes also etching away the Ta protected by the resist mask, which was not desirable. Furthermore, the wet-etch solution is highly corrosive and poisonous requiring special handling.

Therefore, the wet etching was replaced by a dry etching technique called reactive ion etching (RIE). In this technique a low pressure plasma is used to chemically remove material from a surface in a controlled manner, enabling the creation of desired structures. The RIE process requires precise control over parameters like plasma density, energy, and gas composition to achieve the desired etch depth and profile. SF_6 (sulfur hexafluoride) was used to etch Ta with initial etch time of 150 s. It turned out to be a longer time than actually needed and resulted in over-etching as shown in Fig. 3.3. High etch times can etch the substrate affecting the quality of its surface. The etch rates are also affected by 'loading effect', a phenomenon where etching rates are non-uniform due to variations in

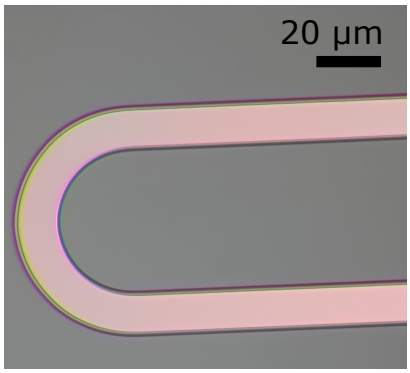

Figure 3.3: Optical image of the resonator meander after Ta etching showing undercut.

substrate material or device structures [165], which caused initial difficulties in applying etch times optimized for small samples to larger ones.

To achieve cleaner results and further improve the final etching, a oxygen descum step, also performed in the RIE, was added right before the fluorine etching. In the oxygen descum step, an oxygen plasma is used to chemically remove any resist residues or thin invisible resist layers remaining after developing.

3.1.2 Finalized fabrication parameters

To develop a fabrication process for Ta, we started with the standard electron beam (e-beam) lithography. The individual lithography steps were modified and refined over time to yield reproducible resonators. However, e-beam lithography is resource intensive and time consuming. This was the motivation behind transitioning towards an optical lithography process which was facilitated by the existing working recipe for e-beam lithography. As a result, resonators were fabricated using both lithographic techniques, sharing some common steps.

For e-beam lithography, 2" Ta coated films were coated with protective resist and diced into 7×7 mm^2 size pieces. After cleaning the protective resist layer following steps in Table 3.1, negative e-beam resist maN 2410 (Micro Resist Technology GmbH) was spun at 3000 rpm for 60 s and prebaked on a hotplate set at 90 °C for 90 s. No gold was deposited as a conductive layer. Resist coated wafers were exposed under e-beam with a dose of 350 µC cm^{-2} using a Leo 1530, Raith ElphyPlus system. Exposed resist was developed in a TMAH based developer (Micro Resist Technology maD 525) for 3 min followed by dipping the wafers in a DI water stop-bath for 3 min. To further harden the resist mask in preparation for etching, the developed wafers were postbaked at 100 °C for 15 min inside an oven. The resonator pattern was transferred into the Ta film in a reactive ion etching tool (SENTECH Instruments GmbH) using an SF_6 plasma with parameters: 25 sccm, 21 Pa, 200 W, 90-150 s. In order to improve the homogeneity of the etch we introduced a 30 s oxygen descum prior to SF_6 etching with parameters: 15 sccm, 20 Pa, 100 W, 30 s.

In the optical lithography recipe, a whole 2" wafer was patterned at once. Positive i-line photoresist S1805 (MICROPOSIT S1800 G2) was spun at 500 rpm for 60 s on the 2" Ta-coated wafers. Afterwards, the resist was prebaked at 115 °C for 60 s. They were then exposed with 365 nm ultra-violet mask aligner and developed in a TMAH based developer Microposit MF 319 for 30 s followed by a 2-3 min DI water stop-bath. For transferring the pattern from resist to the Ta film, RIE was used with the same parameters as used for the e-beam lithography process. After etching, the resist mask was cleaned using NEP/DMSO at 90 °C followed by solvent cleaning. As a final step, the 2" wafers were diced into 7×7 mm^2 and 15×15 mm^2 size pieces. To protect the resonator structures during dicing procedure, a layer of protective resist layer was coated with the steps shown in Table 3.1.

Protective resist coating	S1818 resist to protect wafer during dicing
acceleration	2000 rpm/s
spin speed	4500 rpm
spin time	60 s
Prebake	80°C, 5 min
Resist cleaning	NEP/DMSO at 90°C
time	DMSO (5 min hotplate + 5 min US bath)longer if resist patches remain
acetone	5 min
Ethanol	5 min
IPA	In ultrasonic bath at 3-4 power and N2 blow dry

Table 3.1: Cleanroom parameters for coating a protective resist layer for wafer dicing and resist cleaning from the diced wafers.

3.2 Resonator design

There are three types of resonator implementations widely used in the superconducting qubit community- distributed element coplanar waveguides (CPW), lumped element and 3D cavity resonators. We use lumped-element resonators consisting of a discrete inductor and a capacitor for this study. More details about the resonator circuit are discussed in Chapter 4. A circuit is considered lumped element when the size of circuit elements is smaller than the wavelength of the applied signal, which for frequency range of 4 GHz to 6 GHz corresponds to the wavelength of 4-7 cm. We started with horseshoe and meander style resonators. The naming terminology is based on their capacitor plates and meandering design of the inductor. Figure 3.4 shows six resonators

Steps	Optical lithography			E-beam lithography		
Wafer cleaning	IPA in Ultrasonic bath at maximum power for 10 min			IPA in Ultrasonic bath at maximum power for 10 min		
Baking	120°C, 2 min			120°C, 2 min		
cooldown time	2-3 min			2-3 min		
Resist	S1805 (thickness: 500 nm, positive)			maN 2410 (negative)		
acceleration	500 rpm/s			7000 rpm/s		
ramp speed	500 rpm			-		
ramp time	5 s			-		
spin speed	4500 rpm			3000 rpm		
spin time	60 s			60 s		
Prebake	115°C, 60 sec			90°C, 120 sec		
Exposure dose	13 mW/cm2			350 $\mu C/cm^2$		
wavelength	365 nm			-		
contact mode	hard			-		
time	4 s			-		
Developer	MIF-319			maD-525		
time	30 s			3-4 min		
Stop bath	DI, 2-3 minutes and N2 blow dry			DI, 2-3 minutes and N2 blow dry		
Postbake	-			120°C, 15 min		
Etching	Reactive ion etching					
Parameters	gas	flow	pressure	power	time	T
	O_2	15 sccm	20 Pa	100 W	30 s	RT
	SF_6	25 sccm	21 Pa	200 W	90 s	RT
Resist cleaning	NEP/DMSO			mr-REM 700		
HP temperature	90°C			RT		
time	DMSO (5 min hotplate + 5 min US bath) longer if resist patches remain			4 min		
acetone	5 min			4 min		
Ethanol	5 min			-		
IPA	In ultrasonic bath at 3-4 power and N2 blow dry			In ultrasonic bath at 3-4 power and N2 blow dry		

Table 3.2: Summary of parameters for optical and e-beam lithography for resonator fabrication.

in total on a single chip. For horseshoe style resonators, the gap between two ends of the outer capacitor plate was kept constant at 200 µm, only varying the inner capacitor plate length. The gap between the two capacitor plates is 50 µm. The width of the inductor wire is 10 µm and its length is the same across all horseshoe style resonators. For meander style resonators, both capacitor plates are of the same length and this length was varied. The length of the meander was kept constant in all of them. The

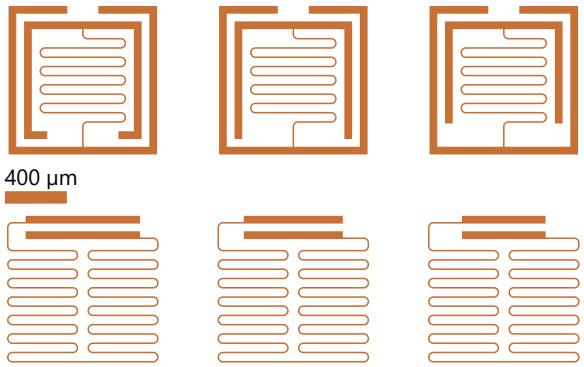

Figure 3.4: Initial resonator designs consisting of horseshoe style (top panel) and meander style (bottom panel) resonators. For horseshoe resonators, the outer capacitor plate was kept constant at 200 µm varying the inner capacitor length. For meander resonators, the length of both capacitors was varied. The length of the meander was kept constant in all of them.

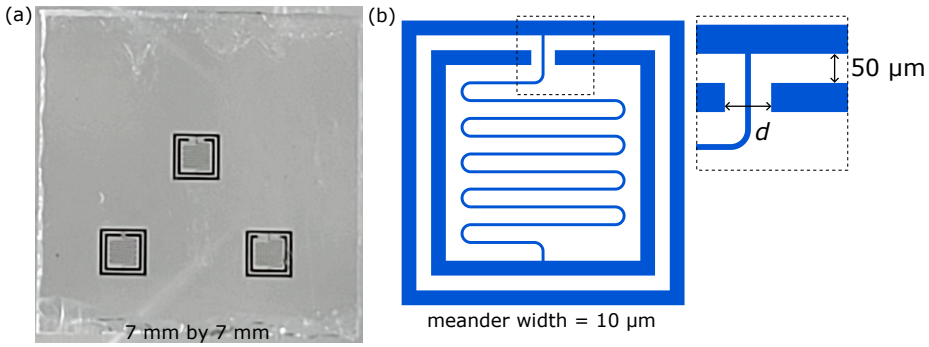

Figure 3.5: The final horseshoe resonator design and layout: (a) photograph of a sample with three resonators (b) a modified design of the horseshoe resonator with a closed loop outer capacitor plate and gap d between inner capacitor pads is varied. The width of meander wire is same for all them at 10 µm.

gap between capacitor plates and the width of the inductor wire are the same as in horseshoe style resonators. The two type of designs were used to achieve different coupling strengths. The highest coupling quality factor is achieved by the horseshoe style resonators with the largest capacitor plates and is $\approx 1 \times 10^6$.

As Ta film deposition and resonator fabrication processes improved over time resulting in overall better quality of resonators with Q_i close to 1 million. These designs were limited by the coupling strength and therefore, modifications and completely new designs were needed. Therefore, the meander style resonator was discontinued and modifications in the horseshoe style resonator design with initial highest coupling quality factor were made by completely closing the outer capacitor plate and increasing the length of inner capacitor plate as shown in Fig. 3.5(b). We fabricated samples of 7×7 mm^2 size containing 3 modified horseshoe style resonators and these samples were fabricated using both e-beam and optical lithography.

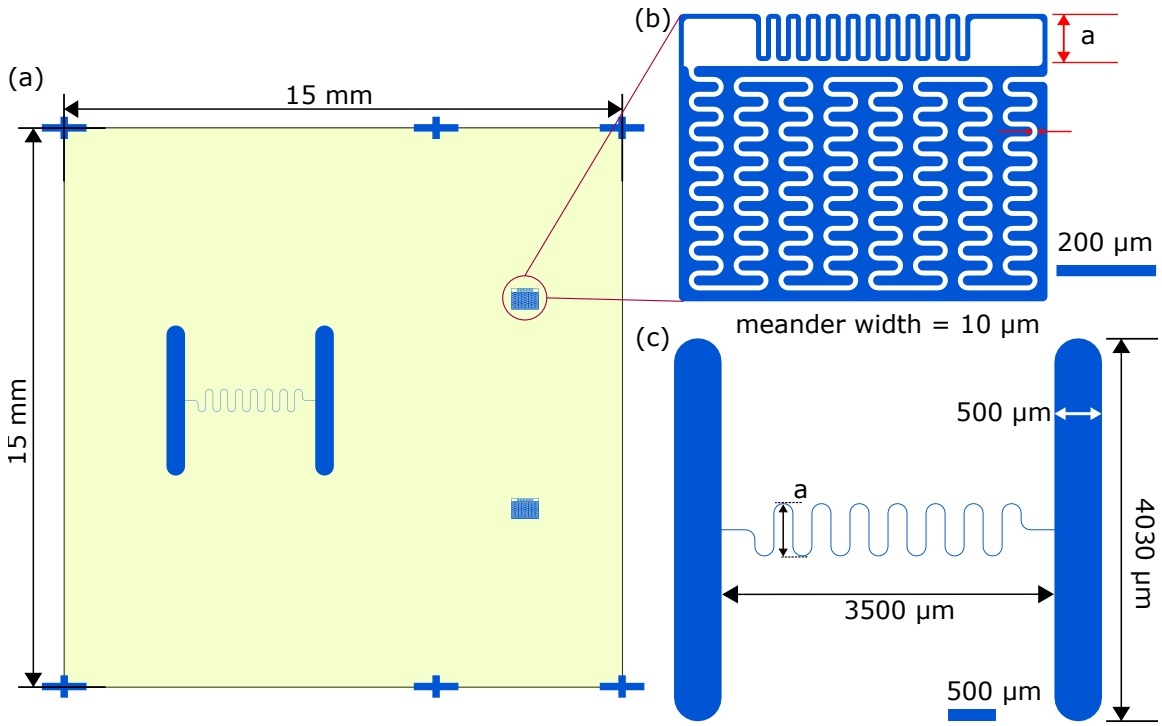

Figure 3.6: (a) Resonator layout for the aluminum 3D-waveguide. Each sample contains 3 resonators in total: two interdigitated as shown in (b) one diluted as shown in (c). In both resonator designs, the amplitude of meander a is varied keeping the capacitor unchanged. The width of meander wire is the same for all of them at 10 µm.

Figure 3.6(b),(c) show two additional resonator designs that were introduced with main focus on varying the capacitor gap and are referred to as interdigitated and diluted. The interdigitated resonator has a small foot-print and consists of tightly packed capacitor fingers with a gap of 10 µm. To vary the resonance frequency, the inductor length is varied keeping the capacitor same. We fabricated 15×15 mm^2 size samples containing one diluted and two interdigitated style resonators and these samples were fabricated using only optical lithography.

3.3 3D-waveguide sample holder

3D-waveguides are hollow metallic tube like structures with a rectangular cross-section used to propagate electromagnetic waves, particularly at microwave frequencies. They allow propagation of only TE and TM modes as they are composed only of a single conductor. They play an important role in superconducting circuits by providing a low

Sample	Ta-phase	Lithography	resonator style
S1	$\alpha(110)+\beta(002)$	e-beam	Horseshoe
S2	$\alpha(111)$	e-beam	Horseshoe
S3	$\alpha(111)$	optical	Horseshoe
S4	$\alpha(111)$	optical	Horseshoe
S5	$\alpha(110)$	e-beam	Horseshoe
S6	$\alpha(110)$	e-beam	Horseshoe
S7	$\alpha(111)$	optical	Horseshoe
S8	$\alpha(111)$	optical	Horseshoe
S9	$\alpha(111)$	optical	Interdigitated and diluted
S10	$\alpha(111)$	optical	Interdigitated and diluted

Table 3.3: List of samples fabricated with the used lithography technique and the type of resonators patterned on them.

loss environment for resonator characterization. Each mode has a cutoff frequency f_c defined by [166]

$$f_{c\,m,n} = \frac{c}{2\pi}\sqrt{\left(\frac{m\pi}{a}\right)^2+\left(\frac{n\pi}{b}\right)^2} \tag{3.1}$$

where, a is the larger, b is the smaller of the cross section dimensions of the waveguide and c is the speed of light. For $m = 1$ and $n = 0$, the $TE_{1,0}$ has the lowest cutoff frequency

$$f_c = \frac{c}{2a} \tag{3.2}$$

At frequencies lower than the cutoff frequency for a certain mode, the propagation constant becomes entirely imaginary, leading to an exponential decay of the fields. These modes are termed cutoff modes or evanescent modes. Due to the presence of a cutoff frequency below which propagation is inhibited, the behavior of the waveguide mode propagation resembles that of a high-pass filter response.

In this work, two 3D waveguides were used as shown in Fig. 3.7, which provides a low loss environment for resonator characterization [57]. These home-built waveguides were inherited from previous works of [58, 167] in our group. They differ in their size and the material they are made of. The first waveguide is made from copper and it can house 7×7 mm^2 chips and will be referred to as waveguide-A. It has two input ports: one of them is impedance matched to the 50 Ω coaxial cables using a copper cylindrical stub with a radius of 2 mm and length 3 mm. It acts as drive port and was used as the input port for resonator measurements. The second port, is located closer to where the sample is mounted inside the waveguide. It is not impedance matched and can be used as a separate drive port for measurements involving qubits. The inner hollow volume of

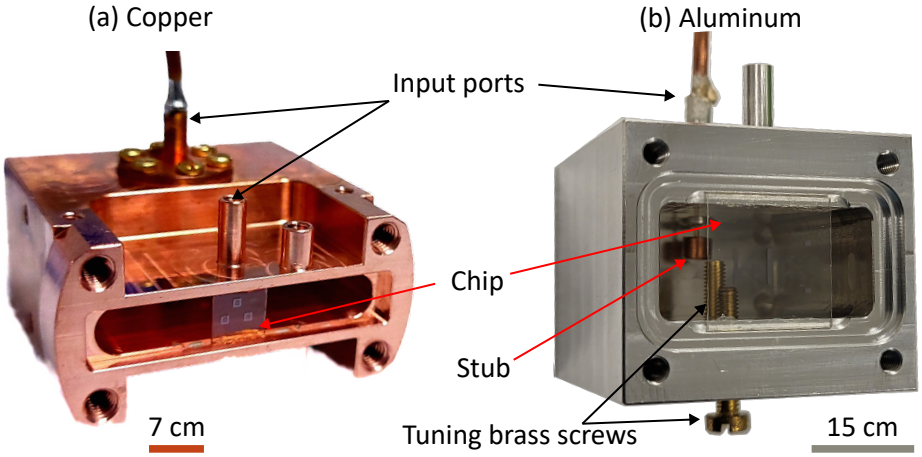

Figure 3.7: 3D waveguide sample holders made of (a) copper, referred to as waveguide-A and (b) aluminum, referred to as waveguide-B.

the waveguide has dimensions $l \times b \times h$ of $6 \times 36 \times 47$ mm. Notice, that the waveguides have not sharp but curved edges. Therefore, Eq. (3.1) is only partially applicable and the approximate cutoff frequency is 4.2 GHz. Horseshoe style resonators were measured using this waveguide

The second waveguide is made of aluminum, accommodating larger samples sized 15×15 mm^2, and will be termed waveguide-B. Bulk aluminum becomes superconducting at 1.2 K. At operating temperatures in mK range, the Al waveguide offers the additional benefit of magnetic shielding from stray fields potentially emanating from nearby components such as the circulator. As our measurements did not require use of magnetic fields, we opted for aluminum as the waveguide material in our newer resonator designs. The inner hollow volume of the waveguide has dimensions $l \times b \times h$ of $12.9 \times 25.8 \times 34$ mm. It features rounded edges with an approximate cutoff frequency of 5.8 GHz, which is comparatively larger than that of waveguide-A. This higher cutoff frequency allowed for designing resonators with significantly different footprints i.e. diluted and interdigitated resonators, while maintaining their resonant frequency below the cutoff frequency of the waveguide. There are brass tuning screws inserted of the bottom of the waveguide which can be used to fine tune the impedance matching. Waveguide-A is equipped with one screw, whereas waveguide-B features two screws for this purpose.

A sapphire chip is fixed inside the waveguide at a quarter wavelength distance from the waveguide lid, at the maximum of the electric field. They are secured in the waveguide using vacuum grease, which solidifies at cryogenic temperatures to aid in the chip's thermalization. The waveguide lid is closed tightly using four brass screws.

3.3.1 Finite element simulations

To predict the resonance frequency, f_r and coupling quality factor Q_c of each resonator in the 3D waveguide before actual experiments, we use a commercial finite-element simulation software *Ansys* High Frequency Structure Simulator (HFSS). In Ansys design creation, there are two primary component types: 2D surfaces, like sheets or 3D object faces, and 3D solids. Solids are used to model bulk materials, such as the waveguide body, substrates, impedance matching port and the tuning screw, reflecting attributes like material permittivity and bulk dielectric loss. Surfaces are best for modeling thin films, such as resonators in this context.

In the simulation, the waveguide model consists of a copper or aluminum body, as shown in Fig. 3.8(b), and is assigned a perfect conductivity boundary condition. The inside of the copper body is filled with vacuum. The tuning screws entering through the bottom are considered by a copper rod. Within the waveguide body lies a sapphire substrate with a thickness of 350 µm, characterized by a relative permittivity of $\varepsilon_r = 10$ and a relative permeability of $\mu_r = 1$. Eigen mode simulations are performed to extract the eigen modes of a resonant circuit with varied capacitor gap denoted by the white

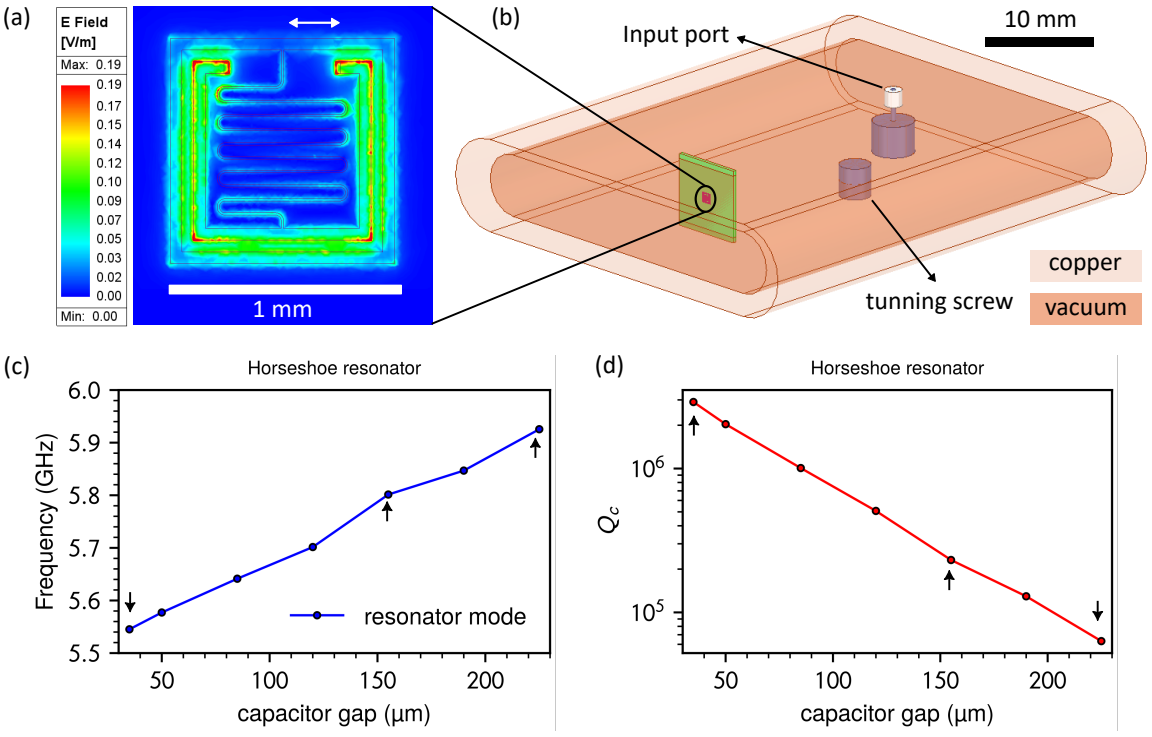

Figure 3.8: HFSS finite element simulations for the horseshoe resonator (a) Simulated distribution of the electric field magnitude at the plane of the resonator. (b) waveguide model used for simulation. (c) and (d) are f_r and Q_c, respectively as a function of capacitor gap which is denoted by the white arrow in (a). The black arrows below data markers show the capacitor gap used in the resonators mask.

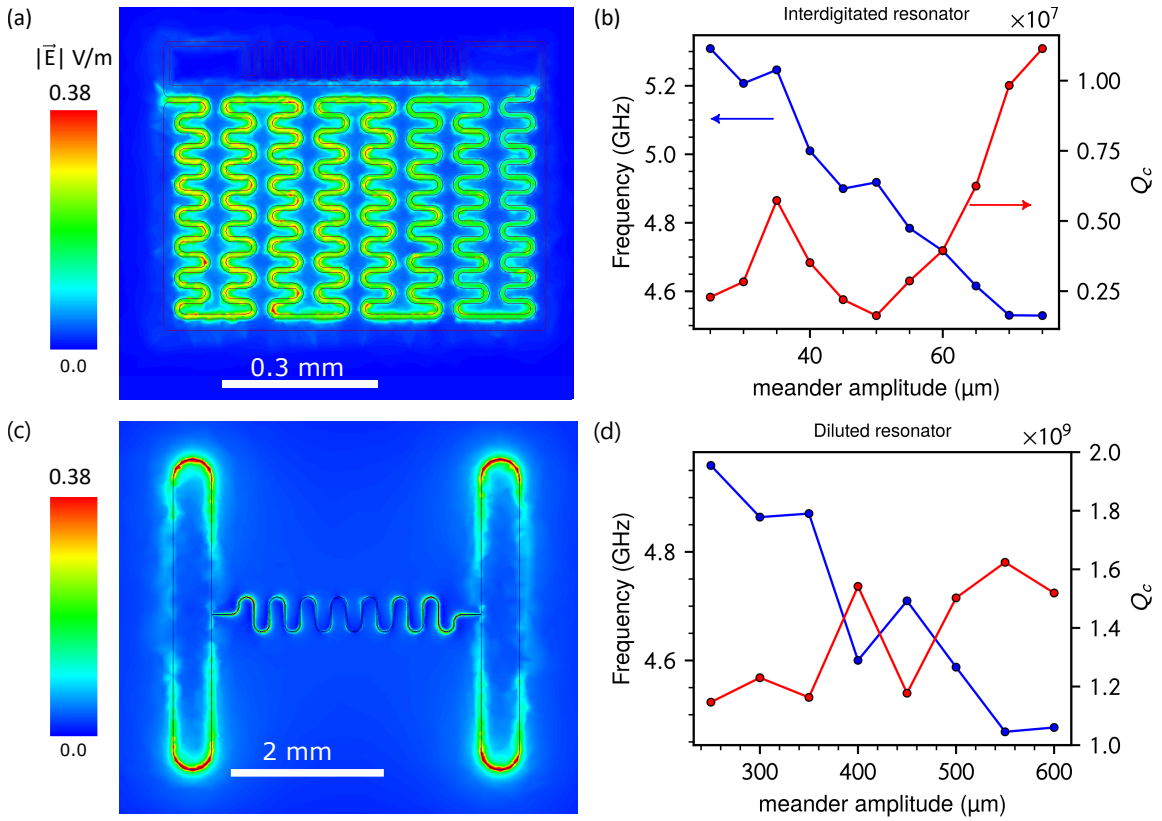

Figure 3.9: HFSS simulations of f_r and Q_c for interdigitated and diluted resonators.

arrow in Fig. 3.8(a). The simulated electric field distribution in one of the resonators is illustrated in Fig. 3.8(a). The amplitude of the field is higher between the capacitor pads of the resonators. Additionally, the coupling strength to the electric field decreases with further closing the inner capacitor loop, as shown in Fig. 3.8(d). Similarly, the simulation was performed for interdigitated and diluted resonators and the results are shown in Fig. 3.9. We also calculate the metal-substrate participation ratio p_{MS} as discussed in Eq. (1.23). We are mainly interested in the loss contribution from the metal-substrate interface. For simulation, we assume an interface thickness of 3 nm and a relative dielectric constant of 10 for sapphire [168].

3.4 Cryostat setup

The microwave measurements in this work were performed in a BlueFors LD400 dilution cryostat with a base temperature of ≈ 10 mK. The outer vacuum shield of the cryostat is equipped with a μ-metal shield to reduce background magnetic fields. The cryostat is fitted with microwave coaxial cables that carry the signal from room temperature, through the different temperature stages all the way to the base of the cryostat. Attenuators

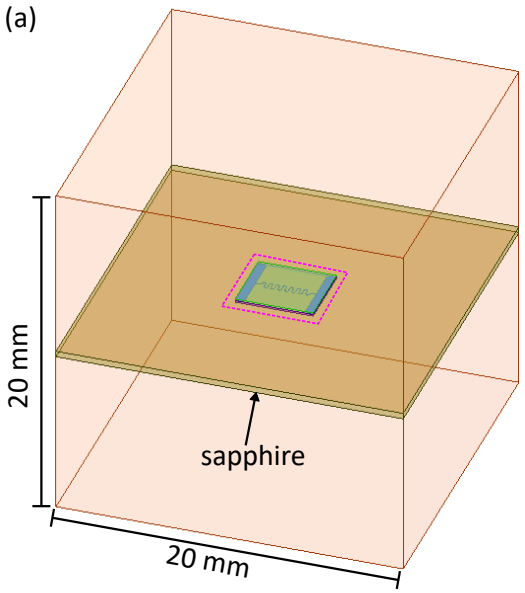

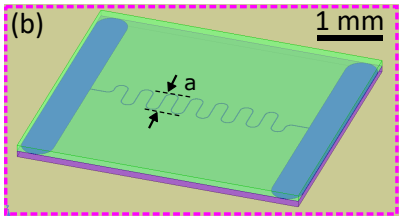

meander amplitude, a(µm)	f_r (GHz)	P_{MS}
250	5.024	4.14×10^{-6}
300	4.910	3.67×10^{-6}
350	4.799	3.35×10^{-6}
400	4.649	3.61×10^{-6}
450	4.550	3.58×10^{-6}
500	4.453	3.51×10^{-6}
550	4.342	3.43×10^{-6}

Figure 3.10: Simulation model for the energy participation ration calculation. (a) The outer box with 20 mm each side is vaccum while the top and bottom surfaces have perfect conductor boundary condition. (b) zoom-in view of the resonator and the volume.

and low-pass filters were installed in the microwave input line to reduce the incoming thermal noise reaching the sample. On the other hand, amplifiers are used on output line to amplify the signal which includes a high-electron mobility transistor (HEMT) amplifier at 4 K stage and additional wideband amplifier at room temperature. An isolator is installed at base temperature to attenuate the signal coming back from higher temperature stages. Figure 3.11 shows the wiring diagram and various components inside the cryostat. The samples are glued with vacuum grease inside the 3D-waveguide which is then anchored to the mixing chamber plate to ensure good thermalization.

The resonator measurements were carried out using a two port VNA. The outgoing microwave signal from a VNA was attenuated by 60-70 dB in total at various cryogenic stages before reaching the resonator through a circulator. The response signal from the resonator was amplified by HEMT and by a room-temperature amplifier before it was recorded by the VNA.

3.5 Post-processing of Ta using buffered oxide etch

One of the ways to improve resonator performance is to treat the film surface with BOE . Like many other metals, Ta also forms native oxide layer when it comes in contact with oxygen environment. The most stable and common stoichiometry for Ta surface oxide is Ta_2O_5 [169], sub-oxides TaO_x with varied oxygen stoichiometries are also found. These surface oxides have different material properties than that of the Ta film. Due to the

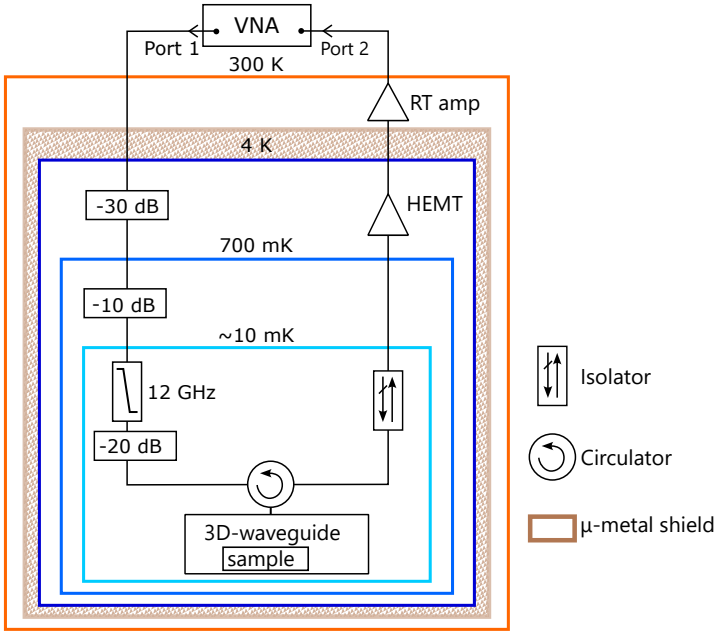

Figure 3.11: Microwave setup in dilution cryostat for resonator characterization. The input line to the waveguide is attenuated and filtered by a low-pass filter. Output line includes an isolator followed by an additional low-pass filter. The signal is then amplified using a commercial high electron mobility transistor amplifier (HEMT) attached to the 4 K stage and a room temperature (RT) amplifier.

amorphous nature of the oxide, they are one of the main source of two-level-system losses in superconducting quantum circuits [106]. There are multiple ways to eradicate or reduce surface oxides by surface encapsulation with another material [39, 103, 106] or by etching the surface oxide prior to device measurements[38, 170]. Buffered oxide etchant is a solution of hydroflouric acid HF and ammonium fluoride NH_4F. It is commonly used to dissolve silicon dioxide but also etches Ta surface oxide yet at a much smaller rate.

This section discusses the details of post-processing for resonators that have been already measured once in a cryostat. Apart from etching the surface oxide and cleaning the surface by removing hydrocarbon residues, BOE has the potential to cause structural changes[171]. Hydrogen poisoning is another possible outcome of BOE treatment [172]. To detect any changes, the BOE treated films are re-characterized using some of the techniques presented in Chapter 2. The primary aim is to only assess films that have produced high-quality resonators post-BOE treatment i.e. S1 and S2. Nonetheless, some analyses included all the films.

The resonators were immersed in BOE 7:1 ($HF : NH_4F = 12.5 : 87.5\%$), which is 7 parts 12.5% HF mixed with 1 part 87.5% NH_4F, for 15 min at room temperature. This was followed by three subsequent DI water baths and finally blown dry with nitrogen gas. It's important to be aware that the resonator chips are mounted inside the 3D-waveguide

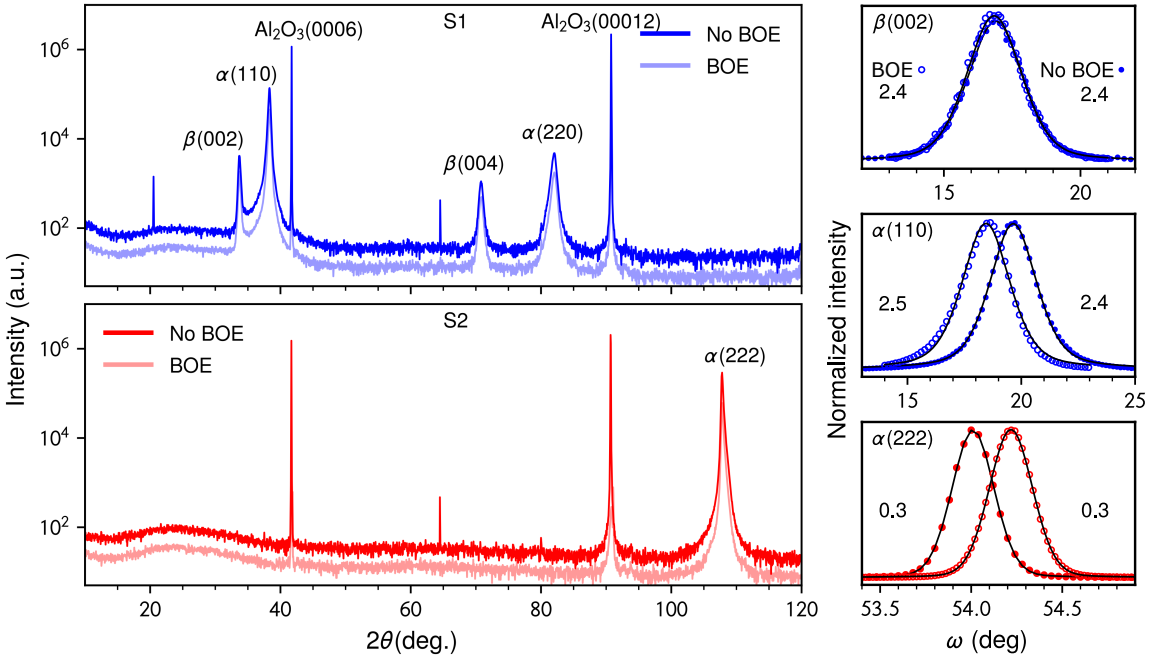

Figure 3.12: Comparision of x-ray diffractograms of S1 and S2 before and after (dark colored) performing 15 min of buffered oxide etch (BOE). The three subplots on right show the rocking curves for $\alpha(110)$ and $\beta(002)$ peaks of S1 and $\alpha(222)$ peak of S2 before (filled markers) and after (empty markers) 15 min of BOE. The black lines in rocking curves are fit to the measured data using a pseudo-Voigt function and the mosaicity is determined form the FWHM of the fit.

sample holder using vacuum grease applied to the top and bottom edges of the chip. Consequently, for any further post processing, it is necessary to remove vacuum grease to avoid contamination. Vacuum grease is challenging to remove with regular solvents and requires use of xylene or toluene. The chips were taken out of the waveguide and were cleaned by dipping them in xylene followed by an acetone bath and IPA in ultrasonic bath.

3.5.1 X-ray diffraction

Figure 3.12 shows comparison of XRD and rocking curves of Ta peaks in films S1 and S2 before and after 15 min of BOE. There is no shift visible in any Ta peaks after BOE. Also, the mosaicity remains same except for $\alpha(110)$ peak.

3.5.2 X-ray Photoelectron Spectroscopy

X-ray Photoelectron Spectroscopy (XPS) is employed to analyze the surface of Ta. XPS is a surface sensitive analytical technique and is based on the photoelectric effect. When

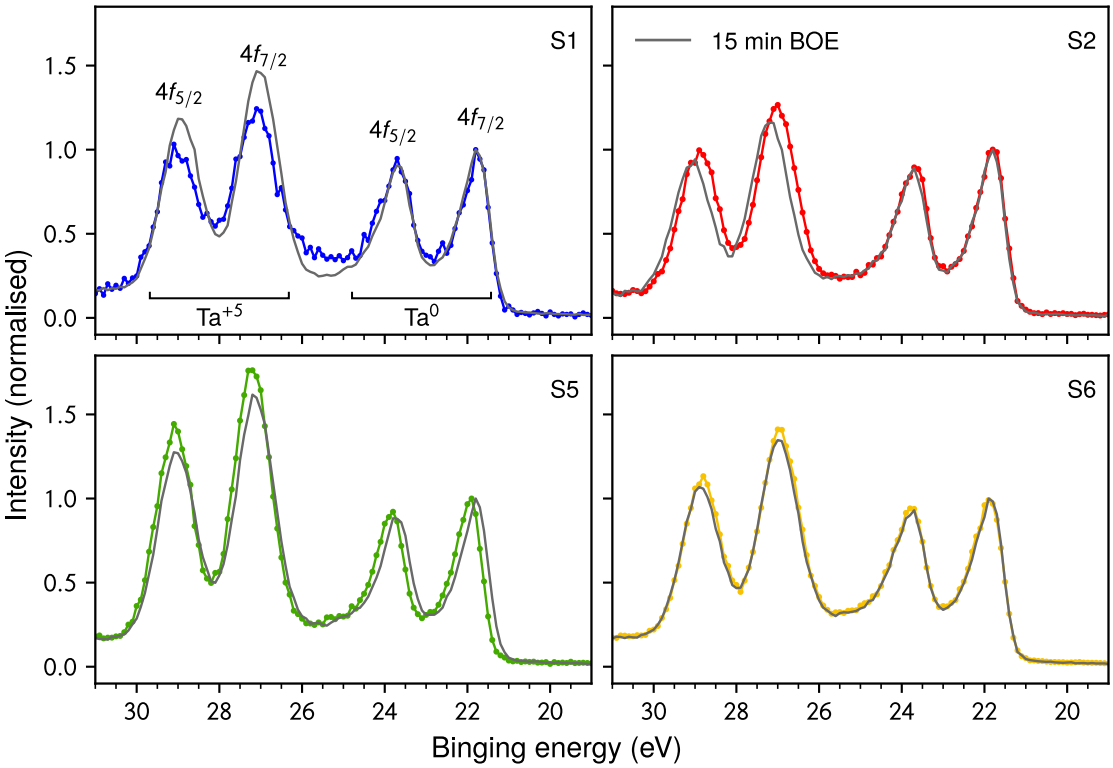

Figure 3.13: XPS analysis of Ta surface before and after 15 min BOE. The intensity is normalised to the metallic Ta $4f_{7/2}$ peak.

x-rays with sufficient energy $h\nu$ strike the surface of a material, they cause emission of (photo)electrons from the core of the atoms. The kinetic energy of the emitted electrons is measured which is related to the binding energy E_B by

$$h\nu = E_B + E_{kin} \tag{3.3}$$

XPS is particularly sensitive to surface because only the electrons near the surface can escape with sufficient energy after they travel through the material without loosing their energy due to scattering. It is also able to reveal chemical state information from the elements in the sample.

XPS was carried out using an Omicron XM 1000 MkII with an Al-K_α X-ray (1486.6 eV) source at an operating power of 300 W. The spectra were acquired with a SPECS Phobias 150 spectrometer and the XPS data were analyzed using CASAXPS® software.

Figure 3.13 shows Ta 4f spectrum of four Ta films S1, S2, S5 and S6 before and after 15 min BOE. There are four peaks in each spectrum corresponding to two different chemical states of Ta, each represented by a pair of spin–split $4f_{7/2}$–$4f_{5/2}$ peaks. Peaks at lower BE, 22 and 23.5 eV, are due to metallic Ta, and the corresponding pair of peaks due to Ta atoms bonded to O (Ta-O), at 27 and 29 eV.

Sample	No BOE			After 15 min BOE		
	T_c (K)	RRR	Sample state	T_c (K)	RRR	Sample state
S1	4.2	4	Diced chip[1]	4.1	4	Patterned[2]
S2	4.3	95	Diced chip[1]	3.7	2	patterned[2,3]
S3	4.3	77	Patterned, Hall bar	4.3	77	Patterned, Hall bar
S4	4.3	93	Patterned, Hall bar	4.3	62	Patterned, Hall bar
S5	4.2	6.2	Diced chip[1]	4.1	5.6	Patterned[2]
S6	4.3	9.2	Diced chip[1]			

Table 3.4: DC transport measurements using four probe method: Superconducting transition temperature (T_c) and residual resistance ratio (RRR) of Ta films before and after buffer oxide etchant treatment.
[1] Before patterning
[2] Contacted meander through wire bonds on capacitor plates of resonator
[3] BOE and annealed for 20 min

Previous reports by [5, 38, 173] have shown the reduction of surface oxide thickness after BOE to different extent. Contrary, we do not observe any significant change in the surface oxide thickness after BOE.

3.5.3 DC transport measurements

T_c was measured again on samples that went through BOE post-processing using the same method explained in Chapter 2 . After BOE treatment, RRR remains the same for most samples with an exception in case of S2. The drastic decrease in RRR of S2 can be explained by the multiple BOE steps and annealing at 800 °C inside the high vacuum sputtering chamber for 20 min. The lower T_c of S2 after several steps of post-treatment was measured by directly contacting the meander inductor of the resonator. Therefore, it is unclear whether the change was due to different measurement conditions or post-treatment steps.

4 Correlating Ta structure with microwave loss

Does a film possessing superior superconducting and structural properties, along with higher degree of order, result in reduced microwave losses? To find the answer, this chapter undertakes detailed microwave characterization of Ta resonators fabricated from films exhibiting varied structural and material properties. As microwave resonators play a central role in this chapter, we first present their circuit analysis and a brief overview of resonators figures of merit. Finally, we examine the microwave performance as a function of photon number and temperature for different resonator geometries. The analysis also includes the effect of post-processing the measured chips using buffered oxide etch (BOE).

4.1 Microwave resonators

Superconducting microwave resonators are an important component in building superconducting circuits. They are versatile components with applications in qubit measurements such as readout [174] and manipulation, coupling qubits to surrounding qubits, Purcell filters [175, 176] and parametric amplifiers [17]. Additionally, they serve as a convenient tool to study material specific losses in superconducting circuits. Instead of directly constructing a qubit, which often involves complex fabrication processes and is resource-intensive, resonators are used as proxy elements [23] which aids in accelerated progress toward improved coherence in superconducting circuits. By measuring the resonator and extracting parameters like quality factor, kinetic inductance fraction and superconducting transition temperature, one can gather information about the properties and performance potential of the final qubit.

4.1.1 LCR circuit analysis

The operating frequency of our resonators lies in the $4-6\,\mathrm{GHz}$ range, corresponding to wavelengths between 4 and 7 cm. These wavelengths are considerably larger than the physical dimensions of the resonators [cf. Section 3.2]. As a result, the resonator

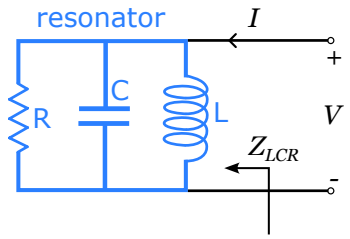

Figure 4.1: Parallel LCR circuit

circuits can be accurately modeled using a lumped-element approach, where voltage and current are assumed to remain approximately constant across each circuit element.

Resonators are composed of two main circuit elements, a capacitor C that stores energy in the electric field and an inductor L that stores energy in its magnetic field. An effective resistance R is used to incorporate all resonator losses. The resonators can be modeled using a parallel LCR circuit as shown in Fig. 4.1. The input impedance of such a circuit is given by

$$Z_{LCR} = \left(\frac{1}{R} + \frac{1}{i\omega L} + i\omega C\right)^{-1} \tag{4.1}$$

The complex power delivered to the resistor R from an external source is

$$P_{in} = \frac{1}{2}\frac{|V|^2}{Z^*_{LCR}} = \frac{1}{2}|V|^2\left(\frac{1}{R} + \frac{i}{\omega L} - i\omega C\right) \tag{4.2}$$

and the power dissipated by the resistor R is given by

$$P_{loss} = \frac{1}{2}\frac{|V|^2}{R} \tag{4.3}$$

The average electric and magnetic energy stored in capacitive and inductive elements, respectively is

$$E_C = \frac{1}{4}C|V|^2 \tag{4.4}$$

$$E_L = \frac{1}{4}L|I_L|^2 = \frac{|V|^2}{4\omega^2 L} \tag{4.5}$$

The resonance condition is fulfilled when energy stored in the capacitive element and in the inductive element becomes equal or when the imaginary part of Z_{LCR} vanishes. Therefore, using Eqs. (4.4) and (4.5), the resonance frequency of a LCR circuit is given by

$$\omega_0 = \frac{1}{\sqrt{LC}} = 2\pi f_0 \tag{4.6}$$

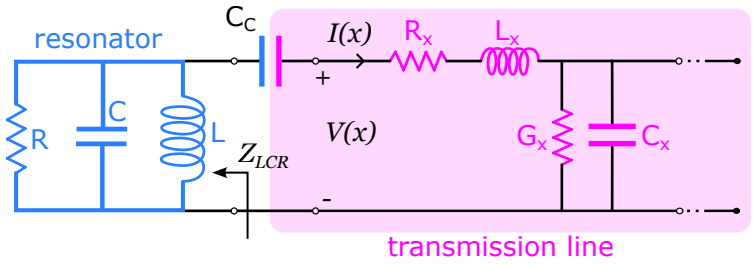

Figure 4.2: Circuit diagram of LCR resonator coupled to a transmission line through capacitor C_c.

4.1.2 Coupling to external circuit

For practical applications, resonators need to be coupled to the external measurement circuit in order to be readout. This coupling can be achieved either capacitively, where the two circuits share a common electric field or inductively [177], where they share a common magnetic field. Figure 4.2 shows circuit diagram of a parallel LCR resonator capacitively coupled to a transmission line. The input impedance Z_{in} of the overall circuit includes coupling capacitance C_c as well as the resonator capacitance C and is given by

$$Z_{in} = Z_c + Z_{LCR} = \frac{1}{i\omega C_c} + \left(\frac{1}{R} + \frac{1}{i\omega L} + i\omega C\right)^{-1} \tag{4.7}$$

In addition, the resonance frequency of the circuit shifts due to C_c and is given by

$$\omega^* = \frac{1}{\sqrt{L(C + C_c)}} \tag{4.8}$$

4.1.3 Quality-factor of resonator

The key parameter for evaluating resonator performance is the quality-factor Q. This dimensionless quantity indicates the resonator's quality or its lossiness. There are two common ways to define Q. The first is defined as the ratio of average energy stored in the resonator to the energy lost per oscillation or cycle [166]

$$Q = 2\pi \frac{\text{average energy stored}}{\text{energy loss/cycle}} = 2\pi f_0 \frac{E_C + E_L}{P_{loss}} \tag{4.9}$$

Average energy stored in a resonator circuit is given by the sum of E_C and E_L. Using Eqs. (4.3) to (4.5), Q can be rewritten in terms of circuit elements R and C

$$Q = 2\pi f_0 \frac{2E_C}{P_{loss}} = 2\pi f_0 \frac{2E_L}{P_{loss}} = 2\pi f_0 RC \tag{4.10}$$

Note that the quality factor increases as the R increases. To understand this, consider Eq. (4.3), where the energy loss in the parallel lumped-element circuit is inversely proportional to R. This means, as R increases, energy loss decreases, leading to a higher quality factor.

The second definition of Q is the ratio of resonant frequency f_0 to the full-width at half-maximum (FWHM) bandwidth δf:

$$Q = \frac{f_0}{\delta f} \tag{4.11}$$

This formulation is particularly useful when the resonator's stored energy is expressed in terms of photon number n, where the photons have frequency f. Higher value of Q implies lower rates of energy losses and a higher quality.

So far, we were addressing energy losses within an isolated resonator circuit. When coupling to the feedline, an additional pathway for energy dissipation into the external circuit is introduced, quantified by the coupling quality factor Q_c. Consequently, the total energy loss can be classified into two types: intrinsic material losses and losses attributed to the external circuitry. Taking coupling into account, both Q_i and Q_c can be expressed as:

$$Q_i = \omega^* R(C + C_c) \tag{4.12a}$$

$$Q_c = \frac{C + C_c}{\omega^* Z_0 C_c^2} \tag{4.12b}$$

Thus, the overall performance of the resonator is given by the loaded quality factor, Q_l which can be written as

$$\frac{1}{Q_l} = \frac{1}{Q_i} + \frac{1}{Q_c} \tag{4.13}$$

where, Q_i is an intrinsic parameter that depends on material properties of the resonator, whereas Q_c is a design-related parameter. The resonator can be operated in three different coupling regimes depending on values of Q_i and Q_c, with each regime suited for specific resonator application:

1. under-coupled ($Q_i < Q_c$): In the weak coupling regime, the resonator interacts weakly to the feedline. In this case, the incoming microwave energy is more likely to get dissipated into the resonator. Undercoupled resonators are suitable for memory devices [178, 179].

2. critically-coupled ($Q_i \simeq Q_c$): The rate of photon dissipating into the resonator is equal to the loss to the feedline. This regime is suitable for studying loss mechanisms, highly relevant for this work.

3. over-coupled ($Q_i > Q_c$): In the strong-coupling regime, resonator interacts strongly with the feedline and hence is more likely to dissipate microwave photons to the feedline than in the resonator itself. This regime is desirable for readout resonators [180].

4.1.4 Reflection coefficient

To measure a resonator, it is first coupled to a transmission line through which microwaves are sent, and the resulting response is measured. From this response, key parameters such as f_0, Q_i and Q_c can be extracted. In our setup, the resonator is coupled to the input port of a 3D-waveguide (details in Section 3.3) via a coupling capacitor C_c. The microwave propagation in transmission line terminated in a load impedance, Z_{in} given by Eq. (4.7), can be derived using *telegrapher equations* [166]. A segment of transmission line can be modeled as a lumped-element circuit characterized by per-unit-length parameters: R_x series resistance, L_x series inductance, G_x shunt conductance and C_x shunt capacitance. Since there is a impedance mismatch between the load impedance and characteristic impedance of transmission line, $Z_{in} \neq Z_0$. The voltage(current) have a forward or incident, $V^+(I^+)$ and a backward or reflected propagating signal $V^-(I^-)$. Thus, at any position x in the transmission line, voltage and current can be written as

$$V(x) = V^+ e^{-\gamma x} + V^- e^{\gamma x} \tag{4.14a}$$

$$I(x) = I^+ e^{-\gamma x} + I^- e^{\gamma x} \tag{4.14b}$$

where $\gamma = \sqrt{(R_x + i\omega L_x)(G + i\omega C_x)}$ is the complex propagation constant. The characteristic impedance Z_0 of the line is given by

$$Z_0 = \frac{V^+}{I^+} = -\frac{V^-}{I^-} = \sqrt{\frac{R_x + i\omega L_x}{G_x + i\omega C_x}} \tag{4.15}$$

Under the condition of a lossless transmission line i.e. resistance R_x and conductance G_x are negligible, Z_0 becomes $\sqrt{L/C}$. At the boundary $x = 0$, to fulfill the impedance mismatch boundary condition, $Z_{in} \neq Z_0$, the ratio of voltage to current must be Z_{in}.

$$Z_{in} = \frac{V(x=0)}{I(x=0)} = \left(\frac{V^+ + V^-}{V^+ - V^-}\right) Z_0 \tag{4.16}$$

Rearranging the above equation to obtain an expression for the reflected signal, one can define the voltage reflection coefficient, Γ as the ratio of reflected to incident voltage amplitude,

$$\Gamma = \frac{V^-}{V^+} = \frac{Z_{in} - Z_0}{Z_{in} + Z_0} \tag{4.17}$$

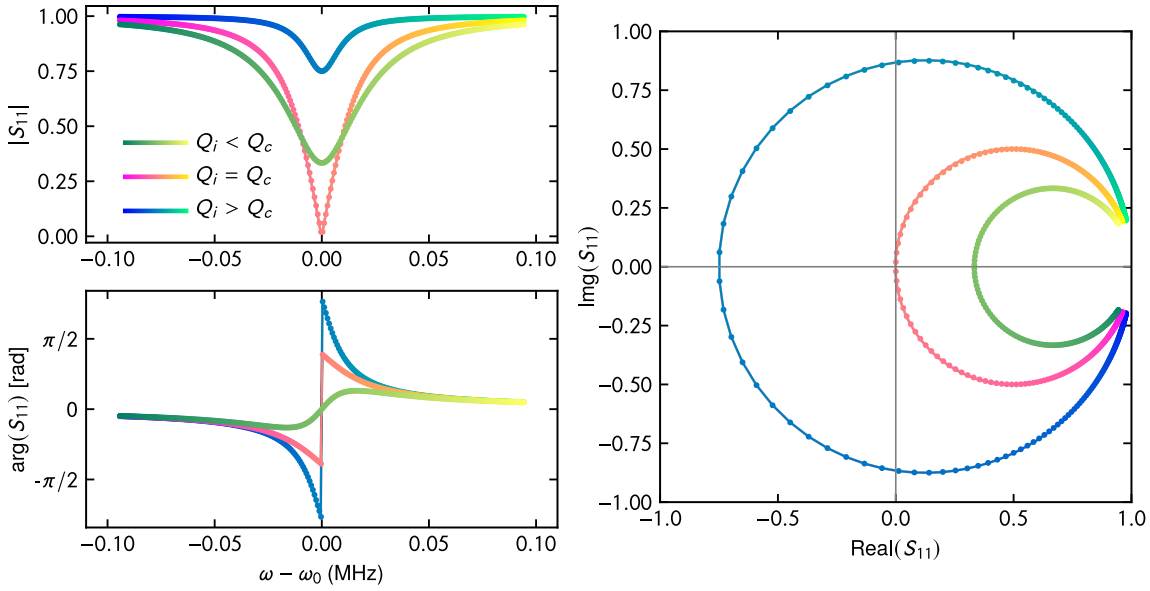

Figure 4.3: Amplitude (left top) and phase (left bottom) of complex reflection coefficient S_{11} as a function of swept frequency calculated using Eq. (4.20). (Right) S_{11} traces a circle in complex plane in clockwise direction as shown by the color gradient. Each panel shows response for overcoupled, critically coupled and undercoupled resonators.

The relevant scattering matrix for a two port circuit is

$$\begin{bmatrix} V_1^- \\ V_2^- \end{bmatrix} = \begin{bmatrix} S_{11} & S_{12} \\ S_{21} & S_{22} \end{bmatrix} \begin{bmatrix} V_1^+ \\ V_2^+ \end{bmatrix} \tag{4.18}$$

We measure resonator in reflection mode using a commercial two port vector network analyzer (VNA). Theoretically, the microwave signal is sent to the resonator from port 1 and the reflected signal is measured back at port 1 as a function of signal frequency. In practice, the reflected signal is channeled to port 2 of the VNA via a separate line using a circulator or a directional coupler. The relevant S-parameter in this case is S_{11} (measured as S_{21} on the VNA) and has the same form as Eq. (4.17). Inserting Z_{in} from Eq. (4.7) in Eq. (4.17) and rewriting the expression in terms of quality factors Q_i and Q_c and ω, it is given by:

$$S_{11}(\omega) = \frac{\delta\omega - i\omega^* \left(\frac{1}{2Q_\mathrm{i}} - \frac{1}{2Q_\mathrm{c}}\right)}{\delta\omega - i\omega^* \left(\frac{1}{2Q_\mathrm{i}} + \frac{1}{2Q_\mathrm{c}}\right)} \tag{4.19}$$

where, $\delta\omega = \omega - \omega^*$ and we are in the limit $\delta\omega \ll \omega^*$. For complete derivation, refer to [181].

$$S_{11}(\omega) = \frac{\delta\omega^2 + \frac{\omega^{*2}}{4}\left(\frac{1}{Q_\mathrm{i}^2} - \frac{1}{Q_\mathrm{c}^2}\right) + \frac{i\omega^*\delta\omega}{Q_\mathrm{c}}}{\delta\omega^2 + \frac{\omega^{*2}}{4Q_\mathrm{i}^2}} \tag{4.20}$$

The function S_{11} forms a circle in the complex plane. We measure the reflection coefficient S_{11} as a function of frequency by sweeping frequency of the input signal in the vicinity of resonator frequencies. Then we fit the phase and amplitude of the S_{11} in complex plane using a circle fit[182, 183] procedure to obtain Q_i and Q_c. The response of Eq. (4.20) for three different coupling regimes explained in Section 4.1.3 is shown in Fig. 4.3.

4.2 Loss mechanisms varying with photon number

Evaluation of superconducting circuits at the single photon level is crucial as this is the typical operating point for these systems. By measuring resonator quality factors at single-photon levels, we gain insights into the losses of the circuits. Dielectric losses from TLS are believed to dominate the superconducting circuits in the single-photon regime at mK temperatures [47]. The photon number and temperature dependence of TLS losses is given by [23]

$$Q_\mathrm{TLS}(\bar{n}, T) = Q_\mathrm{TLS,0}\left(\frac{\sqrt{1+\frac{\bar{n}}{n_c}}}{\tanh(\frac{\hbar\omega}{2k_BT})}\right) \tag{4.21}$$

where, $Q_{TLS,0}$ is the quality-factor at low photon number, $\bar{n}$ is the average photon number, n_c is the critical photon number at which the TLS saturates, $\hbar$ is the reduced Planck constant and k_B is the Boltzmann constant. Typically, Q_i rises with increasing power, indicating it is linked to a saturable loss mechanism. Although, in literature, it is frequently attributed to the broad notion of two-level systems [54], other loss mechanisms that saturate with power exist, such as excess quasiparticles [21, 184].

In this section, we characterize Ta resonators by measuring their Q_i, Q_c and f_r as a function of incoming microwave power P_{in} at constant temperature $\approx 15\,\mathrm{m\,K}$ before and after treating resonators in buffered-oxide etch. Three different resonator geometries (see 3.2) were measured. The estimation of the average photon number $\bar{n}$ at the resonator corresponding to the power of incoming microwave tone is given by [58]

$$\bar{n} = \frac{\langle E_{in}\rangle}{\hbar\omega_0} = \frac{2}{\hbar\omega_0}\frac{Q_\mathrm{l}^2}{Q_\mathrm{c}}P_{in} \tag{4.22}$$

where, $\langle E_{in}\rangle$ is the average energy stored in the resonator.

Figure 4.4(a) shows Q_i as a function of photon number for horseshoe Ta resonators. Each color in the plot represents a structurally different film and different markers within the same color indicate structurally similar film but from a different deposition [cf. Chapter 2]. Surprisingly, Ta resonator S1, with both α and β phases present, has the highest Q_i of $(2.0 \pm 0.4) \times 10^6$ in the single photon regime. For α (111) Ta resonators

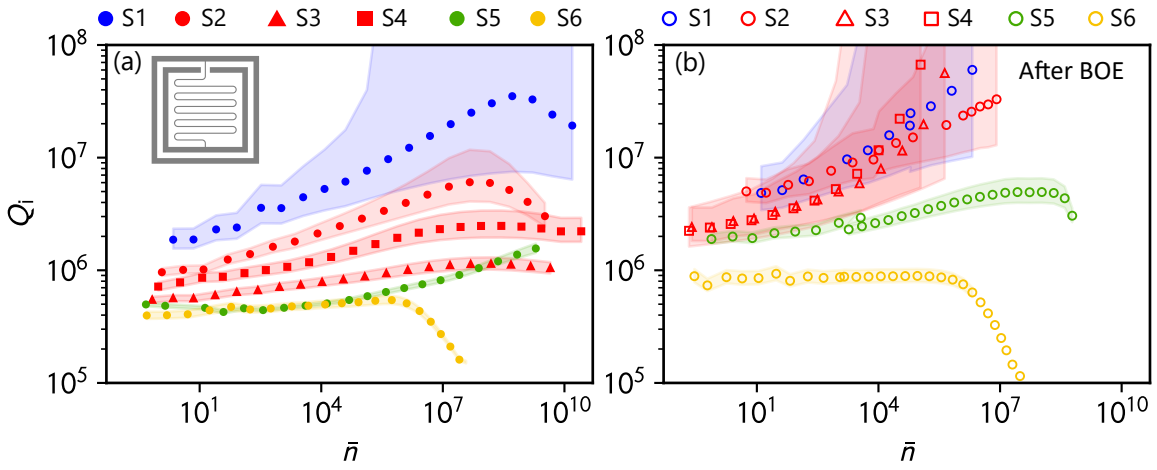

Figure 4.4: Internal quality factor Q_i as a function of the average photon number $\bar{n}$ with Fano uncertainty [185] shown as shaded interval for Ta resonators (a) before (filled markers) and (b) after treating resonators in buffered-oxide etch (BOE, empty markers). The resonator design is shown at the top left corner. The fit uncertainity for Q_i is not shown as it is smaller than the Fano uncertainity. Each color represents a structurally different film and different markers within the same color indicate a structurally similar film but from a different deposition.

S2-S4, Q_i ranges from 5×10^5 to 10^6. Resonators S5 and S6 with $\alpha(110)$ show Q_i of 5×10^5 similar to that of S3 and S4. For all resonators except the commercially deposited S6, Q_i strongly increases with $\bar{n}$, which is associated with the presence of a saturable loss mechanism. For S6, Q_i remains roughly constant upto $\bar{n} \approx 1 \times 10^6$. However, in the regime $\bar{n} \gg 10^7$, we observe a reduction in Q_i with $\bar{n}$ for all of them, possibly associated with quasi-particle heating [23, 59].

Figure 4.4(b) shows the improvement in Q_i, after immersing the chips in BOE for 15 min. We observe 3-6 fold improvement in $Q_{i,LP}$, defined as Q_i at low-power (LP), irrespective of the film micro-structure. Note that S1 and S2 resonators have comparable $Q_{i,LP}$ after BOE treatment. Furthermore, the $Q_{i,LP}$ deteriorates over weeks in air after BOE treatment and the improvement can be reproduced with successive BOE treatments. The reversibility of the change caused by BOE is an interesting information about the loss channel. Possible candidates include etching and re-growth of the surface oxide or loading and unloading of Ta with hydrogen [171]. In the latter case hydrogen could potentially reduce loss from two-level systems [54] by passivating dangling bonds. In addition, residual stress and strain in the film is affected by hydrogen content, which is another potential candidate for the dominating loss mechanism [61].

The shaded region in Fig. 4.4 is uncertainty due to Fano interference [185]. It refers to an asymmetric resonance response caused by the interference between the resonant mode and a continuum of background states. In the context of microwave resonator measurements, this manifests as a distortion or asymmetry instead of Lorentzian shape in the resonator's response i.e. reflection coefficient amplitude. In practice, it is caused by

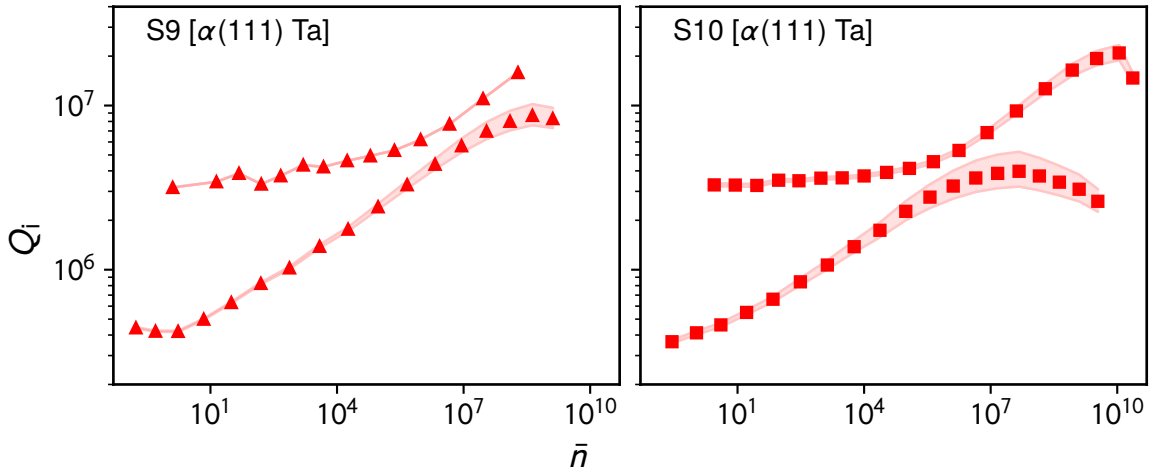

Figure 4.5: Internal quality factor Q_i as a function of the average photon number $\bar{n}$ for sample S9 and S10. Fano uncertainty is shown as shaded intervals and it exceeds fitting uncertainty. In both samples, the higher (lower) Q_i data set corresponds to diluted (interdigitated) resonators.

the the finite isolation of the circulator, an almost unavoidable component in cryogenic single-port reflection measurements.

Figure 4.5 show results for interdigitated and diluted resonators from sample S9 and S10. Both of these samples are fabricated from $\alpha(111)$ Ta films and have varied dielectric-participation. We observe a $Q_{i,LP}$ of approximately 4×10^5 for interdigitated resonators and 3×10^6 for diluted resonators across both samples. The large gap between capacitor plates in diluted resonators reduces dielectric-participation, resulting in a $Q_{i,LP}$ almost an order of magnitude higher than interdigitated resonators.

4.2.1 Quality-factor at high photon number

Typically the resonator reflection coefficient traces a circular path in the complex plane as shown in Fig. 4.3. However, when the applied microwave tone reaches sufficiently high power levels, the resonator begins to exhibit non-linear behavior. This non-linearity manifests as a deviation from the characteristic circular trace and a transformation of the amplitude lineshape from Lorentzian to asymmetric. In addition, the resonant frequency shifts to lower values with increasing drive power - a phenomenon that has been extensively investigated within the kinetic inductance detector community [186].

Mechanisms that contribute to non-linearity in thin-film superconducting resonators include power-dependent current redistribution, quasiparticle generation from readout photon absorption, and the intrinsic non-linear kinetic inductance of the superconducting state [187, 188].

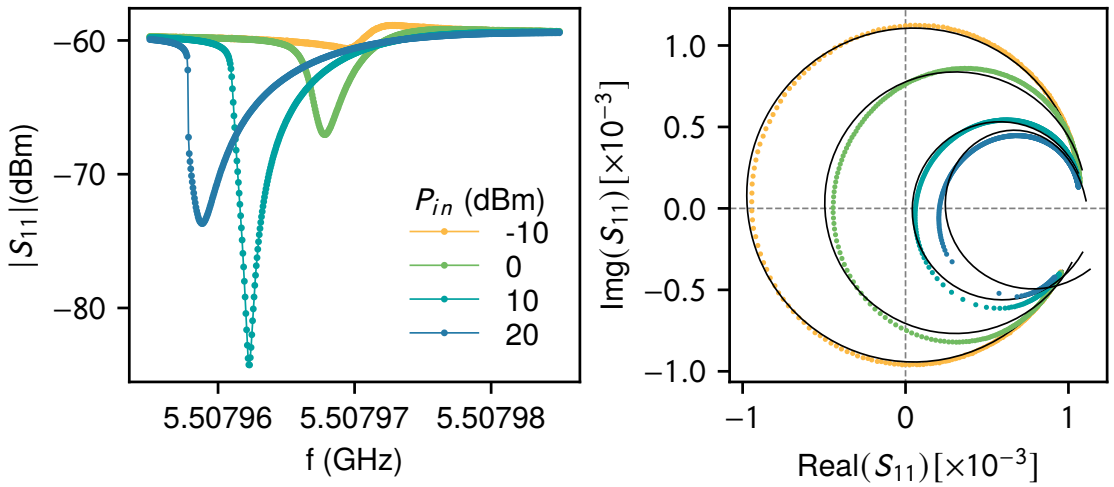

Figure 4.6: Amplitude of measured reflection coefficient as a function of increased frequency (left) and reflection coefficient in complex plane (right). The data was obtained from a horseshoe resonator in high photon regime.

Figure 4.6 shows the non-linear response of a horseshoe resonator at four different powers. Two distinct deviations from the ideal circular trace are observed here: Two different shapes are observed: The first is an elliptical distortion of the otherwise circular response, while the second features sharp discontinuities where the resonator response exhibits abrupt frequency jumps. The elliptical distortion arises from power-dependent loss mechanisms [189], whereas the discontinuous behavior results from the underlying non-linearity of the system.

4.3 Loss mechanisms varying with temperature

Of all the loss mechanisms affecting resonator performance, only two show temperature dependence in the 1 K range, namely TLS and quasiparticle losses [23]. In this section, we present the Mattis-Bardeen model for describing thermal quasi-particle loss in Section 4.3.1. Afterwards, the experimental results are discussed for Q_i and frequency shift dependence on temperature in Sections 4.4.1 and 4.4.2.

4.3.1 Mattis-Bardeen model for thermal quasi-particles

The change in resonance frequency with temperature is caused by the change in superconducting properties of the material. Superconductors are dissipation-free when using direct-current (dc) for $T \ll T_c$. However, this property does not hold for alternating currents (ac), particularly at microwave frequencies of several GHz. The response of a superconductor to an ac field can be understood in the framework of the two-fluid

model, according to which the ac current in a superconductor is carried by a superfluid i.e. Cooper pairs and a normal fluid i.e. unpaired electrons.

$$\sigma(\omega) = \sigma_N(\omega) + \sigma_S(\omega) \tag{4.23}$$

The resulting conductivity is a complex quantity consisting of a resistive part σ_N accounting for dissipation due to quasi-particles and an inductive part σ_S accounting for Cooper pairs. It is well described by the Mattis-Bardeen theory [190]. At temperatures $T > T_c/10$, a fraction of electrons are thermally excited from the Cooper pair state forming quasi-particles giving rise to surface impedance Z_s [191]

$$Z_s = R_s + iX_s = R_s + i\omega L_s = R_s + i\omega\mu_0\lambda_{eff} \tag{4.24}$$

where, R_s is surface resistance, X_s is surface reactance, L_s surface inductance and λ_{eff} is effective penetration depth. The effective conductivity is a complex quantity $\sigma = \sigma_1 - i\sigma_2$, where both real and imaginary parts are given by equations based on section 2.4 of [192]:

$$\frac{\sigma_1}{\sigma_n} = \frac{2}{\hbar\omega}\int_{\Delta}^{\infty}(f(E) - f(E+\hbar\omega))A(E)dE + \frac{1}{\hbar\omega}\int_{\Delta-\hbar\omega}^{-\Delta}(1-2f(E+\hbar\omega))A(E)dE \tag{4.25a}$$

$$\frac{\sigma_2}{\sigma_n} = \frac{1}{\hbar\omega}\int_{\max(\Delta-\hbar\omega,-\Delta)}^{\Delta}(1-2f(E+\hbar\omega))B(E)dE \tag{4.25b}$$

where, σ_n is normal state conductivity, Δ is simplified form of the $f(E)$ is the Fermi-Dirac distribution for quasi-particle distribution in thermal equilibrium and is given by $1/(1+e^{E/k_BT})$ and for convenience, we define two functions

$$A(E) = \frac{E^2 + \Delta^2 + \hbar\omega E}{\sqrt{E^2-\Delta^2}\sqrt{(E+\hbar\omega)^2-\Delta^2}} = -iB(E) \tag{4.26}$$

Note that, we only consider the thermal equilibrium response of complex conductivity and quasiparticles generated due to external pair-breaking (i.e. from an incident flux of photons) are excluded. In the limit k_BT and $\hbar\omega < 2\Delta$, the above equations for conductivity takes a simplified form given by

$$\frac{\sigma_1(\omega,T)}{\sigma_n} = \frac{4\Delta_0}{\hbar\omega}e^{\frac{-\Delta_0}{KT}}\sinh\left(\frac{\hbar\omega}{2k_BT}\right)K_0\left(\frac{\hbar\omega}{2k_BT}\right) \tag{4.27a}$$

$$\frac{\sigma_2(\omega,T)}{\sigma_n} = \frac{\pi\Delta_0}{\hbar\omega}\left[1 - \sqrt{\frac{2\pi k_BT}{\Delta_0}}e^{\frac{-\Delta_0}{KT}} - 2e^{\frac{-\Delta_0}{KT}}e^{\frac{-\hbar\omega}{2k_BT}}I_0\left(\frac{\hbar\omega}{2k_BT}\right)\right] \tag{4.27b}$$

where Δ_0 is the superconducting energy gap, $\Delta_0 = 1.764\ k_BT_c$, and I_n and K_n are the

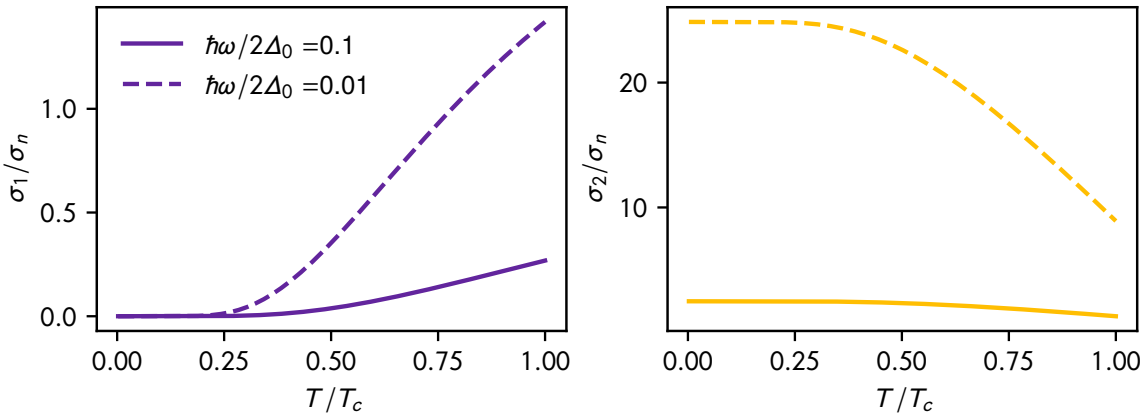

Figure 4.7: σ_1/σ_n and σ_2/σ_n as a function of normalized temperature for two frequency values and for $T_c = 4.4\,\mathrm{K}$, plotting using Eq. (4.27).

n^{th} order modified Bessel function of the first and second kind, respectively. In the limit $T \to 0$, σ_1 and σ_2 takes a simpler form which we will use later to determine quantities at $T = 0$:

$$\frac{\sigma_1(\omega,0)}{\sigma_n} = 0 \quad \text{and} \quad \frac{\sigma_2(\omega,0)}{\sigma_n} = \frac{\pi\Delta_0}{\hbar\omega} \tag{4.28}$$

Surface impedance can be expressed in terms of σ_1 and σ_2, with different forms for the extreme anomalous and local limits. The expression for Z_s and the corresponding conditions for each limit are provided in Table 4.1. The change in Z_s is related to the

limit	expression for Z_s	conditions
Extreme anomalous limit, thick film $t \gg \lambda_{eff}$	$Z_s = i\frac{\sqrt{3}\mu_0\omega}{2}\left[\frac{3\pi\omega}{4\nu_0\lambda_{L0}^2}\left(\frac{\sigma_2}{\sigma_n}+\frac{i\sigma_1}{\sigma_n}\right)\right]^{-1/3}$	$l \gg \lambda_{eff}$ $\xi_0 \gg \lambda_{eff}$
local limit, thick film $t \gg \lambda_{eff}$	$Z_s = \sqrt{\frac{i\omega\mu_0}{\sigma_1 - i\sigma_2}}$	$\xi_0 \ll \lambda_{eff}$ or $l \ll \lambda_{eff}$
local limit, thin film $t \ll \lambda_{eff}$	$Z_s = \frac{1}{(\sigma_1 - i\sigma_2)t}$	$\xi_0 \ll \lambda_{eff}$ or $l \ll \lambda_{eff}$

Table 4.1: Expression for Z_s for extreme anomalous and thin film limits. Here, t is film thickness, λ_{eff} is effective penetration depth, λ_{L0} is penetration depth at $T = 0$, l is mean free path and ξ_0 is coherence length.

change in σ by:

$$\frac{Z_s(\omega,T)-Z_s(\omega,0)}{Z_s(\omega,0)}=\gamma\frac{\sigma(\omega,T)-\sigma(\omega,0)}{\sigma(\omega,0)},\gamma=\begin{cases}-\frac{1}{3} & \text{Extreme anomalous limit, thick film}\\ -\frac{1}{2} & \text{local limit, thick film}\\ -1 & \text{local limit, thin film}\end{cases} \tag{4.29}$$

The temperature dependence of frequency shift and Q_i due to quasi-particle losses is related to the change in X_s and is given by Eq. (2.54) of [192]:

$$\frac{\Delta f}{f_0}=\frac{f(T)-f_0}{f_0}=\frac{-\alpha_\mathrm{k}}{2}\frac{X_s(T)-X_s(0)}{X_s(0)} \tag{4.30a}$$

$$\frac{1}{Q_\mathrm{i}(T)}-\frac{1}{Q_\mathrm{i}(0)}=\alpha_\mathrm{k}\frac{R_s(T)-R_s(0)}{X_s(0)} \tag{4.30b}$$

where α_k is the kinetic inductance fraction, further discussion on which is given in Section 4.4.2.1. From Eq. (4.24), the surface reactance X_s is imaginary part of Z_s. We use local limit, thin film case for our films with $\gamma=-1$ from Eq. (4.29). Taking Eqs. (4.27a), (4.27b) and (4.28) and inserting them in Eq. (4.29), the final expression for frequency shift is given by [5]:

$$\frac{\Delta f}{f_0}=\frac{-\alpha_\mathrm{k}}{2}\left(\left|\frac{\sigma(\omega,0)}{\sigma(\omega,T)}\right|\sin(\phi(\omega,T))-1\right) \tag{4.31}$$

To obtain the expression for Q_i, we need to consider both real and imaginary parts of Z_s which are R_s and X_s, respectively. Note that $R_s(0)$ vanishes for $T=0$.

$$Q_\mathrm{QP}(T)=A_\mathrm{QP}\frac{e^{\frac{\Delta_0}{k_BT}}}{\sinh\left(\frac{\hbar\omega}{2k_BT}\right)K_0\left(\frac{\hbar\omega}{2k_BT}\right)}, \tag{4.32}$$

where A_QP is a constant proportional to α_k.

4.4 Experimental results

In this section, the experimental results from resonator measurements are presented with the aim to examine and compare resonators made from Ta films with three different phase compositions. An overview of the film composition of each sample is given in Table 3.3. The section is structured into two main parts: first, the variation of Q_i

is discussed in Section 4.4.1, followed by the change in relative frequency difference in Section 4.4.2, both as a function of temperature. For each part, the measurement data is derived from the same set of resonators.

4.4.1 Quality-factor dependence on temperature

To gain more insight about the temperature dependence of the resonator losses , we look at Q_i behaviour as a function of temperature at constant drive power at VNA. Figure 4.8 shows Q_i vs temperature for S1-S6. The filled(empty) markers denote measurements before(after) 15 min of BOE treatment. The Q_i behavior can be divided into three regimes. First, starting from the base temperature of 15 m K until $\approx$ 100 m K, Q_i drops slightly as temperature is increased. This effect is attributed to the decrease TLS coherence time and has also been reported in [5] . Second, in the intermediate temperature range, the increase in temperature saturates the TLS losses causing the Q_i to increase. Third, when temperature reaches $T \approx T_c/10$ [193], Q_i starts decreasing due to thermally activated quasi-particle excitations. The data in the third temperature regime is fitted to Eq. (4.32). A_{QP} and T_c are free parameters determined in the fit and only post BOE values are shown in Fig. 4.8. Loss at base temperature is approximated with a constant.

4.4.1.1 Effect of film structure on superconducting properties

For S3 and S4, the extracted values for T_c are approximately consistent with those for bulk Ta of 4.4 K [34]. They are in agreement with the superconducting gap and critical temperature measurements shown in Fig. 2.20. In the case of S1, the T_c is higher than some other only α-Ta containing films S2, S5 and S6. This is surprising as it should be dominated by the low-T_c β-phase. We observe a small reduction from the bulk T_c value showing that the β-phase grains are well proximitized. This is consistent with the atomically coherent interface between $\alpha - \beta$ phase observed in TEM [see Fig. 2.17] and 4-probe DC transport measurements [see Fig. 2.13].

In contrast, the fitted T_c values for S2, S5 and S6 are significantly depressed, as was observed before in Ref. [5]. Elemental analysis using time-of-flight secondary ion mass spectrometry [see Fig. 2.21] did not reveal the presence of magnetic impurities that could explain the lower T_c of S2, S5 and S6. Particularly for film S1, other resonators, S7 and S8, fabricated from the same film do not show the same depressed T_c. A possible explanation is the presence of small β-phase grains, not detectable in XRD.

4.4.1.2 Effect of BOE treatment on superconducting properties

Only for S2, BOE treatment reduces the fitted T_c further as well as the onset of thermal quasi particle loss occurs at much lower temperature as compared to other films consisting of only α-phase.

In case of S5 and S6, the data presented in Fig. 4.8 combines measurements from two resonators on the same chip, taken in both low- and high-temperature regimes. This is common practice for resonators with low Q_i at base temperature. Resonator with highest Q_i and Q_c is measured in the low temperature regime. In case of horseshoe resonators, the highest Q_i resonator has often the highest Q_c of all the resonators on the chip, making it a prime candidate for initial measurements. Once the Q_i drops well below Q_c i.e. it becomes under-coupled ($Q_i < Q_c$), it becomes difficult to measure it with good signal-to-noise ratio. Hence, the second resonator is utilized to measure the thermal quasiparticle losses up to higher temperatures than otherwise would be possible and to maintain continuity in the data across the full range of the temperature sweep.

4.4.1.3 Repeatability and aging of BOE for sample S2

To investigate the deviations in the temperature dependence of Q_i for S2 before and after BOE, we conduct a series of temperature sweep measurements on the same resonator in multiple cool-downs and treating it in different ways beforehand - see Fig. 4.10(a). After a first immersion in BOE, low temperature Q_i improves but at elevated temperature the resonator becomes more susceptible to thermally induced quasi-particle loss. Then, the same sample was kept in vacuum at room temperature within the cryostat for 4 weeks. After cooling it down without exposing it to air, the temperature dependence of Q_i remains nearly the same. After exposing it to ambient conditions for another 4 weeks, low temperature Q_i is found to be almost the same as before the BOE treatment. An improvement of nearly the same amount as after the first BOE treatment, could be achieved by immersing the same sample in BOE for the second time. After this second BOE treatment, the thermal quasi-particle induced loss at elevated temperature does not change. One of our hypothesis for this initial change of quality factor slope was a possible hydrogenation of the film during the BOE treatment. We test this by attempting to remove the hydrogen from the film in an annealing step in ultra-high vacuum ($\approx 1 \times 10^{-7}$ mbar) at 800 °C for 20 min. After this, we measured the sample again (dark yellow graph), resulting in a reduction of Q_i both at low and intermediate temperature. A likely cause for this degradation is the diffusion of oxygen into the film, due to the dissolution of the surface oxide and insufficient vacuum conditions, making the test for hydrogen inconclusive.

To explore whether the depressed T_c from Q_i measurements of S2 remain consistent across various samples from the identical Ta wafer as S2, we conduct measurements

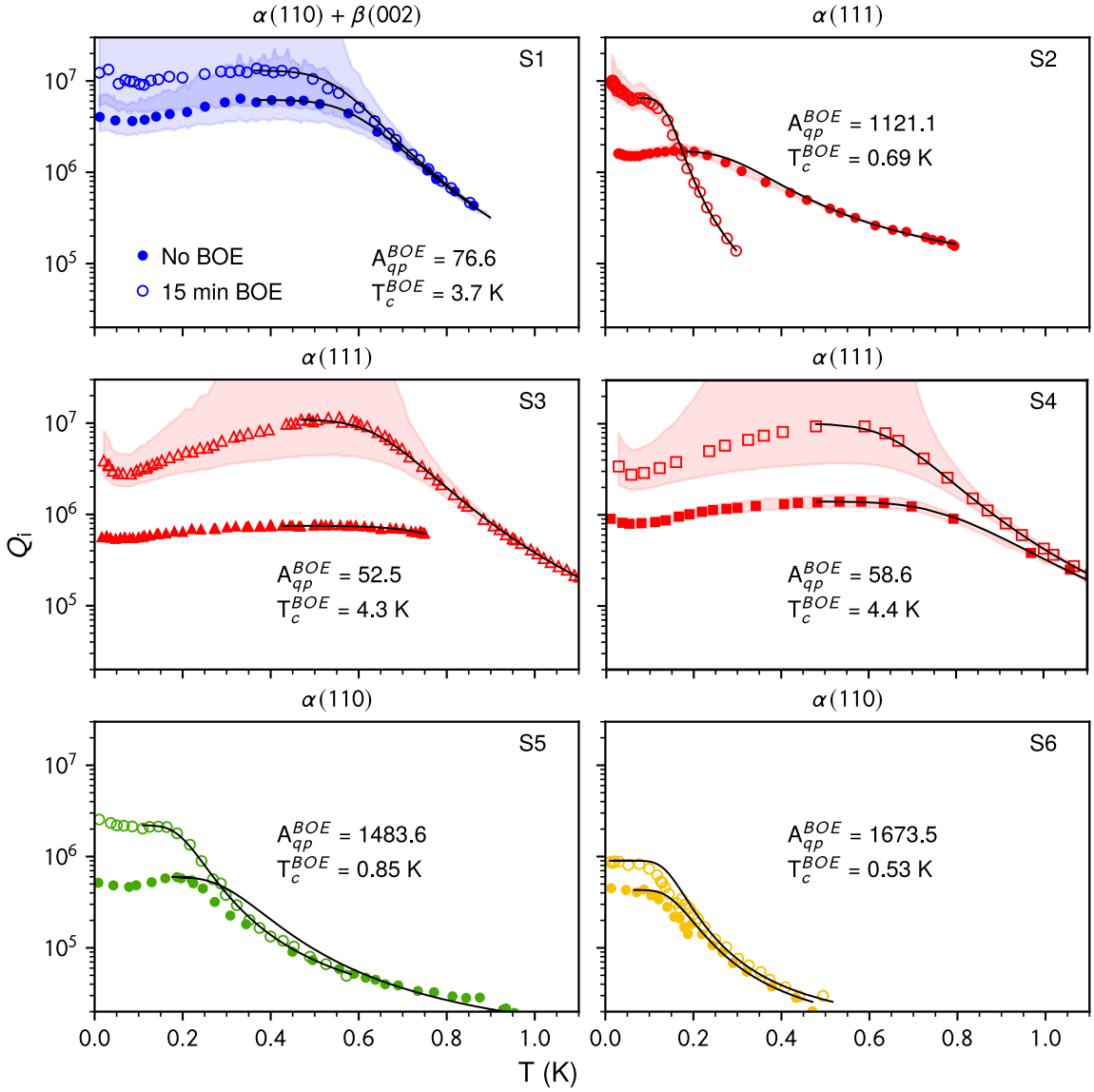

Figure 4.8: Q_i as a function of temperature for horseshoe resonators S1-S6 before(filled markers) and after(empty markers) treating them in BOE for 15 min. The black lines are fits to the simplified model given by Eq. (4.32) for the dataset before and after BOE treatment. Both x- and y-axis ranges are kept same for better comparison. For S2, we note a large change and therefore fit the dataset after BOE separately. The values for T_c and A_{qp} extracted from these fits after BOE are shown in the labels. For S5 and S6, the data shown comprises of two resonators on the same chip measured at two different temperature intervals to cover a larger temperature range. During these measurements, we keep the output power of the vector network analyzer constant, resulting in approximately 10^3 average photons in the resonator at base temperature.

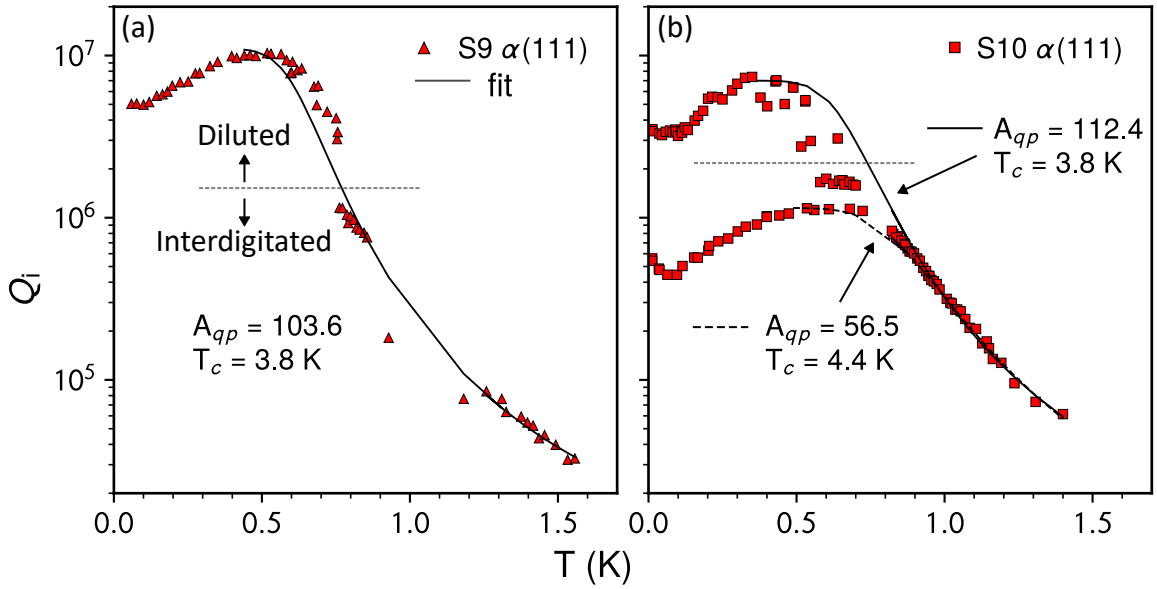

Figure 4.9: Q_i as a function of temperature for (a) sample S9 and (b) S10 (same resonators are shown in Fig. 4.5) without BOE treatment. The black lines are fits to the simplified model given by Eq. (4.32). In both (a) and (b), the data shown comprises of a diluted and two interdigitated resonators on the same chip measured to cover a larger temperature range. The horizontal dashed gray lines serve as visual guides to distinguish between diluted and interdigitated resonator data sets. The photon number for both samples in approximately in the range $1-10^3$.

on additional resonators from two additional samples, S7 and S8. Sample S7 was fabricated using same e-beam lithography process as used for S2. However, when it came to fabricating S8, the optical lithography process had been developed and implemented, leading to S8's fabrication being carried out using this optical lithography [cf. Chapter 3]. Figure 4.10(b) shows Q_i as a function of temperature for additional resonators, S7 and S8. These measurements were performed at fixed input drive power of -50 dBm for S2 and S7 and -20 dBm for S8. This explains the larger Q_i for S8 in the low temperature regime. However, we do not expect a change in the Q_i behavior in the high temperature regime due to input drive power and our comparison of thermally induced quasi-particle loss remains valid. T_c (A_{QP}) for S7 and S8, determined from the fit using Eq. (4.32) are 5.2 K (12.4) and 4.4 K (50.4), respectively. The T_c exceeding bulk value is due to insufficient data in high temperature range. Nonetheless, we can conclude that the source of reduced T_c is present locally in sample S2.

Based on measurements of horseshoe resonators, we can compare the impact of our lithography process on their microwave performance. Only resonators with $\alpha(111)$ phase i.e. S2, S3, S4 and S8 are considered. We observe that the T_c obtained from microwave measurements is closer to the bulk value for resonators fabricated using optical lithography than the ones fabricated using e-beam lithography. However, we notice a slightly reduced Q_i in the single photon regime [cf. Fig. 4.4] for resonators fabricated using optical lithography than e-beam lithography.

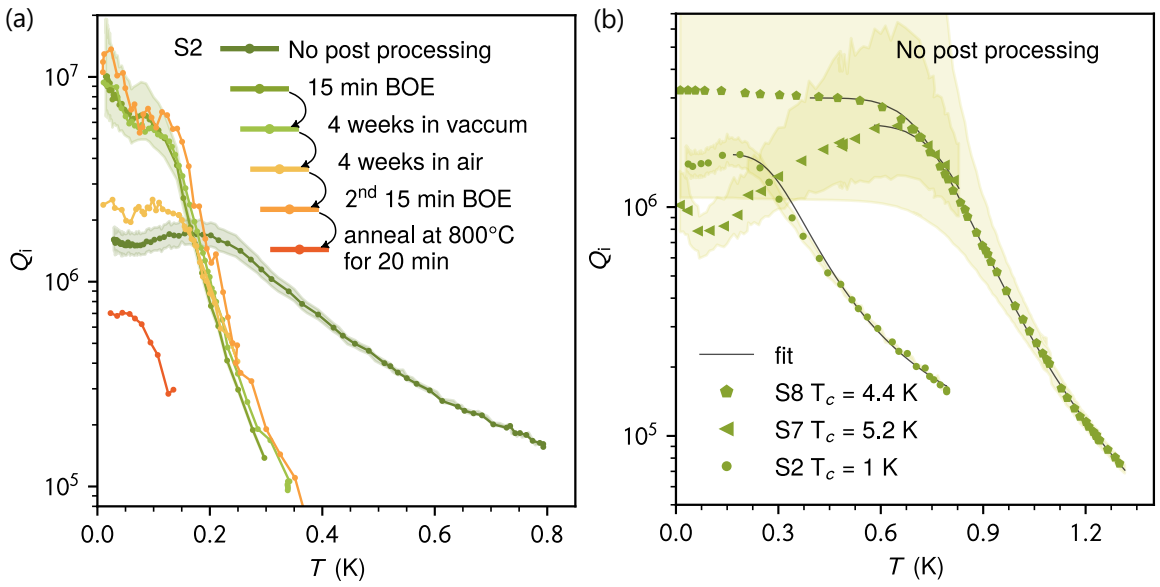

Figure 4.10: Time evolution of Q_i-temperature sweeps for S2 after BOE. (a) Sample S2 before and after treating resonators in BOE repeatedly, different storage conditions between measurements, and after a final annealing step. For details, see main text. (b) three resonators, S2, S7 and S8 which are from different chips but same Ta wafer. S2 and S7 were measured at drive power of −50 dBm whereas S8 was measured at drive power of −20 dBm resulting in a higher Q_i than that of S2 and S7 at low temperatures. Superconducting transition temperature (T_c) is obtained by fitting the decrease in Q_i due to thermally induced quasi-particles in the high temperature regime to Eq. (4.32).

4.4.2 Frequency dependence on temperature

Figure 4.11 shows the relative frequency shift as a function of temperature for horseshoe resonators before and after BOE. Both datasets are fitted using Eq. (4.31) keeping α_k and T_c as free variables. We compare the T_c values obtained from fitting the temperature dependence of frequency shift with the T_c obtained from fitting Q_i and 4-probe dc transport measurements. The latter are generally above 4 K.

4.4.2.1 Kinetic inductance fraction

Kinetic inductance originates from the inertia of charge carriers (electrons or cooper pairs) in presence of an alternating current. Current flowing through the resonator meander wire generates magnetic flux, storing energy in the associated magnetic fields. Additionally, the charge carriers possess kinetic energy, giving rise to kinetic inductance. In normal metals, the effect is usually negligible. But in superconductors, where resistance is nearly zero and current is carried by Cooper pairs, kinetic inductance

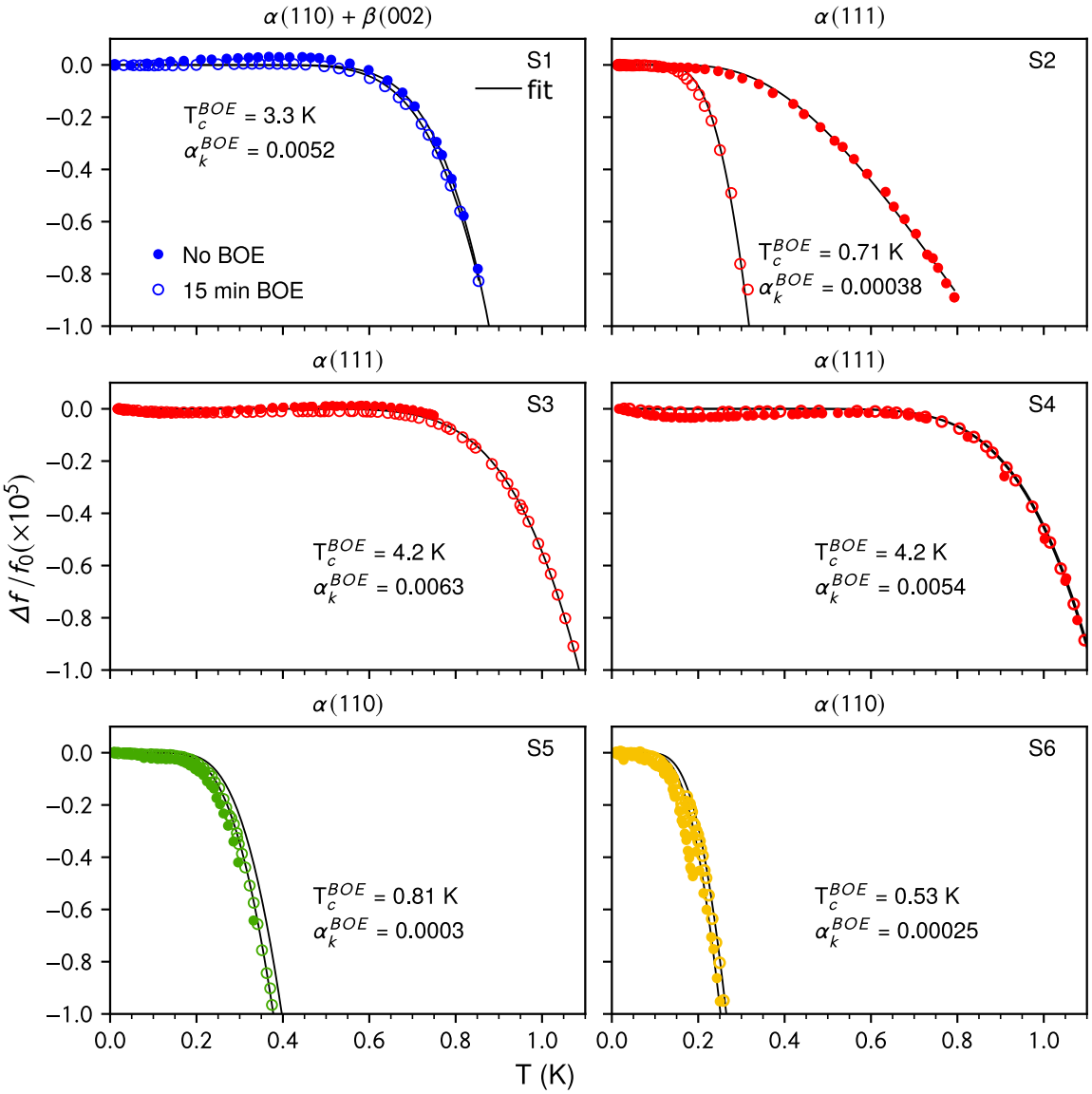

Figure 4.11: Relative frequency shift as a function of temperature for the same horseshoe resonators S1-S6 from Fig. 4.8 before (filled markers) and after(empty markers) treating them in BOE, $\Delta f / f_0 = (f(T) - f_0)/f_0$, where f_0 is the resonant frequency at base temperature (≈ 10 mK). The black line is fit to both before and after BOE data using Eq. (4.31). Both x- and y-axis ranges are kept same for better comparison. For S5 and S6, the shown data comprises of two resonators on the same chip measured at two different temperature intervals to cover the larger temperature range.

can be significant. Thus, the total inductance includes contribution from both kinetic inductance, L_{kin} and magnetic, L_{geo}. The kinetic inductance fraction, α_{k} is defined as

$$\alpha_{\mathrm{k}} = \frac{L_{kin}}{L_{geo} + L_{kin}} \tag{4.33}$$

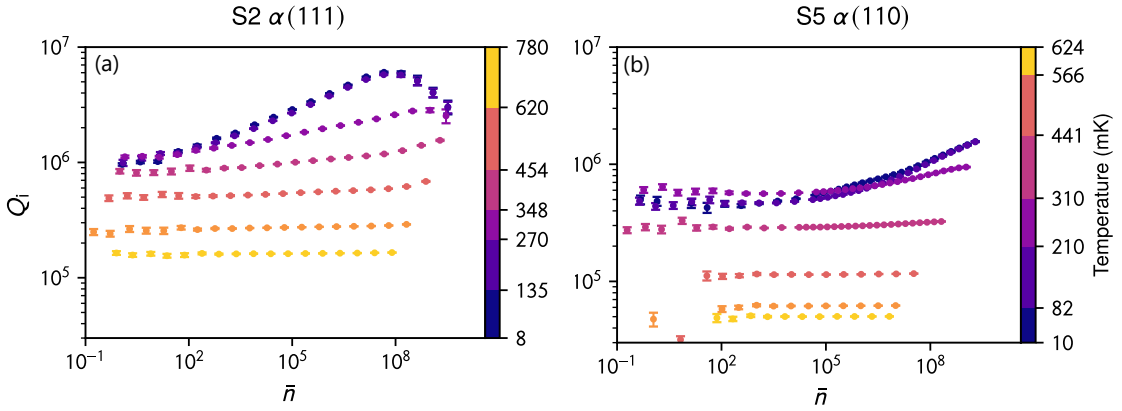

Figure 4.12: Q_i as a function of average photon number $\bar{n}$ for (a) S2 and (b) S5 at different temperature values given in the colorscale.

α_k can also be extracted from the relative frequency shift between the measurement and microwave simulation. The measured frequency f_0 is given by both geometric and kinetic inductance whereas, the simulation for f_0^{sim} does not take kinetic inductance into account.

$$f_0 = \frac{1}{2\pi\sqrt{(L_{geo}+L_{kin})C}} \quad \text{and} \quad f_0^{sim} = \frac{1}{2\pi\sqrt{L_{geo}C}} \tag{4.34}$$

using definition of α_k from Eq. (4.33), the expression for difference in α_k obtained from the frequency offset between measurement and simulation is given by

$$\alpha_k^{\Delta f_0} = \left(1 - \frac{f_0}{f_0^{sim}}\right)^2 \simeq 4\% \tag{4.35}$$

For S2, S5 and S6, α_k is 1-2 orders of magnitude lower compared to those in other samples and more importantly to the $\alpha_k^{\Delta f_0}$ for the same resonators. This large deviation suggests that only a small fraction, of the order of $1-10\%$, of the resonator has a low T_c. To account for this, we propose the existence of a β-phase that remained undetected during film characterization due to its inhomogeneous distribution. Since $Q_{i,LP}$ of S2 was also high among the measured resonators, this hypothesis would align with the benefits of β-Ta in reducing microwave losses. On the other hand, for S3 and S4, the extracted values for α_k from the fit to Eq. (4.31) are comparable to $\alpha_k^{\Delta f_0}$.

Powersweeps at varied temperature For a selection of resonators, powersweep measurements were performed at different temperatures. Results for S2 and S5 are shown in Fig. 4.12(a),(b), respectively. Similar behavior is expected for other resonators. As the temperature starts to increases, the overall Q_i decreases and at a given temperature, the saturable loss also decreases. With further increase in temperature, the Q_i does not show any dependence on $\bar{n}$.

4.4.3 Temperature sweep fit results and discussion of kinetic inductance fraction

The parameters extracted from fitting the temperature dependence of frequency shift and Q_i are listed in the first four columns of Table 4.2. The values for T_c approximately agree when comparing the values extracted from thermal frequency shift and Q_i. The T_c values are slightly lower for sample S1 compared to sample S3 and S4 and the bulk value of about 4.4 K. This is likely due to the well-proximitized inclusions of the β-phase present in the film.

The resistivity of the film for sample S1 was also larger by almost an order of magnitude compared to the films used for samples S2-S4. Also the two parameters are relatively strongly correlated, although it can be stated that T_c determines approximately the temperature where frequency or Q_i deviations due to thermal quasi-particles start to dominate, and the kinetic inductance fraction is related to the slope.

Note that the values for $A_\mathrm{QP}^\mathrm{Q(T)}$ and $\alpha_\mathrm{k}^\mathrm{f(T)}$ in the case of sample S2, S5 and S6 deviate by two orders of magnitude, and one order of magnitude after buffered oxide etch (BOE) treatment. We interpret this as a small part of the resonator (approximately 1 % to 10 % judging from the ratios in α_k) having a depressed T_c that dominates the generation of thermal quasi-particles at elevated temperature.

In addition, the table lists measured (f_0^{meas}) and simulated (f_0^{sim}) frequencies of the resonators. The difference in the latter two frequency can be accounted for by assuming that it is due to the kinetic inductance neglected in the simulation model. Note that the f_0^{meas} are reproducible. The f_0^{meas} of sample S1 is slightly lower than f_0^{sim} due to the larger amount of kinetic inductance added by the high-resistivity β-phase.

For sample S2, difference between measured and simulated frequency does not fit with the α_k extracted from temperature sweep data. This gives further support to the hypothesis that there is a small inhomogeneity with suppressed T_c present in resonator S1. It can dominate the dependence on thermal quasi-particles due to the exponential dependence of their density on temperature, while the low temperature reactance is hardly affected.

Note that the α_k estimated using Eq. (4.35) is systematically larger than $\alpha_\mathrm{k}^\mathrm{f(T)}$. This is most likely because of the simplifications in the HFSS simulation used to determine the geometric inductance of resonator. Possible sources of elevated capacitance are the high dielectric constant of Ta_2O_5 forming on the surface and sidewalls and the finite thickness of the metal sheets. In the simulation, we assumed anisotropic values for the relative permittivity of sapphire measured at 15 K, namely, $\epsilon_{r,\parallel} = 11.34$ parallel to the c-axis and $\epsilon_{r,\perp} = 9.27$ orthogonal to it [168]. We also accounted for differences in fabrication most notably between e-beam and optical lithography, by matching the resonator pattern used in the simulation with optical microscopy images of the resonators.

Sample	$T_c^{Q(T)}$ (K)	$A_{QP}^{Q(T)}$	$T_c^{f(T)}$ (K)	$\alpha_k^{f(T)}$	f_0^{meas} (GHz)	f_0^{sim} (GHz)	$\alpha_k^{\Delta f_0}$
Horseshoe resonators							
S1	3.8	63.2	3.7	0.012	5.4315	5.62	0.066
S1 (BOE)	3.7	76.6	3.3	0.005	5.5079	5.62	0.040
S2	1	6065.6	0.8	0.00028	5.5124	5.62	0.038
S2 (BOE)	0.69	1121.1	0.7	0.00038	5.5091	5.62	0.039
S3	4.6	23	-	-	5.3086	5.43	0.044
S3 (BOE)	4.3	52.5	4.2	0.006	5.3087	5.43	0.044
S4	4.4	50.1	4.2	0.006	5.3146	5.43	0.042
S4 (BOE)	4.4	58.6	4.2	0.005	5.3147	5.43	0.042
S5	1.2	605	0.9	0.0004	5.4924	5.62	0.051
S5 (BOE)	0.86	1462	0.8	0.0003	5.4936	5.62	0.051
S6	0.52	1553	0.5	0.0002	5.4162	5.62	0.13
S6 (BOE)	0.53	1673	0.5	0.0002	5.4165	5.62	0.13
Diluted and interdigitated resonators							
S9	3.8	103.6			4.6570	4.57	
					4.9112	4.7	
					5.2897	5.1	
S10	3.8	112.4			4.7646	4.61	
					5.1906	5	
					5.2892	5.1	

Table 4.2: Summary of parameters resulting from fitting Eqs. (4.31) and (4.32) to the temperature dependence of internal quality factor and frequency shift, as shown in Figs. 4.8 and 4.11, before and after buffered oxide etching, and comparison of the resulting kinetic inductance fraction ($\alpha_k^{f(T)}$) to that derived from frequency offset between measurement and simulation ($\alpha_k^{\Delta f_0}$). Here, "Sample" refers to the resonator samples and "BOE" indicates that the measurement was performed after buffered oxide etch treatment discussed in more detail in the next section. $T_c^{Q(T)}$ and $A_{QP}^{Q(T)}$ correspond to the values for superconducting critical temperature and a constant proportional to the inverse of the kinetic inductance fraction (α_k), respectively, resulting from the fit to the thermal quasi-particle model in Eq. (4.32). The values in columns $T_c^{f(T)}$ and $\alpha_k^{f(T)}$ refer to the fit results for superconducting critical temperature and (α_k), respectively, using the model for the temperature dependent frequency shift in Eq. (4.31). The column f_0^{meas} lists the measured resonator frequencies at low power and base temperature. f_0^{sim} refers to the resonator frequencies determined from simulation of the lumped element resonator in the waveguide using *Ansys HFSS*, approximating the lumped element resonator to have zero thickness and neglecting any surface resistance and reactance. The kinetic inductance fraction estimated from these two frequencies is given by Eq. (4.35).

5 Conclusions and outlook

In this thesis, we investigated the material properties of tantalum thin films to identify material requirements for low dissipation in superconducting quantum circuits. This was motivated by the huge potential of superconducting quantum circuits for making practical quantum processors. Tantalum was the material choice, due to its recent use in state-of-the-art transmon qubits improving their lifetimes to 300 µs to 500 µs [1, 2].

Different types of tantalum films were deposited and then fabricated into microwave resonators, to investigate their quality factors (Q_i). Resonator quality factor measurements are an excellent platform to study material related losses in superconducting quantum circuits, since they constitute a minimal circuit that is easy to fabricate while being limited by similar loss mechanisms as more delicate circuits such as qubits. Film deposition remains an important task as tantalum can exist in two very different crystalline phases namely α- and β-phase. Four types of films were particularly used in this work, most of them deposited in a UHV sputtering system at KIT. In addition, we received some tantalum films from other labs deposited by our collaborators at ENS, Paris and from the commercial supplier StarCryoelectronics. Deposition temperature and rate were the two main parameters adjusted to achieve different crystalline phases and structural properties. Key material properties of tantalum films such as T_c, residual resistance ratio, critical magnetic field, presence of impurities, surface morphology, film structure, etc. were analyzed to correlate them with microwave loss. This work focused on the dielectric and quasiparticle induced losses in microwave regime and in the temperature range 20 mK to 2 K.

As a result of this study, we have identified a few critical improvements to our fabrication recipes that led to lower dissipation. First, we found that a better base-vacuum in the sputtering chamber before film deposition in general leads to higher Q_i resonators. A likely explanation is the reduced levels of oxygen impurities or others in the deposited films. Second, films deposited on large substrates, 2" sapphire wafers in this work, resulted in resonators with higher Q_i than for those where the films were sputtered on smaller substrates. A possible culprit is residual protective resist that was needed for dicing these from a larger substrate. Third, the process involving wet etching to pattern the resonators, invariably resulted in poor Q_i. In general, we also found that sufficiently heating the substrates during deposition leading to high quality epitaxial films, reduced resonator loss.

We observed a tendency of larger Q_i of resonators fabricated with the e-beam lithography process, as opposed to the optical lithography recipe. This could be associated with the 30 keV electron-beam exposure of the film, but other explanations related to differences in the processing are also plausible. Furthermore, more statistics is needed to confirm this correlation.

Furthermore, specific conclusions about losses in tantalum resonator include:

1. The work demonstrated that low-loss superconducting resonators can be fabricated from tantalum films with 10% volume fraction of β-phase defects at the metal-substrate interface. These resonators with a 50 µm capacitor gap achieved internal Q_i upto $(5.0 \pm 2.5) \times 10^6$ in the single-photon regime.
2. Resonators fabricated from high quality pure α-phase Ta films exhibited lower single-photon Q_i in general. For one of these α-phase resonators similarly high internal Q_i was measured.
3. However, the temperature dependence of resonance frequencies and Q_i suggests the presence of low-T_c defects in the film, possibly associated with trace amounts of β-phase not detectable in XRD analysis, or introduced by sample fabrication processes. Our study suggest that the correlation between β-phase concentration and Q_i is more complex than anticipated and a small amount of β-phase in the film can be beneficial, enhancing critical magnetic fields. Its concentration might even be a possible optimization parameter leading to improved coherence in Ta based superconducting circuits.

The conclusions summarized above are encouraging and open up some avenues to improving coherence in Ta based circuits. Yet the question posed initially about the correlation between film properties and dissipation is far from completely answered. There are lot more material aspects that could be explored to bridge the knowledge gap and the results lead to new questions to be tackled in future projects.

For example, strain analyses to compare a structurally good film against one containing grain boundaries. To better understand the role of β-phase, it would be beneficial to develop a deposition process that produces high quality films with both phases. Additionally, depositing films with varying levels of the β-phase could help determine the tolerable limits for its presence in microwave resonators.

Annealed sapphire substrates could be used to improved interface between substrate and metal to achieve high Q_i [37].

Superconducting quantum circuits require temperatures down to mK. It is worth noting that the material properties of Ta, its surface oxide as well as the sapphire substrate can change due to phase transitions or strain release as the circuits are cooled down [63]. Therefore, the field will benefit from advanced low temperature material characterization techniques in the future.

Bibliography

[1] Alexander PM Place *et al.* "New material platform for superconducting transmon qubits with coherence times exceeding 0.3 milliseconds". *Nature communications* **12**(1), 2021 (cited on pages i, 3, 4, 18, 21, 26, 55, 56, 58, 95).

[2] Chenlu Wang *et al.* "Towards practical quantum computers: Transmon qubit with a lifetime approaching 0.5 milliseconds". *npj Quantum Information* **8**(1), 2022 (cited on pages i, 3, 4, 18, 21, 26, 56, 95).

[3] A. Kobler *et al.* "Combination of in situ straining and ACOM TEM: A novel method for analysis of plastic deformation of nanocrystalline metals". *Ultramicroscopy* **128**, 2013 (cited on pages i, 43).

[4] Ritika Dhundhwal *et al.* "High quality superconducting tantalum resonators with beta phase defects". 2025, arXiv:2502.17247 (cited on page i).

[5] Kevin D. Crowley *et al.* "Disentangling Losses in Tantalum Superconducting Circuits". *Phys. Rev. X* **13**, 2023 (cited on pages i, 11, 21, 72, 85, 86).

[6] Newton Schwartz *et al.* "Temperature coefficient of resistance of beta-tantalum films and mixtures with b.c.c.-tantalum". *Thin Solid Films* **14**(2), 1972 (cited on page ii).

[7] Richard P. Feynman. "Simulating physics with computers". *International Journal of Theoretical Physics* **21**(6), 1982 (cited on page 1).

[8] Frank Arute *et al.* "Quantum supremacy using a programmable superconducting processor". *Nature* **574**, 2019 (cited on page 1).

[9] Andrew D. King *et al.* "Beyond-classical computation in quantum simulation". *Science* **388**(6743), 2025 (cited on page 1).

[10] P. Krantz *et al.* "A quantum engineer's guide to superconducting qubits". *Appl. Phys. Rev.* **6**(2), 2019 (cited on page 1).

[11] Colin D. Bruzewicz *et al.* "Trapped-ion quantum computing: Progress and challenges". *Applied Physics Reviews* **6**(2), 2019 (cited on pages 1, 3).

[12] Christophe Couteau *et al.* "Applications of single photons to quantum communication and computing". en. *Nature Reviews Physics* **5**(6), 2023 (cited on page 1).

[13] Anasua Chatterjee *et al.* "Semiconductor qubits in practice". en. *Nature Reviews Physics* **3**(3), 2021 (cited on page 1).

[14] Alexandre Blais *et al.* “Circuit quantum electrodynamics”. *Rev. Mod. Phys.* **93**, 2021 (cited on page 1).

[15] Alex Krasnok *et al.* “Superconducting microwave cavities and qubits for quantum information systems”. *Applied Physics Reviews* **11**(1), 2024 (cited on page 1).

[16] V. V. Sivak *et al.* “Real-time quantum error correction beyond break-even.” *Nature* **616**(7955), 2023 (cited on page 1).

[17] Jose Aumentado. “Superconducting Parametric Amplifiers: The State of the Art in Josephson Parametric Amplifiers”. *IEEE Microwave Magazine* **21**(8), 2020 (cited on pages 1, 73).

[18] Hans Mooij. “Superconducting quantum bits”. *Physics World* **17**(12), 2004 (cited on page 1).

[19] M. H. Devoret *et al.* “Superconducting Qubits: A Short Review”. *arXiv e-prints*, 2004 (cited on pages 2, 7).

[20] John Clarke *et al.* “Superconducting quantum bits”. en. *Nature* **453**(7198), 2008 (cited on page 2).

[21] Lukas Grünhaupt. “Granular aluminium superinductors”. PhD thesis. Karlsruher Institut für Technologie (KIT), 2019. 146 pp. (cited on pages 2, 79).

[22] Irfan Siddiqi. “Engineering high-coherence superconducting qubits”. *Nature Reviews Materials* **6**(10), 2021-10-01 (cited on page 2).

[23] C. R. H. McRae *et al.* “Materials loss measurements using superconducting microwave resonators”. *Review of Scientific Instruments* **91**(9), 2020 (cited on pages 3, 14, 73, 79, 80, 82).

[24] Conal E. Murray. “Material matters in superconducting qubits”. *Materials Science and Engineering: R: Reports* **146**, 2021 (cited on page 3).

[25] Morten Kjaergaard *et al.* “Superconducting Qubits: Current State of Play”. *Annual Review of Condensed Matter Physics* **11**, 2020 (cited on pages 3, 4).

[26] Y. Nakamura *et al.* “Coherent control of macroscopic quantum states in a single-Cooper-pair box”. *Nature* **398**(6730), 1999 (cited on page 3).

[27] Ani Nersisyan *et al.* “Manufacturing low dissipation superconducting quantum processors”. 2019, arXiv:1901.08042 (cited on page 3).

[28] Nathalie P. de Leon *et al.* “Materials challenges and opportunities for quantum computing hardware”. *Science* **372**(6539), 2021 (cited on page 3).

[29] Lert Chayanun *et al.* “Characterization of process-related interfacial dielectric loss in aluminum-on-silicon by resonator microwave measurements, materials analysis, and imaging”. *APL Quantum* **1**(2), 2024 (cited on page 3).

[30] Mikko Tuokkola *et al.* “Methods to achieve near-millisecond energy relaxation and dephasing times for a superconducting transmon qubit”. 2024, arXiv:2407.18778v3 (cited on pages 3, 19, 21).

[31] Alexander Anferov *et al.* “Improved coherence in optically defined niobium trilayer-junction qubits”. en. *Physical Review Applied* **21**(2), 2024 (cited on pages 3, 19).

[32] Josephine B. Chang *et al.* “Improved superconducting qubit coherence using titanium nitride”. *Applied Physics Letters* **103**(1), 2013 (cited on pages 3, 16).

[33] Hao Deng *et al.* “Titanium Nitride Film on Sapphire Substrate with Low Dielectric Loss for Superconducting Qubits”. *Phys. Rev. Appl.* **19**, 2023 (cited on pages 3, 16).

[34] Mildred H. Read *et al.* “A new structure in Tantalum thin films”. *Appl. Phys. Lett.* **7**(3), 1965 (cited on pages 4, 20, 26, 86).

[35] Newton Schwartz *et al.* “Temperature coefficient of resistance of beta-tantalum films and mixtures with b.c.c.-tantalum”. *Thin Solid Films* **14**(2), 1972 (cited on pages 4, 20).

[36] A. A. Navid *et al.* “Nanostructured alpha and beta tantalum formation-Relationship between plasma parameters and microstructure”. *Mater. Sci. Eng., A* **536**, 2012 (cited on pages 4, 20).

[37] Suhas Ganjam *et al.* “Surpassing millisecond coherence in on chip superconducting quantum memories by optimizing materials and circuit design.” *Nat Commun* **15**(1), 2024-05-01 (cited on pages 4, 96).

[38] Russell A. McLellan *et al.* “Chemical Profiles of the Oxides on Tantalum in State of the Art Superconducting Circuits”. *Adv. Sci.* **10**(21), 2023 (cited on pages 4, 21, 69, 72).

[39] Mustafa Bal *et al.* “Systematic improvements in transmon qubit coherence enabled by niobium surface encapsulation”. *npj Quantum Information* **10**(1), 2024 (cited on pages 4, 19, 21, 69).

[40] Olivier Ezratty. “Is there a Moore’s law for quantum computing?” 2023, arXiv:2303.15547 (cited on page 4).

[41] H Kamerlingh Onnes. *Commun. Phys. Lab. Univ. Leiden*, 1911 (cited on page 5).

[42] Dirk van Delft *et al.* “The discovery of superconductivity”. *Physics Today* **63**(9), 2010 (cited on page 5).

[43] W. Meissner *et al. Naturwissenschaften, 21*, 1933 (cited on page 5).

[44] J. Bardeen *et al.* “Theory of Superconductivity”. *Phys. Rev.* **108**, 1957 (cited on pages 6, 48).

[45] S. M. Girvin. “113Circuit QED: superconducting qubits coupled to microwave photons”. *Quantum Machines: Measurement and Control of Engineered Quantum Systems: Lecture Notes of the Les Houches Summer School: Volume 96, July 2011*. Ed. by Michel Devoret *et al.* Oxford University Press, 2014 (cited on page 9).

[46] C. R. H. McRae *et al.* “Materials loss measurements using superconducting microwave resonators”. *Review of Scientific Instruments* **91**(9), 2020 (cited on page 9).

[47] John M Martinis *et al.* “Decoherence in Josephson qubits from dielectric loss”. *Physical review letters* **95**(21), 2005 (cited on pages 10, 79).

[48] Marcel Haas. “Non-linear Dynamics of Two-Level Systems in Non-equilibrium”. PhD thesis. Heidelberg University, 2023 (cited on page 10).

[49] Alexander P. Read *et al.* “Precision Measurement of the Microwave Dielectric Loss of Sapphire in the Quantum Regime with Parts-per-Billion Sensitivity”. *Phys. Rev. Appl.* **19**, 2023 (cited on page 11).

[50] C. Wang *et al.* “Surface participation and dielectric loss in superconducting qubits”. *Applied Physics Letters* **107**(16), 2015 (cited on pages 11, 12).

[51] W. Woods *et al.* “Determining Interface Dielectric Losses in Superconducting Coplanar-Waveguide Resonators”. *Phys. Rev. Appl.* **12**, 2019 (cited on page 11).

[52] J. Verjauw *et al.* “Investigation of Microwave Loss Induced by Oxide Regrowth in High-Q Niobium Resonators”. *Physical Review Applied* **16**(1), 2021 (cited on pages 11, 19).

[53] P. w. Anderson *et al.* “Anomalous low-temperature thermal properties of glasses and spin glasses”. *The Philosophical Magazine: A Journal of Theoretical Experimental and Applied Physics* **25**(1), 1972 (cited on page 13).

[54] Clemens Müller *et al.* “Towards understanding two-level-systems in amorphous solids: insights from quantum circuits”. *Rep. Prog. Phys.* **82**(12), 2019 (cited on pages 13, 79, 80).

[55] Michael R. Vissers *et al.* “Identifying capacitive and inductive loss in lumped element superconducting hybrid titanium nitride/aluminum resonators”. *Applied Physics Letters* **101**(2), 2012 (cited on page 13).

[56] Matthew Reagor *et al.* “Reaching 10ms single photon lifetimes for superconducting aluminum cavities”. *Applied Physics Letters* **102**(19), 2013 (cited on page 13).

[57] D. Zoepfl *et al.* “Characterization of low loss microstrip resonators as a building block for circuit QED in a 3D waveguide”. *AIP Advances* **7**(8), 2017 (cited on pages 13, 64).

[58] Lukas Grünhaupt *et al.* “Loss Mechanisms and Quasiparticle Dynamics in Superconducting Microwave Resonators Made of Thin-Film Granular Aluminum”. *Phys. Rev. Lett.* **121**, 2018 (cited on pages 13, 64, 79).

[59] P. J. de Visser *et al.* “Evidence of a Nonequilibrium Distribution of Quasiparticles in the Microwave Response of a Superconducting Aluminum Resonator”. *Phys. Rev. Lett.* **112**, 2014 (cited on pages 14, 80).

[60] Steven A. H. de Rooij *et al.* “Volume dependence of microwave induced excess quasiparticles in superconducting resonators”. 2025, arXiv:2503.07443 (cited on page 14).

[61] Robin Anthony-Petersen *et al.* “A stress-induced source of phonon bursts and quasiparticle poisoning”. *Nature Communications* **15**(1), 2024 (cited on pages 14, 80).

[62] Shingo Kono *et al.* “Mechanically induced correlated errors on superconducting qubits with relaxation times exceeding 0.4 ms”. en. *Nature Communications* **15**(1), 2024 (cited on page 14).

[63] Y. V. Krasnikova *et al.* “Experimental Observation of Short-Range Magnetic Correlations in Amorphous Nb_2O_5 and Ta_2O_5 Thin Films”. 2025, arXiv:2505.07957 (cited on pages 15, 96).

[64] W. J. Plumbridge. “Tin pest issues in lead-free electronic solders”. en. *Journal of Materials Science: Materials in Electronics* **18**(1), 2007 (cited on page 16).

[65] K. A. Delin *et al.* “The Electrical Engineering Handbook”. Ed. by R. C. Dorf. CRC Press, Boca Raton, FL, 1993. Chap. Superconductivity (cited on page 16).

[66] Charles Kittel *et al. Introduction to solid state physics*. John Wiley & Sons, 2018 (cited on pages 16, 18).

[67] M Müller *et al.* “Magnetic field robust high quality factor NbTiN superconducting microwave resonators”. *Materials for Quantum Technology* **2**(1), 2022 (cited on page 16).

[68] Michael I. Faley *et al.* “Titanium Nitride as a New Prospective Material for NanoSQUIDs and Superconducting Nanobridge Electronics.” *Nanomaterials (Basel, Switzerland)* **11**(2), 2021 (cited on page 16).

[69] Roger W. Cohen *et al.* “Superconductivity in Granular Aluminum Films”. *Phys. Rev.* **168**(2), 1968 (cited on pages 16, 18).

[70] R. W. Shaw *et al.* “Critical Fields of Superconducting Tin, Indium, and Tantalum”. *Phys. Rev.* **120**, 1960 (cited on page 16).

[71] J. J. Hauser *et al.* “Size Effects in Thin Films of V_3Ge, Nb, and Ta”. *Phys. Rev.* **134**(1A), 1964 (cited on pages 16, 48).

[72] Stefano Curiotto *et al.* “Surface morphology and composition of *c*-, *a*- and *m*-sapphire surfaces in O2 and H2 environments”. *Surface Science* **603**(17), 2009 (cited on page 17).

[73] Richard B. Pettit *et al.* “Film structure and enhanced superconductivity in evaporated aluminum films”. *Phys. Rev. B* **13**(7), 1976 (cited on page 17).

[74] A. Megrant *et al.* “Planar superconducting resonators with internal quality factors above one million”. *Applied Physics Letters* **100**(11), 2012 (cited on pages 17, 18).

[75] Ka Ming Law *et al.* “Demonstration of nearly pinhole-free epitaxial aluminum thin films by sputter beam epitaxy”. *Scientific Reports* **10**(1), 2020 (cited on page 17).

[76] C J K Richardson *et al.* “Fabrication artifacts and parallel loss channels in metamorphic epitaxial aluminum superconducting resonators”. *Superconductor Science and Technology* **29**(6), 2016 (cited on pages 17, 18).

[77] Y. Nakamura *et al.* “Coherent control of macroscopic quantum states in a single-Cooper-pair box”. *Nature* **398**(6730), 1999 (cited on page 17).

[78] Sidney Shapiro. “Josephson Currents in Superconducting Tunneling: The Effect of Microwaves and Other Observations”. *Phys. Rev. Lett.* **11**(2), 1963 (cited on page 18).

[79] N. Maleeva *et al.* “Circuit quantum electrodynamics of granular aluminum resonators”. *Nature Communications* **9**(1), 2018 (cited on page 18).

[80] Yachin Ivry *et al.* “Universal scaling of the critical temperature for thin films near the superconducting-to-insulating transition”. *Physical Review B* **90**(21), 2014 (cited on page 18).

[81] E. V. Zikiy *et al.* “High-Q trenched aluminum coplanar resonators with an ultrasonic edge microcutting for superconducting quantum devices.” eng. *Scientific reports* **13**(1), 2023 (cited on page 18).

[82] WM Roach *et al.* “Investigation of epitaxial niobium thin films grown on different surfaces suitable for SRF cavities”. *Proc. 15th Int. Conf. on RF Superconductivity*. 2011 (cited on page 18).

[83] J. Čížek *et al.* “Defects in nanocrystalline Nb films: Effect of sputtering temperature”. *Applied Surface Science* **252**(9), 2006 (cited on page 18).

[84] A. R. Wildes *et al.* “The growth and structure of epitaxial niobium on sapphire”. *Thin Solid Films* **401**(1), 2001 (cited on pages 19, 28, 36).

[85] Maxwell Drimmer *et al. The effect of niobium thin film structure on losses in superconducting circuits*. 2024 (cited on page 19).

[86] Kevin M. Ryan *et al.* “Characterization of Nb films for superconducting qubits using phase boundary measurements”. *Applied Physics Letters* **121**(20), 2022 (cited on page 19).

[87] Akshay A. Murthy *et al.* “Developing a Chemical and Structural Understanding of the Surface Oxide in a Niobium Superconducting Qubit”. *ACS Nano* **16**(10), 2022 (cited on page 19).

[88] M. Virginia P. Altoé *et al.* “Localization and Mitigation of Loss in Niobium Superconducting Circuits”. *PRX Quantum* **3**(2), 2022 (cited on page 19).

[89] M.H. Mueller. “The lattice parameter of tantalum”. *Scripta Metallurgica* **11**(8), 1977 (cited on pages 20, 36, 37, 39, 40).

[90] Alla Arakcheeva *et al.* “The commensurate composite σ-structure of β-tantalum”. *Acta Crystallographica Section B* **59**(3), 2003 (cited on pages 20, 36, 37, 39, 40, 47).

[91] G. Abadias *et al.* “Elastic properties of α- and β-tantalum thin films”. *Thin Solid Films* **688**, 2019 (cited on page 20).

[92] Yoshiro Urade *et al.* “Microwave characterization of tantalum superconducting resonators on silicon substrate with niobium buffer layer”. *APL Materials* **12**(2), 2024 (cited on pages 20–22).

[93] Moritz Singer *et al.* “Tantalum Thin Films Sputtered on Silicon and on Different Seed Layers: Material Characterization and Coplanar Waveguide Resonator Performance”. *2024 IEEE International Conference on Quantum Computing and Engineering (QCE)*. Vol. 01. 2024 (cited on pages 20, 21).

[94] Senthil Kumar Karuppannan *et al. Development of High-Quality α-Ta Film at Room Temperature via Seed Layer Engineering*. 2025 (cited on page 20).

[95] S. Gnanarajan *et al.* “Coexistence of epitaxial Ta(111) and Ta(110) oriented magnetron sputtered thin film on c-cut sapphire”. *Journal of Vacuum Science & Technology A* **28**(2), 2010 (cited on page 21).

[96] Lena N. Majer *et al.* “α-Ta films on c-plane sapphire with enhanced microstructure”. *APL Materials* **12**(9), 2024 (cited on page 21).

[97] Lili Shi *et al.* “Tantalum microwave resonators with ultra-high intrinsic quality factors”. *Applied Physics Letters* **121**(24), 2022 (cited on page 21).

[98] Teun A.J. van Schijndel *et al.* “Cryogenic growth of tantalum thin films for low-loss superconducting circuits”. *Physical Review Applied* **23**(3), 2025 (cited on page 21).

[99] Haolin Jia *et al.* “Investigation of the deposition of α-tantalum (110) films on a-plane sapphire substrate by molecular beam epitaxy for superconducting circuit”. *Journal of Vacuum Science & Technology B* **41**(5), 2023 (cited on page 21).

[100] Boyi Zhou *et al.* “Epitaxial α-Ta (110) film on a-plane sapphire substrate for superconducting qubits on wafer scale”. en. *Japanese Journal of Applied Physics* **62**(10), 2023 (cited on page 21).

[101] S. Gnanarajan *et al.* “Evolution of epitaxial Ta2O5 and Ta2O films during thermal oxidation of epitaxial tantalum films on sapphire substrates”. *Journal of Vacuum Science & Technology A* **26**(3), 2008 (cited on page 21).

[102] D. W. Face *et al.* “Fabrication and dc characteristics of small-area tantalum and niobium superconducting tunnel junctions”. *Journal of Applied Physics* **62**(8), 1987 (cited on page 21).

[103] Jin-Su Oh *et al.* “Structure and Formation Mechanisms in Tantalum and Niobium Oxides in Superconducting Quantum Circuits”. *ACS Nano* **18**(30), 2024 (cited on pages 21, 51, 69).

[104] Hunter J. Frost *et al.* “Oxidation Kinetics of Superconducting Niobium and a-Tantalum in Atmosphere at Short and Intermediate Time Scales” (cited on page 21).

[105] Chenyu Zhou *et al.* “Ultrathin Magnesium-Based Coating as an Efficient Oxygen Barrier for Superconducting Circuit Materials”. en. *Advanced Materials* **36**(18), 2024 (cited on page 21).

[106] Ray D. Chang *et al.* “Eliminating Surface Oxides of Superconducting Circuits with Noble Metal Encapsulation”. *Phys. Rev. Lett.* **134**, 2025 (cited on pages 21, 69).

[107] S. K. H. Lam *et al.* “Fabrication of Ta/Ta-oxide/Ta trilayer Josephson junctions”. *Nuclear Instruments and Methods in Physics Research Section A: Accelerators, Spectrometers, Detectors and Associated Equipment* **559**(2), 2006 (cited on page 21).

[108] Kevin Kouwenhoven *et al.* “Resolving Power of Visible-To-Near-Infrared Hybrid β-Ta/Nb-Ti-N Kinetic Inductance Detectors”. *Physical Review Applied* **19**(3), 2023 (cited on page 22).

[109] H. J. Seim *et al.* “Attempts to Electrodeposit Tantalum”. *Journal of The Electrochemical Society* **96**(1), 1949 (cited on page 26).

[110] Howard C McAllister. *Thin films by thermal evaporation*. University of Wyoming, 1950 (cited on page 26).

[111] R.B. Marcus *et al.* “Formation of f.c.c., b.c.c. and β-tantalum films by evaporation”. *Thin Solid Films* **2**(5), 1968 (cited on page 26).

[112] P. T. Moseley *et al.* “The crystal structure of β-tantalum”. *Acta Crystallographica Section B* **29**(5), 1973 (cited on pages 26, 46).

[113] P. N. Baker. “Preparation and properties of tantalum thin films”. *Thin Solid Films* **14**(1), 1972 (cited on page 26).

[114] Norman E. Booth *et al.* “Superconducting particle detectors”. *Superconductor Science and Technology* **9**(7), 1996 (cited on page 26).

[115] Matthew H. Carpenter *et al.* “Development of Ta-Based Superconducting Tunnel Junction X-Ray Detector Arrays”. *IEEE Transactions on Applied Superconductivity* **23**(3), 2013 (cited on page 26).

[116] D.A. McLean *et al.* “Tantalum-film technology”. *Proceedings of the IEEE* **52**(12), 1964 (cited on page 26).

[117] G.S. Chen *et al.* “Phase formation behavior and diffusion barrier property of reactively sputtered tantalum-based thin films used in semiconductor metallization”. *Thin Solid Films* **353**(1), 1999 (cited on page 26).

[118] Jonathan Black. “Biologic performance of tantalum”. *Clinical Materials* **16**(3), 1994 (cited on page 26).

[119] Dean W. Matson *et al.* “Properties of thick sputtered Ta used for protective gun tube coatings”. *Surface and Coatings Technology* **146-147**, 2001 (cited on page 26).

[120] R. W. Buckman. “New applications for tantalum and tantalum alloys”. *JOM* **52**(3), 2000 (cited on page 26).

[121] R. Barends *et al.* “Minimal resonator loss for circuit quantum electrodynamics”. *Applied Physics Letters* **97**(2), 2010 (cited on page 26).

[122] J. E. Greene. “Review Article: Tracing the recorded history of thin-film sputter deposition: From the 1800s to 2017”. *Journal of Vacuum Science & Technology A* **35**(5), 2017 (cited on page 26).

[123] William Robert Grove. “VII. On the electro-chemical polarity of gases”. *Philosophical Transactions of the Royal Society of London* **142**, 1997 (cited on page 26).

[124] Jon Tomas Gudmundsson *et al.* “1 - Introduction to magnetron sputtering”. *High Power Impulse Magnetron Sputtering*. Ed. by Daniel Lundin *et al.* Elsevier, 2020 (cited on page 26).

[125] Milton Ohring. *Materials Science of Thin Films (Second Edition)*. Ed. by Milton Ohring. Second Edition. San Diego: Academic Press, 2002 (cited on pages 27, 29).

[126] John A Thornton. “The microstructure of sputter-deposited coatings”. *Journal of Vacuum Science & Technology A: Vacuum, Surfaces, and Films* **4**(6), 1986 (cited on page 28).

[127] I. Petrov *et al.* “Microstructural evolution during film growth”. *Journal of Vacuum Science & Technology A* **21**(5), 2003 (cited on page 28).

[128] Philipp Moritz Leufke. “Magnetoelectric coupling in layered LSMO/PZT nanostructures”. en. PhD thesis. Darmstadt: Technische Universität Darmstadt, 2014 (cited on page 30).

[129] Philipp M. Leufke *et al.* “Large-distance rf- and dc-sputtering of epitaxial LaSrMnO thin films”. *Thin Solid Films* **520**(17), 2012 (cited on pages 29, 30).

[130] C. V. R. Vasant Kumar *et al.* “Effect of target-substrate distance on the growth and properties of rf-sputtered indium tin oxide films”. *Journal of Applied Physics* **65**(3), 1989 (cited on page 30).

[131] Li-Jian Meng *et al.* “Influence of the target-substrate distance on the properties of indium tin oxide films prepared by radio frequency reactive magnetron sputtering”. *Journal of Vacuum Science & Technology A* **18**(4), 2000 (cited on page 30).

[132] S. Kyropoulos. “Ein Verfahren zur Herstellung großer Kristalle”. *Zeitschrift für anorganische und allgemeine Chemie* **154**(1), 1926 (cited on page 31).

[133] Andrew Novoselov. “Growth of large sapphire crystals: Lessons learned”. *Journal of Crystal Growth* **578**, 2022 (cited on page 31).

[134] George F. Harrington *et al.* “Back-to-Basics tutorial: X-ray diffraction of thin films”. English. *Journal of Electroceramics* **47**(4), 2021 (cited on pages 35, 36).

[135] T Ungár. “Microstructural parameters from X-ray diffraction peak broadening”. *Viewpoint set no. 35. Metals and alloys with a structural scale from the micrometer to the atomic dimensions* **51**(8), 2004 (cited on page 36).

[136] Daniel J. Graham *et al.* “Back to the basics of time-of-flight secondary ion mass spectrometry of bio-related samples. I. Instrumentation and data collection.” eng. *Biointerphases* **18**(2), 2023 (cited on pages 37, 50).

[137] J. I. Budnick. “Some Studies of the Superconducting Transition in Purified Tantalum”. *Phys. Rev.* **119**, 1960 (cited on page 40).

[138] J. G. C. Milne. “Superconducting Transition Temperature of High-Purity Tantalum Metal”. *Phys. Rev.* **122**, 1961 (cited on page 40).

[139] J. E. Zablocki *et al.* “Search for electron-electron scattering in tantalum”. en. *Journal of Low Temperature Physics* **56**(5), 1984 (cited on page 40).

[140] Van Der Pauw L. J. “A method of measuring the resistivity and Hall coefficient on lamellae of arbitrary shape”. *Philips Technical Review* **20**, 1958 (cited on page 40).

[141] *Realization of a set-up for hall effect measurements, Technische Universität Graz*. 2017 (cited on page 41).

[142] G. Binnig *et al.* “Atomic Force Microscope”. *Phys. Rev. Lett.* **56**, 1986 (cited on page 41).

[143] P.E. West. *Introduction to Atomic Force Microscopy: Theory, Practice, Applications*. Pacific Nanotechnology, 2006 (cited on page 41).

[144] Jonathan J. Colin *et al.* “On the origin of the metastable β-Ta phase stabilization in tantalum sputtered thin films”. *Acta Materialia* **126**, 2017 (cited on page 42).

[145] J.P. Singh *et al.* “Nanoridge domains in α-phase W films”. *Surface Science* **538**(3), 2003 (cited on page 42).

[146] David A. Muller. “Structure and bonding at the atomic scale by scanning transmission electron microscopy”. *Nature Materials* **8**(4), 2009 (cited on page 42).

[147] Colin Ophus. “Quantitative Scanning Transmission Electron Microscopy for Materials Science: Imaging, Diffraction, Spectroscopy, and Tomography”. *Annual Review of Materials Research* **53**, 2023 (cited on page 42).

[148] E.F. Rauch *et al.* “Automated crystal orientation and phase mapping in TEM”. *Materials Characterization* **98**, 2014 (cited on page 43).

[149] Robert A. Schwarzer. “Advances in crystal orientation mapping with the SEM and TEM”. *Ultramicroscopy* **67**(1), 1997 (cited on page 44).

[150] Anubhav Jain *et al.* “Commentary: The Materials Project: A materials genome approach to accelerating materials innovation”. *APL Mater.* **1**(1), 2013 (cited on page 47).

[151] David Sibanda *et al.* “A Mini Review on Thin Film Superconductors”. *Processes* **10**(6), 2022 (cited on page 47).

[152] Tai-Chang Chiang. “Superconductivity in Thin Films”. *Science* **306**(5703), 2004 (cited on page 47).

[153] F.M. Sauerzopf *et al.* “Anisotropy effects in tantalum, niobium, and vanadium down to the millikelvin temperature range”. *Journal of Low Temperature Physics* **66**(3), 1987 (cited on page 47).

[154] Faranak Bahrami *et al.* “Vortex Motion Induced Losses in Tantalum Resonators”. 2025, arXiv:2503.03168 (cited on page 48).

[155] Robert L Fagaly. “Superconducting quantum interference device instruments and applications”. *Review of scientific instruments* **77**(10), 2006 (cited on page 48).

[156] G. Binnig *et al.* “Surface Studies by Scanning Tunneling Microscopy”. en. *Physical Review Letters* **49**(1), 1982 (cited on page 49).

[157] T. Balashov *et al.* “A compact ultrahigh vacuum scanning tunneling microscope with dilution refrigeration”. *Review of Scientific Instruments* **89**(11), 2018 (cited on page 49).

[158] Soroush Arabi *et al.* “Magnetic bound states embedded in tantalum superconducting thin films”. *Applied Physics Letters* **126**(11), 2025 (cited on page 49).

[159] Robert W. Reed *et al.* “Ultrasonic determination of the superconducting energy gap in high-purity tantalum”. *J. Low Temp. Phys.* **24**(1), 1976 (cited on page 49).

[160] Xianlin Luo. “Interface effects in solid electrolytes for Li-ion batteries”. PhD thesis. Karlsruher Institut für Technologie (KIT), 2022 (cited on page 50).

[161] Jernej Ekar *et al.* “Quantitative aspects of ToF-SIMS analysis of metals and alloys in a UHV, O2 and H2 atmosphere”. *Surfaces and Interfaces* **49**, 2024 (cited on page 50).

[162] Sarah Fearn. “Introduction”. *An Introduction to Time-of-Flight Secondary Ion Mass Spectrometry (ToF-SIMS) and its Application to Materials Science*. Morgan & Claypool Publishers, 2015 (cited on page 50).

[163] A. A. Murthy *et al.* “TOF-SIMS analysis of decoherence sources in superconducting qubits”. *Applied Physics Letters* **120**(4), 2022 (cited on page 51).

[164] Anthony P. McFadden *et al.* “Interface-sensitive microwave loss in superconducting tantalum films sputtered on c-plane sapphire”. 2024, arXiv:2412.16730 (cited on page 56).

[165] C. Hedlund *et al.* “Microloading effect in reactive ion etching”. *Journal of Vacuum Science & Technology A* **12**(4), 1994 (cited on page 59).

[166] David M Pozar. *Microwave engineering; 3rd ed.* Hoboken, NJ: Wiley, 2005 (cited on pages 64, 75, 77).

[167] Patrick Winkel *et al.* “Implementation of a Transmon Qubit Using Superconducting Granular Aluminum”. *Phys. Rev. X* **10**, 2020 (cited on page 64).

[168] Jerzy Krupka *et al.* “Complex permittivity of some ultralow loss dielectric crystals at cryogenictemperatures”. *Meas. Sci. Technol.* **10**(5), 1999 (cited on pages 67, 93).

[169] Nicolas Martin *et al.* “Tantalum Oxide Thin Films Sputter-Deposited by Oxygen Gas Pulsing”. *Coatings* **13**(11), 2023 (cited on page 68).

[170] Anjali Premkumar *et al.* “Microscopic relaxation channels in materials for superconducting qubits”. *Communications Materials* **2**(1), 2021 (cited on page 69).

[171] Longchang Ni *et al.* “Compression and decompression of structural tantalum films exposed to buffered hydrofluoric acid”. *Journal of Micromechanics and Microengineering* **30**(5), 2020 (cited on pages 69, 80).

[172] D. P. Lozano *et al.* “Reversing Hydrogen-Related Loss in α-Ta Thin Films for Quantum Device Fabrication”. 2025, arXiv:2503.12889 (cited on page 69).

[173] D P Lozano *et al.* “Low-loss α-tantalum coplanar waveguide resonators on silicon wafers: fabrication, characterization and surface modification”. *Materials for Quantum Technology* **4**(2), 2024 (cited on page 72).

[174] Y. Sunada *et al.* “Fast Readout and Reset of a Superconducting Qubit Coupled to a Resonator with an Intrinsic Purcell Filter”. *Phys. Rev. Appl.* **17**, 2022 (cited on page 73).

[175] M. D. Reed *et al.* “Fast reset and suppressing spontaneous emission of a superconducting qubit”. *Applied Physics Letters* **96**(20), 2010 (cited on page 73).

[176] Y. Sunada *et al.* “Fast Readout and Reset of a Superconducting Qubit Coupled to a Resonator with an Intrinsic Purcell Filter”. *Phys. Rev. Appl.* **17**(4), 2022 (cited on page 73).

[177] D Bothner *et al.* “Inductively coupled superconducting half wavelength resonators as persistent current traps for ultracold atoms”. *New Journal of Physics* **15**(9), 2013 (cited on page 75).

[178] Matthew Reagor *et al.* “Quantum memory with millisecond coherence in circuit QED”. *Phys. Rev. B* **94**, 2016 (cited on page 76).

[179] Lev Krayzman *et al.* “Superconducting quantum memory with a suspended coaxial resonator”. *Applied Physics Letters* **124**(20), 2024 (cited on page 76).

[180] L. Frunzio *et al.* “Fabrication and characterization of superconducting circuit QED devices for quantum computation”. *IEEE Transactions on Applied Superconductivity* **15**(2), 2005 (cited on page 77).

[181] Philip Krantz. “Parametrically pumped superconducting circuits”. PhD thesis. CHALMERS UNIVERSITY OF TECHNOLOGY, 2013 (cited on page 78).

[182] S. Probst *et al.* “Efficient and robust analysis of complex scattering data under noise in microwave resonators”. *Review of Scientific Instruments* **86**(2), 2015 (cited on page 79).

[183] *Qkit framework*. 2017 (cited on page 79).

[184] E. M. Levenson-Falk *et al.* “Single-Quasiparticle Trapping in Aluminum Nanobridge Josephson Junctions”. *Phys. Rev. Lett.* **112**, 2014 (cited on page 79).

[185] D. Rieger *et al.* “Fano Interference in Microwave Resonator Measurements”. *Phys. Rev. Appl.* **20**, 2023 (cited on page 80).

[186] P. J. de Visser *et al.* “Readout-power heating and hysteretic switching between thermal quasiparticle states in kinetic inductance detectors”. *Journal of Applied Physics* **108**(11), 2010 (cited on page 81).

[187] L. J. Swenson *et al.* “Operation of a titanium nitride superconducting microresonator detector in the nonlinear regime”. *Journal of Applied Physics* **113**(10), 2013 (cited on page 81).

[188] M. R. Vissers *et al.* “Low loss superconducting titanium nitride coplanar waveguide resonators”. *Applied Physics Letters* **97**(23), 2010 (cited on page 81).

[189] C N Thomas *et al.* “Nonlinear effects in superconducting thin film microwave resonators”. en. *New Journal of Physics* **22**(7), 2020 (cited on page 82).

[190] D. C. Mattis *et al.* “Theory of the Anomalous Skin Effect in Normal and Superconducting Metals”. *Phys. Rev.* **111**, 1958 (cited on page 83).

[191] J. P. Turneaure *et al.* “The surface impedance of superconductors and normal conductors: The Mattis-Bardeen theory”. *Journal of Superconductivity* **4**(5), 1991 (cited on page 83).

[192] Gao Jiansong. *The Physics of Superconducting Microwave Resonators. Dissertation (Ph.D.), California Institute of Technology*. 2008 (cited on pages 83, 85).

[193] M. Arzeo *et al.* “Microwave losses in MgO, $LaAlO_3$, and $(La_{0.3}Sr_{0.7})(Al_{0.65}Ta_{0.35})O_3$ dielectrics at low power and in the millikelvin temperature range”. *Applied Physics Letters* **104**(21), 2014 (cited on page 86).